

ACTIVE VIBRATION CONTROL OF BEAM AND PLATES BY USING PIEZOELECTRIC
PATCH ACTUATORS

A THESIS SUBMITTED TO
THE GRADUATE SCHOOL OF NATURAL AND APPLIED SCIENCES
OF
MIDDLE EAST TECHNICAL UNIVERSITY

BY

İBRAHİM FURKAN LÜLEÇİ

IN PARTIAL FULLFILLMENT OF THE REQUIREMENTS
FOR
THE DEGREE OF MASTER OF SCIENCE
IN
MECHANICAL ENGINEERING

JANUARY 2013

Approval of the thesis:

**ACTIVE VIBRATION CONTROL OF BEAM AND PLATES BY USING PIEZOELECTRIC
PATCH ACTUATORS**

submitted by **İBRAHİM FURKAN LÜLECI** in partial fulfillment of the requirements for the degree
of **Master of Science in Mechanical Engineering Department, Middle East Technical University**
by,

Prof. Dr. Canan Özgen
Dean, Graduate School of **Natural and Applied Sciences**

Prof. Dr. Suha Oral
Head of Department, **Mechanical Engineering**

Prof. Dr. H. Nevzat Özgüven
Supervisor, **Mechanical Engineering Dept., METU**

Examining Committee Members:

Prof. Dr. Mehmet Çalışkan
Mechanical Engineering Dept., METU

Prof. Dr. H. Nevzat Özgüven
Mechanical Engineering Dept., METU

Prof. Dr. Yavuz Yaman
Aerospace Engineering Dept., METU

Assist. Prof. Dr. Ender Cigeroğlu
Mechanical Engineering Dept., METU

Assist. Prof. Dr. Gökhan O. Özgen
Mechanical Engineering Dept., METU

Date:

28/01/2013

I hereby declare that all information in this document has been obtained and presented in accordance with academic rules and ethical conduct. I also declare that, as required by these rules and conduct, I have fully cited and referenced all material and results that are not original to this work.

Name, Last name: İbrahim Furkan Lüleci

Signature:

ABSTRACT

ACTIVE VIBRATION CONTROL OF BEAM AND PLATES BY USING PIEZOELECTRIC PATCH ACTUATORS

Lüleci, İbrahim Furkan
M. Sc., Department of Mechanical Engineering
Supervisor: Prof. Dr. H. Nevzat Özgüven

January 2013, 117 pages

Conformal airborne antennas have several advantages compared to externally mounted antennas, and they will play an important role in future aircrafts. However, they are subjected to vibration induced deformations which degrade their electromagnetic performances. With the motivation of suppressing such vibrations, use of active vibration control techniques with piezoelectric actuators is investigated in this study.

At first, it is aimed to control the first three bending modes of a cantilever beam. In this scope, four different modal controllers; positive position feedback (PPF), resonant control (RC), integral resonant control (IRC) and positive position feedback with feed-through (PPFFT) are designed based on both reduced order finite element model and the system identification model. PPFFT, is a modified version of PPF which is proposed as a new controller in this study. Results of real-time control experiments show that PPFFT presents superior performance compared to its predecessor, PPF, and other two methods.

In the second part of the study, it is focused on controlling the first three modes of a rectangular plate with four clamped edges. Best location alternatives for three piezoelectric actuators are determined with modal strain energy method. Based on the reduced order finite element model, three PPFFT controllers are designed for three collocated transfer functions. Disturbance rejection performances show the convenience of PPFFT in multi-input multi-output control systems. Performance of the control system is also verified by discrete-time simulations for a random disturbance representing the in-flight aircraft vibration characteristics.

Keywords: Active vibration control, conformal antennas, finite element method, optimal piezoelectric actuator placement, piezoelectric materials.

ÖZ

PIEZOELEKTRİK EYLEYİCİLERLE KİRİŞ VE LEVHALARIN AKTİF TİTREŞİM KONTROLÜ

Lüleci, İbrahim Furkan
Yüksek Lisans, Makina Mühendisliği Bölümü
Tez Yöneticisi: Prof. Dr. H. Nevzat Özgüven

Ocak 2013, 117 sayfa

Hava platformlarında kullanılan konformal antenler dıştan entegre edilen antenlere göre birçok açıdan daha avantajlıdır. Fakat bu antenler titreşim kaynaklı deformasyonlara maruz kaldıklarında elektromanyetik performanslarında kayıp gözlenmektedir. Bu çalışmada, bu titreşimleri sönümleme amacıyla piezoelektrik eyleyicilerin kullanıldığı aktif titreşim kontrol teknikleri incelenmiştir.

Öncelikle bir ankastre kirişin ilk üç eğilme modu kontrol edilmeye çalışılmıştır. Bu kapsamda, hem düşük dereceli sonlu elemanlar modeli hem de tanımlanmış sistem modeli üzerinden dörder farklı modal kontrolcü; pozitif pozisyon geri beslemesi (PPG), rezonans kontrol (RK), integral rezonans kontrol (İRK) ve geçiş besleyicili pozitif pozisyon geri beslemesi (GBPPG), tasarlanmıştır. GBPPG, bu çalışmada önerilen ve PPG'nin geliştirilmesiyle elde edilmiş bir kontrolcüdür. Gerçek zamanlı kontrol uygulamalarında, önerilen metodun diğer kontrol metotlarına göre daha iyi performans gösterdiği gözlenmiştir.

Çalışmanın ikinci bölümünde, dört kenarlı ankastre dikdörtgen bir levhanın ilk üç modunun kontrol edilmesine odaklanılmıştır. En iyi piezoelektrik eyleyici konum alternatifleri modal gerinim enerjisi metoduna göre belirlenmiştir. Düşük dereceli sonlu elemanlar modeli baz alınarak üç eşyerleşik transfer fonksiyonu için üç adet GBPPG kontrolcüsü tasarlanmıştır. Bozucu etki bastırma performansı GBPPG metodunun çok-girdili çok-çıkıtlı kontrol sistemleri için de uygun olduğunu göstermektedir. Kontrol sisteminin performansı, uçuş esnasındaki titreşim karakteristiğini yansıtan bir rastsal bozucu etki için ayırık zamanlı kontrol simülasyonları ile doğrulanmıştır.

Anahtar Kelimeler: Aktif titreşim kontrolü, konformal antenler, sonlu elemanlar yöntemi, optimal piezoelektrik eyleyici yerleşimi, piezoelektrik malzemeler.

To My Mother

ACKNOWLEDGEMENTS

First of all, I want to express my sincere appreciation to Prof. Dr. H. Nevzat ÖZGÜVEN, for his supervision and helpful critics throughout the progress of my thesis study.

I would like to thank my colleagues Deniz MUTLU, Cemal SARALP, Şerife TOL GÜL, Egemen YILDIRIM, Erdal ARGÜN, Emre ERDEM, Mehmet TURHAN, Mustafa Erdem TOPAL and Gökhan YAŞAR in ASELSAN Inc. for their support and friendship.

I would like to express my special thanks to my mother, brother and sister for their endless love, patience and support.

Also thanks to Scientific and Technological Research Council of Turkey (TÜBİTAK) for their financial support.

TABLE OF CONTENTS

| | |
|---|-------------|
| ABSTRACT | V |
| ÖZ..... | VI |
| ACKNOWLEDGEMENTS | VIII |
| TABLE OF CONTENTS | IX |
| LIST OF FIGURES..... | XI |
| LIST OF TABLES..... | XVI |
| LIST OF SYMBOLS | XVII |
| CHAPTERS | |
| 1. INTRODUCTION | 1 |
| 1.1 MOTIVATION OF THE STUDY | 1 |
| 1.2 OBJECTIVE AND SCOPE OF THE STUDY | 6 |
| 2 THEORY..... | 7 |
| 2.1 INTRODUCTION..... | 7 |
| 2.2 PIEZOELECTRIC MATERIAL MODELING IN ANSYS | 7 |
| 2.2.1 <i>Piezoelectric Phenomenon</i> | 8 |
| 2.2.2 <i>Definition of Piezoelectric Material Properties</i> | 8 |
| 2.2.3 <i>Element Types and Finite Element Formulation</i> | 11 |
| 2.3 COLLOCATED MODAL CONTROL..... | 13 |
| 2.3.1 <i>Collocated Control</i> | 13 |
| 2.3.2 <i>Positive Position Feedback (PPF)</i> | 14 |
| 2.3.3 <i>Resonant Control (RC)</i> | 18 |
| 2.3.4 <i>Integral Resonant Control (IRC)</i> | 20 |
| 2.3.5 <i>Positive Position Feedback with Feed-through (PPFFT)</i> | 23 |
| 2.4 PLACEMENT OF PIEZOELECTRIC SENSORS AND ACTUATORS | 27 |
| 2.5 SUMMARY | 33 |
| 3 ACTIVE VIBRATION CONTROL OF A CANTILEVER BEAM..... | 35 |
| 3.1 INTRODUCTION..... | 35 |
| 3.2 PLANT MODELING..... | 36 |
| 3.3 ORDER REDUCTION | 38 |
| 3.4 CONTROLLER DESIGN..... | 44 |
| 3.4.1 <i>Methodology</i> | 44 |
| 3.4.2 <i>Positive Position Feedback (PPF)</i> | 47 |
| 3.4.3 <i>Resonant Controller (RC)</i> | 50 |
| 3.4.4 <i>Integral Resonant Controller (IRC)</i> | 52 |
| 3.4.5 <i>Positive Position Feedback with Feed-through (PPFFT)</i> | 56 |
| 3.5 SYSTEM IDENTIFICATION..... | 61 |
| 3.6 ADAPTATION OF CONTROLLERS | 66 |
| 3.6.1 <i>Positive Position Feedback (PPF)</i> | 66 |
| 3.6.2 <i>Resonant Controller (RC)</i> | 67 |
| 3.6.3 <i>Integral Resonant Controller (IRC)</i> | 68 |
| 3.6.4 <i>Positive Position Feedback with Feed-through (PPFFT)</i> | 70 |
| 3.7 REAL-TIME APPLICATIONS OF DESIGNED CONTROLLERS..... | 71 |
| 3.7.1 <i>Positive Position Feedback (PPF)</i> | 71 |
| 3.7.2 <i>Resonant Controller (RC)</i> | 72 |

| | | |
|----------|--|------------|
| 3.7.3 | <i>Integral Resonant Controller (IRC)</i> | 73 |
| 3.7.4 | <i>Positive Position Feedback with Feed-through (PPFFT)</i> | 74 |
| 3.8 | CONCLUSIONS..... | 75 |
| 4 | ACTIVE VIBRATION CONTROL OF A RECTANGULAR PLATE WITH FOUR CLAMPED EDGES | 79 |
| 4.1 | INTRODUCTION | 79 |
| 4.2 | STRUCTURE TO BE CONTROLLED | 80 |
| 4.3 | ACTUATOR AND SENSOR PLACEMENT | 81 |
| 4.4 | FINITE ELEMENT MODEL | 86 |
| 4.5 | ORDER REDUCTION | 87 |
| 4.6 | CONTROLLER DESIGN..... | 91 |
| 4.7 | CONCLUSIONS..... | 100 |
| 5 | SUMMARY AND CONCLUSIONS | 101 |
| | REFERENCES | 103 |
| | APPENDICES | |
| A | PROPERTIES OF PI DURAACT P-876.A12 | 109 |
| B | Z-POLARIZED MATERIAL PROPERTIES OF PIC255 | 111 |
| C | COMMAND SNIPPETS FOR ORDER REDUCTION | 113 |
| D | SAMPLE SPM FILE IN DENSE FORMAT | 115 |
| E | MATLAB SCRIPT PARSING THE GENERATED SPM FILE | 117 |

LIST OF FIGURES

FIGURES

| | |
|--|----|
| Figure 1-1 Airborne antennas on a: (a) Patrol aircraft [1], (b) Fighter aircraft [2] | 1 |
| Figure 1-2 Typical aircrafts having protruding antennas. (a) AP-3C, (b) F/A-18 [3]..... | 2 |
| Figure 1-3 Typical aircrafts having large antenna housings. (a) Boeing 737-700 AEW&C, (b) Boeing E-3 Sentry | 3 |
| Figure 1-4 Conformal and reflector airborne antennas on the skin of an aircraft [7] | 4 |
| Figure 1-5 Boeing’s Joined Wing SensorCraft concept [8]..... | 4 |
| Figure 1-6 Dynamic deformations of a conformal airborne antenna [9] | 5 |
| Figure 2-1 Piezoelectric effect. (a) Direct, (b) Converse [33] | 8 |
| Figure 2-2 Visual representation of piezoelectric constitutive equations [34]..... | 9 |
| Figure 2-3 Geometries of piezoelectric elements in ANSYS: (a) SOLID5, (b) SOLID226, | 12 |
| Figure 2-4 Pole-zero pattern of a collocated transfer function. (a) Undamped, (b) lightly damped [40] | 13 |
| Figure 2-5 Bode plot of a lightly damped collocated transfer function [40]..... | 14 |
| Figure 2-6 Root locus of $G(s)$ compensated by a PPF filter targeting the first mode..... | 15 |
| Figure 2-7 Bode plot of $G(s)$ compensated by a PPF filter targeting the first mode | 16 |
| Figure 2-8 Root locus of $G(s)$ compensated by a PPF filter targeting the second mode | 16 |
| Figure 2-9 Bode plot of $G(s)$ compensated by a PPF filter targeting the second mode..... | 17 |
| Figure 2-10 Bode plot of PPF filter targeting the first mode | 17 |
| Figure 2-11 Root locus of $G(s)$ compensated by a RC compensator targeting the first mode..... | 18 |
| Figure 2-12 Bode plot of $G(s)$ compensated by a RC compensator targeting the first mode..... | 19 |
| Figure 2-13 Root locus of $G(s)$ compensated by a RC compensator targeting the second mode..... | 19 |
| Figure 2-14 Bode plot of $G(s)$ compensated by a RC compensator targeting the second mode..... | 20 |
| Figure 2-15 Bode plot of RC compensator targeting the second mode | 20 |
| Figure 2-16 Bode plot of different IRC compensators. (a) simple integrator, (b) low-pass (c) band-pass | 21 |
| Figure 2-17 Band-pass integral resonant control scheme | 22 |
| Figure 2-18 Root locus for band-pass IRC compensator | 22 |
| Figure 2-19 Effects of IRC compensator on frequency response | 23 |

| | |
|---|----|
| Figure 2-20 Single mode PPFFT control scheme | 24 |
| Figure 2-21 Effect of feed-through addition on collocated transfer function | 24 |
| Figure 2-22 Root locus of $G(s)$ compensated by a PPFFT controller targeting the first mode..... | 25 |
| Figure 2-23 Bode plot of $G(s)$ compensated by a PPFFT controller targeting the first mode..... | 25 |
| Figure 2-24 Root locus of $G(s)$ compensated by a PPFFT controller targeting the second mode..... | 26 |
| Figure 2-25 Bode plot of $G(s)$ compensated by a PPFFT controller targeting the second mode..... | 26 |
| Figure 2-26 First three mode shapes of the cantilever plate | 31 |
| Figure 2-27 Strain energy distribution of the cantilever plate for the first three modes | 32 |
| Figure 2-28 First five mode shapes of the simply supported plate. | 32 |
| Figure 2-29 Strain energy distribution of the simply supported plate for the first five modes. | 33 |
| Figure 3-1 Proposed simulation procedure for active vibration control with piezoelectric materials..... | 35 |
| Figure 3-2 Dimensions of the structure to be controlled..... | 36 |
| Figure 3-3 Finite element mesh of the model | 37 |
| Figure 3-4 Defined Rayleigh damping spectrum..... | 38 |
| Figure 3-5 Defined input (red) and outputs (blue) of the plant..... | 40 |
| Figure 3-6 Frequency response of reduced and full order $G_{11}(s)$ | 41 |
| Figure 3-7 Frequency response of reduced and full order $G_{21}(s)$ | 41 |
| Figure 3-8 Frequency response of reduced and full order $G_{12}(s)$ | 42 |
| Figure 3-9 Frequency response of reduced and full order $G_{22}(s)$ | 42 |
| Figure 3-10 Step response of reduced and full order (a) $G_{11}(s)$ (b) $G_{21}(s)$ (c) $G_{12}(s)$ (d) $G_{22}(s)$ | 43 |
| Figure 3-11 Control Scheme..... | 44 |
| Figure 3-12 Sample time history of piezoelectric amplifier noise..... | 45 |
| Figure 3-13 Power spectral density of piezoelectric amplifier noise | 45 |
| Figure 3-14 Sample time history of strain gage noise..... | 46 |
| Figure 3-15 Power spectral density of strain gage noise..... | 46 |
| Figure 3-16 View of a sample Simulink model | 47 |
| Figure 3-17 Three mode PPF Control Scheme | 47 |
| Figure 3-18 Effect of 3 mode PPF controller on $G_{12}(s)$ | 48 |
| Figure 3-19 Effect of 3 mode PPF controller on $G_{22}(s)$ | 49 |
| Figure 3-20 Effect of 3 mode PPF controller on transient strain response | 49 |

| | |
|---|----|
| Figure 3-21 Effect of 3 mode PPF controller on transient tip displacement response | 49 |
| Figure 3-22 3 mode Resonant Control Scheme | 50 |
| Figure 3-23 Effect of 3 mode resonant controller on $G_{12}(s)$ | 51 |
| Figure 3-24 Effect of 3 mode RC on transient strain response | 51 |
| Figure 3-25 Effect of 3 mode RC on transient tip displacement response | 51 |
| Figure 3-26 Effect of 3 mode resonant controller on $G_{22}(s)$ | 52 |
| Figure 3-27 Effect of feed-through on collocated frequency response | 53 |
| Figure 3-28 Integral Resonant Control Scheme | 54 |
| Figure 3-29 Effect integral resonant controller on $G_{12}(s)$ | 54 |
| Figure 3-30 Effect integral resonant controller on $G_{22}(s)$ | 55 |
| Figure 3-31 Effect of IRC on transient strain response | 55 |
| Figure 3-32 Effect of IRC on transient tip displacement response | 55 |
| Figure 3-33 3 mode PPFFT Control Scheme | 56 |
| Figure 3-34 Effect of feed-through on collocated frequency response ($G_{11}(s)$) | 57 |
| Figure 3-35 Root-locus and pole-zero map of PPFFT controlled $G_{11}(s)$ | 58 |
| Figure 3-36 Bode diagram of PPFFT controlled $G_{11}(s)$ | 59 |
| Figure 3-37 Effect of PPFFT controller on $G_{12}(s)$ | 59 |
| Figure 3-38 Effect of PPFFT controller on $G_{22}(s)$ | 60 |
| Figure 3-39 Effect of 3 mode PPFFT on transient strain response | 60 |
| Figure 3-40 Effect of 3 mode PPFFT on transient tip displacement response | 60 |
| Figure 3-41 Effect of 3 mode PPFFT on transient tip displacement response-2 | 61 |
| Figure 3-42 Schematic diagram of the experimental setup | 61 |
| Figure 3-43 Picture of the experimental setup | 62 |
| Figure 3-44 Picture of the bonded piezoelectric patches | 62 |
| Figure 3-45 Picture of the bonded strain gages | 62 |
| Figure 3-46 Experimental open-loop transfer function of $G_{11}(s)$ in Bode format | 63 |
| Figure 3-47 Experimental disturbance frequency response ($G_{12}(s)$) | 64 |
| Figure 3-48 Frequency weights used in curve-fitting | 64 |
| Figure 3-49 Experimental and identified $G_{11}(s)$ in Bode format | 65 |
| Figure 3-50 Experimental and identified $G_{12}(s)$ in Bode format | 65 |
| Figure 3-51 Forced response performance of updated 3 mode PPF controller | 67 |
| Figure 3-52 Free response performance of updated 3 mode PPF controller | 67 |
| Figure 3-53 Forced response performance of updated 3 mode RC | 68 |
| Figure 3-54 Free response performance of updated 3 mode RC | 68 |
| Figure 3-55 Forced response performance of updated IRC | 69 |

| | |
|--|----|
| Figure 3-56 Free response performance of updated IRC | 69 |
| Figure 3-57 Forced response performance of updated PPFFT controller | 70 |
| Figure 3-58 Free response performance of updated PPFFT controller | 70 |
| Figure 3-59 Experimental forced response performance of PPF controller..... | 71 |
| Figure 3-60 Experimental free response performance of PPF controller..... | 71 |
| Figure 3-61 Experimental forced response performance of RC | 72 |
| Figure 3-62 Experimental free response performance of RC | 73 |
| Figure 3-63 Experimental forced response performance of IRC | 73 |
| Figure 3-64 Experimental free response performance of IRC | 74 |
| Figure 3-65 Experimental forced response performance of PPFFT controller | 74 |
| Figure 3-66 Experimental free response performance of PPFFT controller | 75 |
| Figure 3-67 Experimental free response performance of PPFFT controller (2)..... | 75 |
| Figure 4-1 First six flexural mode shapes of the structure..... | 80 |
| Figure 4-2 Strain energy distribution for the first mode | 81 |
| Figure 4-3 Strain energy distribution for the second mode..... | 82 |
| Figure 4-4 Strain energy distribution for the third mode | 82 |
| Figure 4-5 Seven location alternatives for piezoelectric patch bonding | 83 |
| Figure 4-6 Normal strain $-X$ on alternative patch locations for the first mode | 84 |
| Figure 4-7 Normal strain $-X$ on alternative patch locations for the second mode..... | 84 |
| Figure 4-8 Normal strain $-X$ on alternative patch locations for the third mode | 85 |
| Figure 4-9 Normal strain $-Y$ on alternative patch locations for the first mode | 85 |
| Figure 4-10 Normal strain $-Y$ on alternative patch locations for the second mode..... | 85 |
| Figure 4-11 Normal strain $-Y$ on alternative patch locations for the third mode | 86 |
| Figure 4-12 Mesh of the finite element model..... | 87 |
| Figure 4-13 Inputs and outputs of the plant | 88 |
| Figure 4-14 Frequency response of reduced and full order $G_{11}(s)$ | 89 |
| Figure 4-15 Frequency response of reduced and full order $G_{12}(s)$ | 89 |
| Figure 4-16 Frequency response of reduced and full order $G_{22}(s)$ | 90 |
| Figure 4-17 Frequency response of reduced and full order $G_{23}(s)$ | 90 |
| Figure 4-18 Frequency response of reduced and full order $G_{33}(s)$ | 90 |
| Figure 4-19 Frequency response of reduced and full order $G_{44}(s)$ | 91 |
| Figure 4-20 Frequency response of reduced and full order $G_{55}(s)$ | 91 |
| Figure 4-21 PPFFT Control Scheme with three actuators | 92 |
| Figure 4-22 Effect of feed-through on collocated frequency response $G_{11}(s)$ | 92 |
| Figure 4-23 Effect of feed-through on collocated frequency response $G_{22}(s)$ | 93 |
| Figure 4-24 Effect of feed-through on collocated frequency response $G_{33}(s)$ | 93 |

| | |
|--|-----|
| Figure 4-25 Root-locus and pole-zero map of PPFFT#1 controlled $G_{11}(s)$ | 94 |
| Figure 4-26 Root-locus and pole-zero map of PPFFT#2 controlled $G_{22}(s)$ | 95 |
| Figure 4-27 Root-locus and pole-zero map of PPFFT#3 controlled $G_{33}(s)$ | 95 |
| Figure 4-28 Effect of PPFFT controller on $G_{44}(s)$ | 96 |
| Figure 4-29 Effect of PPFFT controller on $G_{54}(s)$ | 96 |
| Figure 4-30 Effect of PPFFT controller on $G_{45}(s)$ | 97 |
| Figure 4-31 Effect of PPFFT controller on $G_{55}(s)$ | 97 |
| Figure 4-32 View of the Simulink model | 98 |
| Figure 4-33 Control voltage of piezoelectric patch#1 | 98 |
| Figure 4-34 Control voltage of piezoelectric patch#2 | 98 |
| Figure 4-35 Control voltage of piezoelectric patch#3 | 99 |
| Figure 4-36 Effect of PPFFT controller on acceleration response#1 | 99 |
| Figure 4-37 Effect of PPFFT controller on acceleration response#2..... | 100 |
| Figure A-1 Properties of PI DuraAct P-876.A12..... | 109 |
| Figure A-2 Dimensions of PI DuraAct P-876.A12..... | 109 |
| Figure B-1 Piezoelectric material properties of PIC255..... | 111 |
| Figure D-1 Sample SPM file in Dense Format..... | 115 |

LIST OF TABLES

TABLES

| | |
|---|----|
| Table 2-1 Properties of piezoelectric elements in ANSYS | 11 |
| Table 2-2 Definitions of matrices and vectors in Equation (2.13) | 12 |
| Table 2-3 Optimal locations of surface bonded piezoelectric sensor/actuator patches on a plate [58] | 30 |
| Table 3-1 Material properties of aluminum and PIC 255 | 37 |
| Table 3-2 First six natural frequencies of the structure | 37 |
| Table 3-3 Three mode PPF parameters | 48 |
| Table 3-4 Three mode RC parameters | 50 |
| Table 3-5 Integral Resonant Control parameters | 53 |
| Table 3-6 Three mode PPFFT controller parameters | 57 |
| Table 3-7 Modal properties of identified model vs. finite element model | 66 |
| Table 3-8 Updated 3 mode PPF parameters | 66 |
| Table 3-9 Updated three mode RC parameters | 67 |
| Table 3-10 Updated Integral Resonant Control parameters | 69 |
| Table 3-11 Updated PPFFT parameters | 70 |
| Table 3-12 Experimentally stable 3 mode RC parameters | 72 |
| Table 3-13 Summary of the performance of controllers | 76 |
| Table 4-1 Material properties of aluminum | 80 |
| Table 4-2 First six natural frequencies of the structure | 81 |
| Table 4-3 Directions of strain feedback for seven patch location alternatives | 82 |
| Table 4-4 Comparison of the patch location alternatives | 84 |
| Table 4-5 Material properties of PIC 255 | 86 |
| Table 4-6 First twelve natural frequencies (short-circuited piezoelectric electrodes) | 87 |
| Table 4-7 Numbering of the transfer functions | 88 |
| Table 4-8 Two mode PPFFT#1 controller parameters | 94 |
| Table 4-9 One mode PPFFT#2 controller parameters | 94 |
| Table 4-10 One mode PPFFT#3 controller parameters | 94 |

LIST OF SYMBOLS

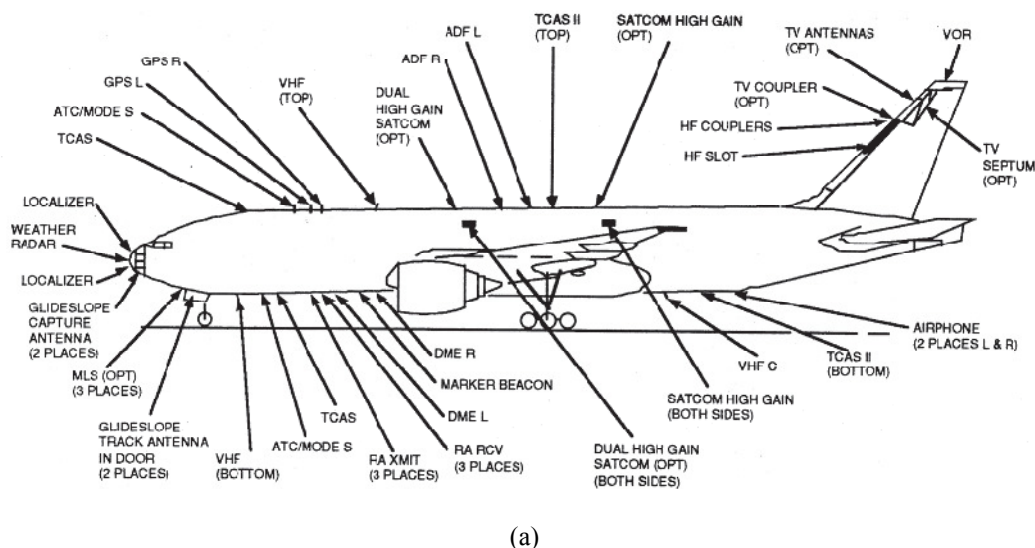
- ω = Circular natural frequency
 ζ = Modal damping ratio
 z = Frequency of zero
 K = Control gain
 $G(s)$ = Transfer function in Laplace domain
 $G(\omega)$ = Transfer function in frequency domain
 K_{FT} = Feed-through gain
 X = State vector
 A = System matrix
 B = Input vector/matrix
 C = Output vector/matrix
 D = Direct feed-through vector/matrix
 V_{act} = Actuation voltage
 J = Cost function
 η = Modal amplitude
 U = Forcing matrix
 Φ = Normalized modal matrix

CHAPTER 1

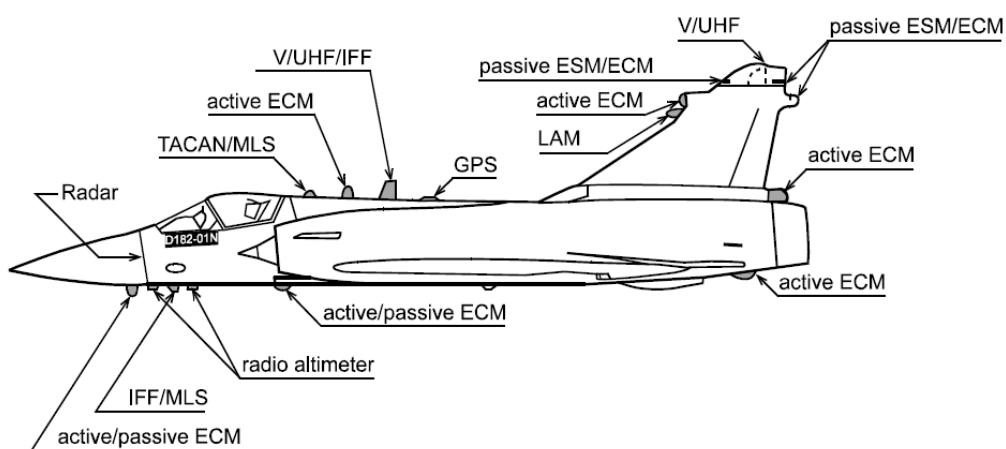
INTRODUCTION

1.1 Motivation of the Study

Military aircrafts have many antennas for different avionic functions such as radar, electronic support measure, electronic counter measure, communication, navigation and identification. Placement of several antennas on a modern patrol and fighter aircrafts are given in Figure 1-1. However, most of these antennas protrude from the skin of the aircraft (Figure 1-2). Even some large antenna housings can change the shape of the air vehicle (Figure 1-3).



(a)



(b)

Figure 1-1 Airborne antennas on a: (a) Patrol aircraft [1], (b) Fighter aircraft [2]

Primary disadvantages of the antennas protruding from the outer mould line (OML) of the aircraft are listed below [3]:

- Reduction in aerodynamic performance due to increased drag coefficient,
- Structural weakening due to cut-outs and locally added extra payloads,
- Increase in observability of aircraft due to increase in radar cross-section,
- Reduction in damage resistance due to vulnerability of protruding, especially blade, antennas.



(a)



(b)

Figure 1-2 Typical aircrafts having protruding antennas. (a) AP-3C, (b) F/A-18 [3]

State of the art airborne antenna studies show that conformal antennas will play an important role in future aircrafts [4–6]. Since conformal airborne antennas are designed to be flush to the OMLs of the aircrafts (Figure 1-4), their contribution on reduction of drag force, radar cross-section and damage susceptibility is unquestionable. Moreover, their being lightweight and having load-bearing capacity (conformal load-bearing antenna structure (CLAS)) make them more advantageous than externally mounted antennas in terms of structural design. With the adoption of this technology, limitations on the antenna size, shape and placement will decrease, which will pave the way for improving electromagnetic performance [3]. To maximize the sensor functionality, several projects exist on special sensor platforms and one of the most popular of those is United States Air Force’s SensorCraft program (Figure 1-5).



(a)



(b)

Figure 1-3 Typical aircrafts having large antenna housings. (a) Boeing 737-700 AEW&C, (b) Boeing E-3 Sentry

Beside advantages, many difficulties are waiting to be studied on which will arise with the employment of conformal airborne antennas. The primary problem is the untraditional multidisciplinary (electromagnetics, analog & digital electronics, aerodynamics, structural mechanics, thermal and material engineering etc.) work required for the design phase. Recalibration of retrofitted system and airworthiness certification are the requirements that should be satisfied for a conformal airborne antenna installation [3].

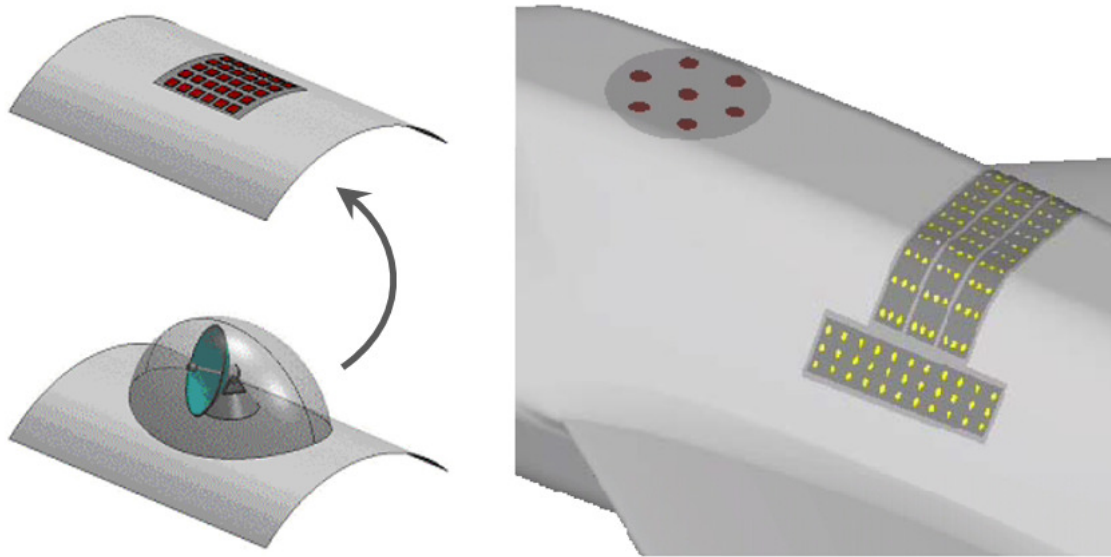


Figure 1-4 Conformal and reflector airborne antennas on the skin of an aircraft [7]

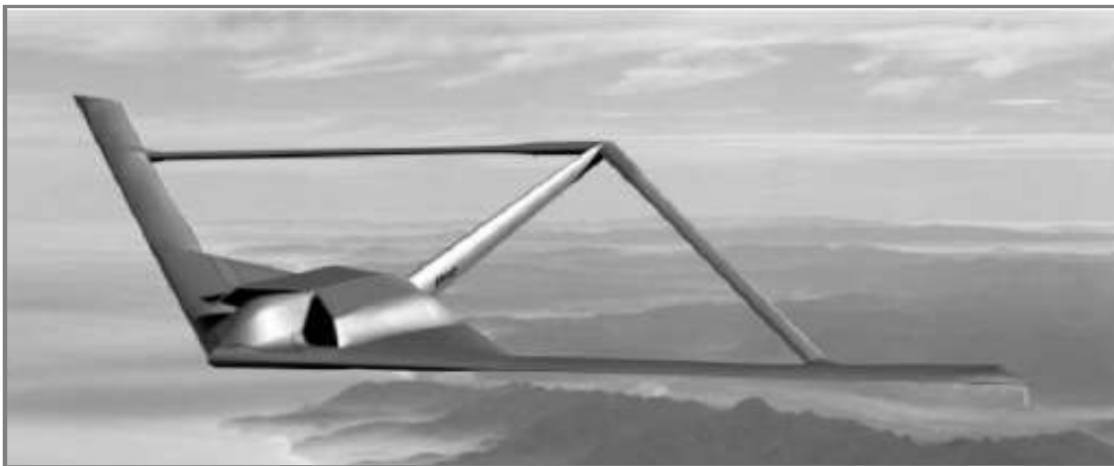


Figure 1-5 Boeing's Joined Wing SensorCraft concept [8]

Performance loss associated with the operational deflections is another popular problem of conformal airborne antennas [9–15]. When the effects of these deflections are taken into account, they can be investigated under two categories:

- Low frequency oscillations: Excitation of the airframe in low frequencies results deformations in global mode shapes. Since a conformal antenna is integrated in a local region, it moves as an almost-rigid-body in the global mode shape of the airframe. As a result, relative position of the each antenna element in the array does not change significantly, but phase center of the array move from its position at rest (Figure 1-6). Possible effects of this motion are error in the looking direction, rise of side lobes, bias on estimated source direction of arrival and resolution loss [9].
- High frequency oscillations: Excitations in high frequencies cause deformations in local mode shapes of the aircraft structure. In this sense, vibratory energy focused at the natural frequencies of the conformal array antenna structure will force the antenna elements to move according to the respective mode shape. During this motion, both mutual positions of the antenna elements change, and phase center of the array shifts from its original position (Figure 1-6). Possible effects of this motion may be broadening or splitting of the clutter

doppler line (which can complicate choice of real targets or create false targets), increase in number of degrees of freedom allocated to cancel a single jammer (possible decrease in the maximum number of jammers that antenna can cancel), bias on real targets and false alarms in the case of passive listening [9].

Fundamentally three different compensation methods are suggested for the solution of aforementioned problem [9,10,12–15]. Principles of these methods are summarized below:

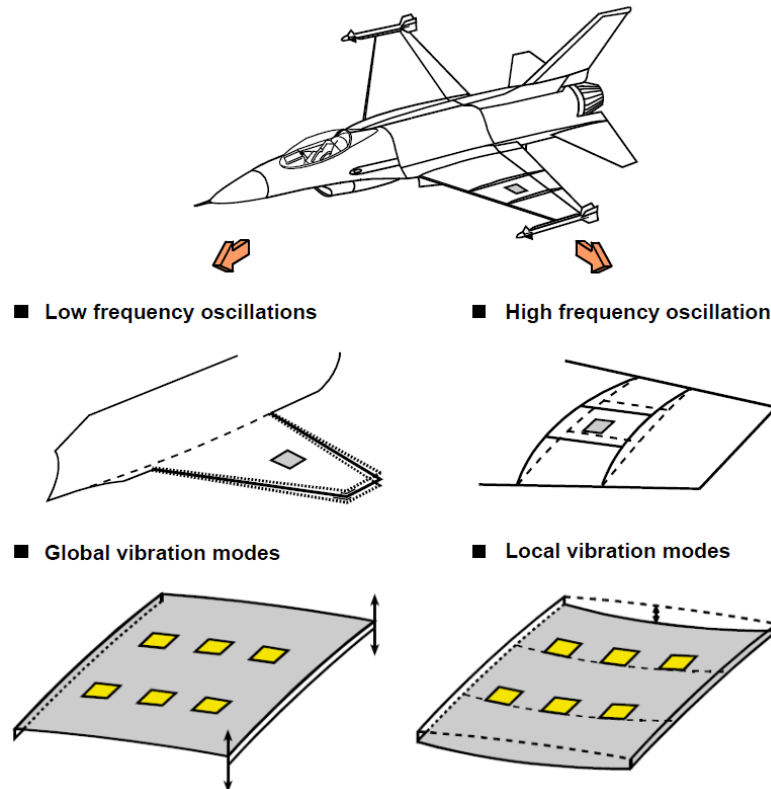


Figure 1-6 Dynamic deformations of a conformal airborne antenna [9]

- **Mechanical compensation:** In this method, it is aimed to minimize the operational deflections. In essence, mechanical sensors and actuators are used to control the vibration of conformal antenna structures in an active manner. Although they could not find place in the literature much, special passive vibration treatment techniques may also be considered.
- **Mechanical sensing and electronic compensation:** Distortion of antenna structure is compensated by phase shifting (at element or sub-array level) in the look direction with respect to the antenna shape information is gathered via mechanical sensors (such as strain gages, piezoelectric patches, accelerometers, inclinometers etc.). Also a mathematical model will be required to relate the sensor outputs with element/sub-array positions. Additionally, excitations of the elements/sub-arrays may have to be revised for large deformations.
- **Signal processing and electronic compensation:** In this method, it is aimed to acquire the shape of the deformed antenna structure by processing external signals like civilian telecommunication signals, strong clutter echoes, data links etc. Amplitude and phase excitations of the elements/sub-arrays will be determined with this information.

Once the power requirement for mechanical compensation of high amplitude global aircraft deformations (e.g. first bending mode of a wing) is considered, it can be concluded that electronic compensation of these deformations is more reasonable. In a supplemental manner, complex local deformations (high frequency and low amplitude) of conformal antenna structures, which would be more troublesome to predict for electronic compensation, can be compensated mechanically.

As mentioned above, active vibration control is one of the most popular mechanical compensation techniques in literature. Fundamental motivation of this study is to extend the know-how on this subject which will be helpful for a future conformal antenna design problem.

1.2 Objective and Scope of the Study

In this study, it is aimed to establish a practical design methodology for active vibration control with piezoelectric materials. In this scope:

- Theoretical information and detailed literature survey on the subjects of piezoelectric material modeling in ANSYS, collocated modal control methods and placement of piezoelectric actuators/sensors are presented in Chapter 2.
- Finite element model of a cantilever beam with piezoelectric patches is generated using ANSYS. A reduced order model of the structure is also obtained with a specialized command of ANSYS. Based on this reduced order model four different collocated modal controllers are designed to control the first three modes of a cantilever beam. Designed controllers are updated after a system identification process. Finally, performances of these controllers are verified by experiments. Details of this study are presented in Chapter 3.
- Active vibration control of a rectangular plate with four clamped edges is studied in Chapter 4. Initially, piezoelectric actuator locations are determined by using modal strain energy method based on the finite element model created in ANSYS. Afterwards, a reduced order multi-input multi-output model of the plant is obtained in ANSYS. By using this model, a novel collocated modal controller is designed to suppress the first three modes of the structure. Finally, performance of the vibration control system is verified by discrete-time simulations for a disturbance representing in-flight aircraft vibration characteristics.
- Finally, a conclusive summary of this study is presented in Chapter 5.

CHAPTER 2

THEORY

2.1 Introduction

In a vibration control study, dynamic characteristics of the structure to be controlled should be well-known in order to design a successful controller. These characteristics can be obtained analytically by using distributed parameters approach, numerically by finite element modeling techniques or experimentally by modal tests and analyses. Analytical methods are extensively used in simple structures but they lose their efficiency when the geometry and/or boundary conditions of the structure are complex. Since experimental techniques require the real structure, they cannot give the required preliminary information to design a vibration control system, like actuator/sensor locations or capabilities. For these reasons, finite element modeling technique is adopted to define the model of the structure to be controlled.

ANSYS is one of the most used finite element software packages in researches on the subject of active vibration control with piezoelectric materials [16–20]. This software is used to perform finite element simulations in this study. Detailed information about piezoelectric modeling techniques in ANSYS are presented in Section 2.2.

Active vibration control is a challenging subject in the area of structural dynamics. Numerous active vibration control methods have been suggested in the literature, including LQR [21–24], LQG [22,23,25], H_∞ [25–27], H_2 [28,29], μ -synthesis [30,31] and adaptive [17,32] controllers. Control studies presented in the scope of this thesis are focused on the use of classical collocated modal control methods. Collocated control phenomenon and different types of collocated modal controllers are investigated in Section 2.3.

Placement of piezoelectric materials on the structure to be controlled is one of the most important problems in piezoelectric-based vibration control application. Detailed literature survey on this problem and solution alternatives are given in Section 2.4.

Finally, discussions and conclusions drawn are summarized in Section 2.5.

2.2 Piezoelectric Material Modeling in ANSYS

A multiphysics analysis is an analysis which couples different fields of physics to solve an engineering problem. ANSYS is a commercial finite element package which provides several types of coupled-field analyses such as thermal-electric, structural-thermal, magneto-structural etc. Piezoelectric analysis is one of them which couples structural and electric fields.

In this section, firstly brief information is given about the piezoelectric phenomenon. Then, the definition of piezoelectric material properties is explained. Finally, piezoelectric element types and coupled piezoelectric finite element formulation in ANSYS are given.

2.2.1 Piezoelectric Phenomenon

Piezoelectricity is an electromechanical phenomenon which relates electricity and mechanical pressure. This phenomenon is discovered by the Curie brothers (Jacques and Pierre Curie) in 1880. They showed that, certain solid materials (named as piezoelectric materials) produce an electric charge when these materials are subjected to mechanical stress. This behavior is called as ‘*direct piezoelectric effect*’. Inversely, an electric field applied to piezoelectric materials causes mechanical deformations, which is called ‘*converse piezoelectric effect*’. Presented bidirectional property enables the use of piezoelectric materials in both actuation and measurement as pictured in Figure 2-1.

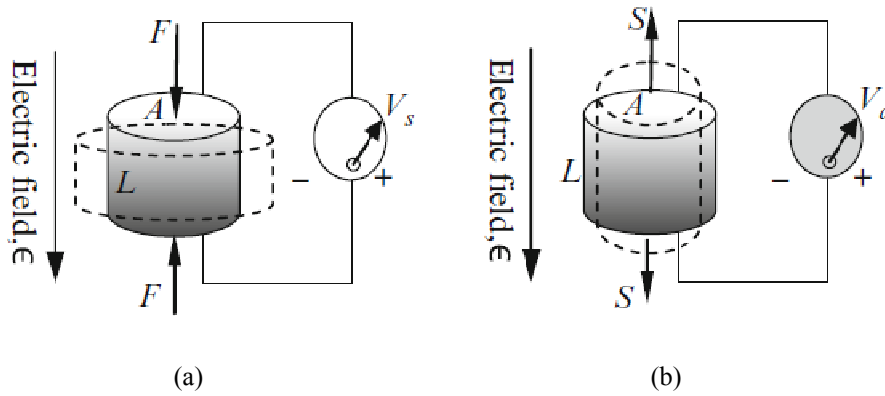


Figure 2-1 Piezoelectric effect. (a) Direct, (b) Converse [33]

Some materials including quartz, ammonium phosphate, paraffin and even bone show piezoelectric behavior naturally. However, synthetic piezoelectric materials are used in engineering applications. Synthetic piezoelectric materials can be categorized as ceramics, crystallines and polymers [34]. The most prominent piezoelectric materials are ceramic based lead zirconate titanate (PZT) and polymer based polyvinylidene fluoride (PVDF). Due to its low modulus of elasticity, PVDF is generally used as sensor. On the contrary, high stiffness and actuation capacity make PZT ideal for actuation. Therefore, PZT actuators are used in this study.

2.2.2 Definition of Piezoelectric Material Properties

In order to model piezoelectric materials in ANSYS, three different matrices are required to be specified. These are permittivity, piezoelectric and elastic coefficient matrices. In this section, derivations of these matrices are presented.

By referencing Hooke’s law, one directional relationship between mechanical strain (S) and stress (T) can be written as follows:

$$S = sT \quad (2.1)$$

where s denotes the elastic compliance (inverse of elastic stiffness) of the material. Another one directional relationship can be given as follows:

$$D = \varepsilon E \quad (2.2)$$

where D , E and ε refer to the electric displacement, electric field and dielectric permittivity of the material, respectively. However, since mechanical and electrical fields are coupled in piezoelectric material, Equations (2.1) and (2.2) are also coupled in the form of:

$$S = s^E T + d.E \quad (2.3)$$

$$D = d.T + \varepsilon^T E \quad (2.4)$$

where superscripts E and T denote constant electric field and constant stress, respectively. The coupling term d is the piezoelectric strain constant. Equations (2.3) and (2.4) are called *linear constitutive equations*. If they are examined carefully, it can be seen that the first equation stands for the converse piezoelectric effect while the second one represents the direct piezoelectric effect. Visual representation of these equations is given in Figure 2-2.

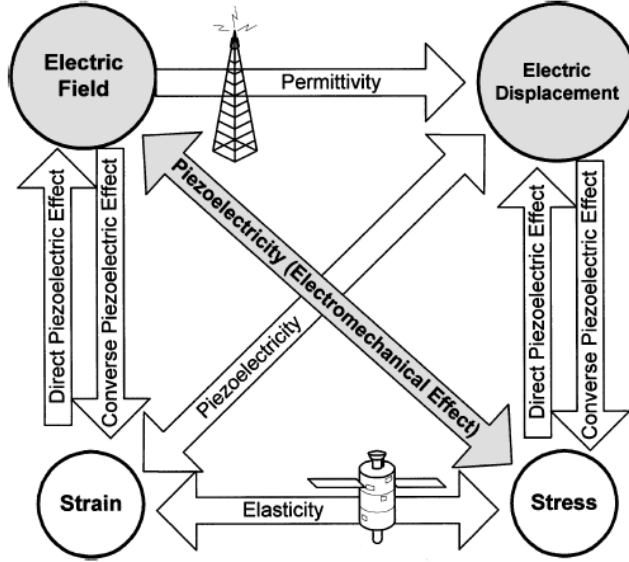


Figure 2-2 Visual representation of piezoelectric constitutive equations [34]

When the directivities of piezoelectric material properties are taken into account, Equations (2.3) and (2.4) can be expanded as:

$$\begin{bmatrix} S_1 \\ S_2 \\ S_3 \\ S_4 \\ S_5 \\ S_6 \end{bmatrix} = \begin{bmatrix} s_{11}^E & s_{12}^E & s_{13}^E & s_{14}^E & s_{15}^E & s_{16}^E \\ s_{21}^E & s_{22}^E & s_{23}^E & s_{24}^E & s_{25}^E & s_{26}^E \\ s_{31}^E & s_{32}^E & s_{33}^E & s_{34}^E & s_{35}^E & s_{36}^E \\ s_{41}^E & s_{42}^E & s_{43}^E & s_{44}^E & s_{45}^E & s_{46}^E \\ s_{51}^E & s_{52}^E & s_{53}^E & s_{54}^E & s_{55}^E & s_{56}^E \\ s_{61}^E & s_{62}^E & s_{63}^E & s_{64}^E & s_{65}^E & s_{66}^E \end{bmatrix} \begin{bmatrix} T_1 \\ T_2 \\ T_3 \\ T_4 \\ T_5 \\ T_6 \end{bmatrix} + \begin{bmatrix} d_{11} & d_{21} & d_{31} \\ d_{12} & d_{22} & d_{32} \\ d_{13} & d_{23} & d_{33} \\ d_{14} & d_{24} & d_{34} \\ d_{15} & d_{25} & d_{35} \\ d_{16} & d_{26} & d_{36} \end{bmatrix} \begin{bmatrix} E_1 \\ E_2 \\ E_3 \end{bmatrix} \quad (2.5)$$

$$\begin{bmatrix} D_1 \\ D_2 \\ D_3 \end{bmatrix} = \begin{bmatrix} d_{11} & d_{12} & d_{13} & d_{14} & d_{15} & d_{16} \\ d_{21} & d_{22} & d_{23} & d_{24} & d_{25} & d_{26} \\ d_{31} & d_{32} & d_{33} & d_{34} & d_{35} & d_{36} \end{bmatrix} \begin{bmatrix} T_1 \\ T_2 \\ T_3 \\ T_4 \\ T_5 \\ T_6 \end{bmatrix} + \begin{bmatrix} \varepsilon_{11}^T & \varepsilon_{12}^T & \varepsilon_{13}^T \\ \varepsilon_{21}^T & \varepsilon_{22}^T & \varepsilon_{23}^T \\ \varepsilon_{31}^T & \varepsilon_{32}^T & \varepsilon_{33}^T \end{bmatrix} \begin{bmatrix} E_1 \\ E_2 \\ E_3 \end{bmatrix} \quad (2.6)$$

By considering the transversely isotropic material properties of the piezoceramics, linear constitutive equations (2.5) and (2.6) can be written, according to the ANSI/IEEE Standard 176-1987, as follows [35]:

When the transversely isotropic material properties of the piezoceramics are considered, required parameters to define a piezoelectric stress matrix ($[e]$) and an elastic stiffness matrix at constant electric field ($[c^E]$) in ANSYS reduce to:

$$[e]_{ANSYS} = \begin{bmatrix} 0 & 0 & e_{13} \\ 0 & 0 & e_{13} \\ 0 & 0 & e_{33} \\ 0 & 0 & 0 \\ 0 & e_{15} & 0 \\ e_{15} & 0 & 0 \end{bmatrix} \quad (2.11)$$

$$[c^E]_{ANSYS} = \begin{bmatrix} c_{11}^E & & & & & \\ c_{12}^E & c_{11}^E & & & & \\ c_{13}^E & c_{13}^E & c_{33}^E & & & \\ 0 & 0 & 0 & c_{66}^E & & \\ 0 & 0 & 0 & 0 & c_{44}^E & \\ 0 & 0 & 0 & 0 & 0 & c_{44}^E \end{bmatrix} \quad (2.12)$$

Hence, permittivity (Equations (2.6) and (2.8)), piezoelectric (Equations (2.9) and (2.11)) and elastic coefficient (Equations (2.10) and (2.12)) matrices, which need to be specified to model piezoelectric material properties in ANSYS, are derived.

2.2.3 Element Types and Finite Element Formulation

In ANSYS 14.0, six different coupled-field elements (*see Table 2-1*) support piezoelectric behavior. In addition, these elements are also used for different coupled fields (structural-thermal, electro-elastic etc.). Hence, in order to choose piezoelectric behavior, relevant key options of these elements should be enabled. Properties of these elements with their piezoelectric key options are given in Table 2-1. Geometries of these elements are shown in Figure 2-3. Further information about the properties of these element types can be found in [37].

Table 2-1 Properties of piezoelectric elements in ANSYS

| Element | Type | Number of nodes | KEYOPT(1) |
|----------|---------------|-----------------|-----------|
| SOLID5 | Brick | 8 | 0 or 3 |
| SOLID226 | Brick | 20 | 1001 |
| SOLID98 | Tetrahedron | 10 | 0 or 3 |
| SOLID227 | Tetrahedron | 10 | 1001 |
| PLANE13 | Quadrilateral | 4 | 7 |
| PLANE223 | Quadrilateral | 8 | 1001 |

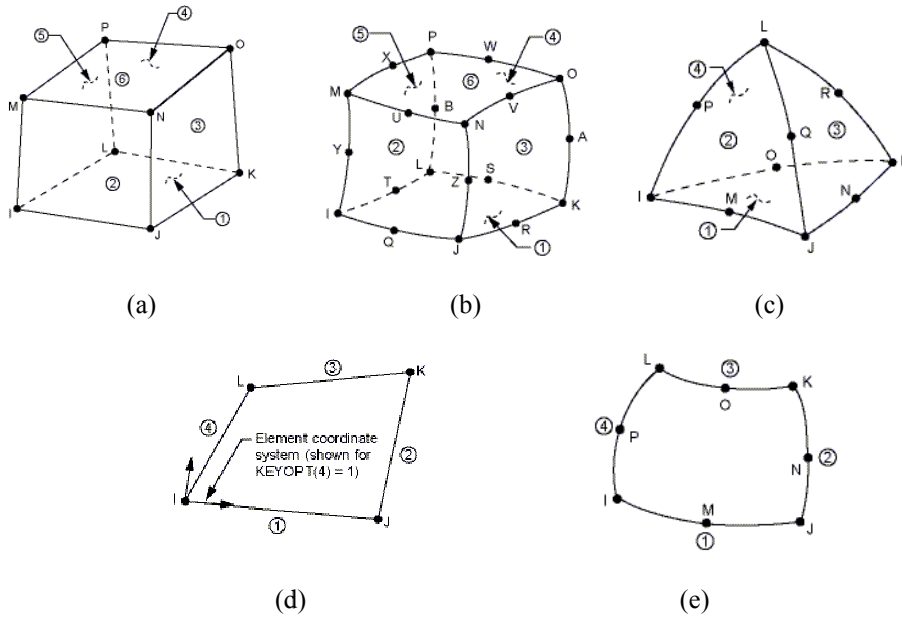


Figure 2-3 Geometries of piezoelectric elements in ANSYS: (a) SOLID5, (b) SOLID226, (c) SOLID98 and SOLID227, (d) PLANE13, (e) PLANE223. [37]

Allik and Hughes [38,39] have derived the coupled finite element matrix equations by using variational principle and finite element discretization. Resulting equilibrium equations are:

$$\begin{bmatrix} [M] & [0] \\ [0] & [0] \end{bmatrix} \begin{Bmatrix} \{\ddot{u}\} \\ \{\ddot{V}\} \end{Bmatrix} + \begin{bmatrix} [C] & [0] \\ [0] & [-C^{vh}] \end{bmatrix} \begin{Bmatrix} \{\dot{u}\} \\ \{\dot{V}\} \end{Bmatrix} + \begin{bmatrix} [K] & [K^z] \\ [K^z]^T & [-K^d] \end{bmatrix} \begin{Bmatrix} \{u\} \\ \{V\} \end{Bmatrix} = \begin{Bmatrix} \{F\} \\ \{L\} + \{L^{th}\} \end{Bmatrix} \quad (2.13)$$

Definitions of piezoelectric matrices and vectors in Equation (2.13) are given in Table 2-2. After nodal displacements and electric potentials are obtained by solving Equation (2.13), unknowns (strain, stress, electric field and electric displacement) at any point in the element can be found by using strain-displacement matrix, electric field-electric potential matrix and linear constitutive equations.

Table 2-2 Definitions of matrices and vectors in Equation (2.13)

| Parameter | Definition |
|--------------|--|
| $\{u\}$ | Vector of nodal displacements |
| $\{V\}$ | Vector of nodal electric potentials |
| $[M]$ | Element mass matrix |
| $[C]$ | Element damping matrix |
| $[C^{vh}]$ | Element dielectric damping matrix |
| $[K]$ | Element stiffness matrix |
| $[K^z]$ | Element piezoelectric coupling matrix |
| $[K^d]$ | Element dielectric permittivity matrix |
| $\{F\}$ | Vector of nodal forces |
| $\{L\}$ | Vector of nodal electric charges |
| $\{L^{th}\}$ | Vector of nodal thermo-piezoelectric loads |

2.3 Collocated Modal Control

In this section, firstly some brief information is given about collocated control. Then, theoretical backgrounds of some collocated modal control methods are given. These methods are positive position feedback (PPF), resonant control (RC) and integral resonant control (IRC). Afterwards, a novel modification on PPF is proposed and properties of this method, positive position feedback with feed-through (PPFFT), are explained in details.

2.3.1 Collocated Control

If the actuator and sensor pairs of a control system are related to the identical degree of freedoms (DOFs), this control system is called a collocated control system. The open loop transfer function of a collocated control system (with a force actuator and displacement sensor) is described as:

$$G(\omega) = \sum_{r=1}^{\infty} \frac{k_r^2}{-\omega^2 + i2\zeta_r\omega_r\omega + \omega_r^2} \quad (2.14)$$

where r , k and ζ denotes mode number, modal constant and modal damping ratio, respectively.

When the frequency response function of a collocated control system is investigated, an interesting property can be observed. A zero exists between each pole of the system which is called as anti-resonance. By considering this interlacing property of poles and zeros, open loop transfer function of a collocated control system can also be described as follows:

$$G(s) = G_0 \frac{\prod_i (s^2 + 2\zeta_i z_i s + z_i^2)}{\prod_j (s^2 + 2\zeta_j \omega_j s + \omega_j^2)} \quad (\omega_k < z_k < \omega_{k+1}) \quad (2.15)$$

If the actuator of a collocated system is excited at anti-resonance frequencies, almost no (absolute zero for an undamped system) response is seen in the sensor. Sample pole-zero pattern and Bode plot of a collocated system are presented in Figure 2-4 and Figure 2-5 [40].

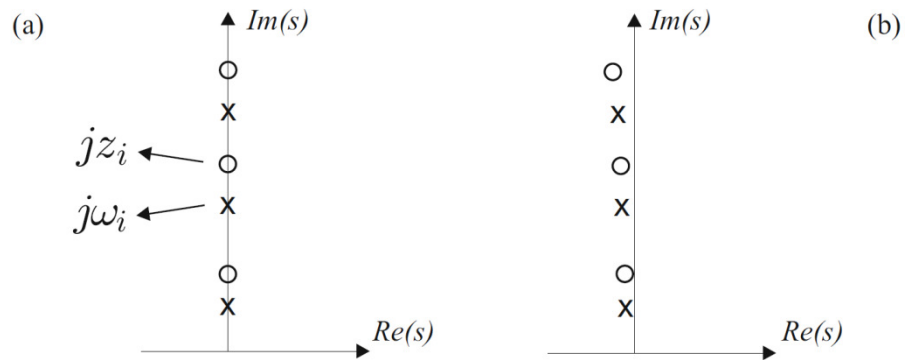


Figure 2-4 Pole-zero pattern of a collocated transfer function. (a) Undamped, (b) lightly damped [40]

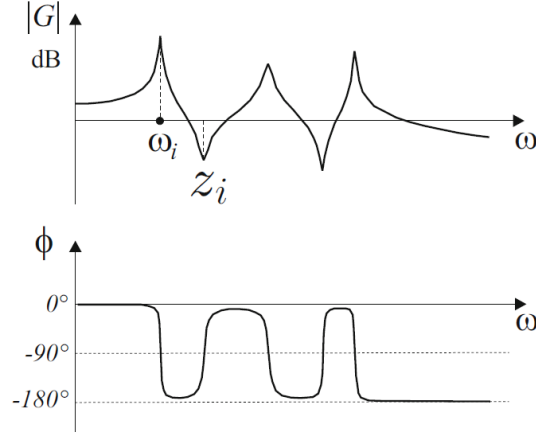


Figure 2-5 Bode plot of a lightly damped collocated transfer function [40]

When the phase response is examined, it can be seen that phase diagram is limited between 0° and -180° . Since phase lag, theoretically, does not exceed 180° , collocated actuator/sensor placement makes the control system advantageous in terms of stability robustness [40,41].

A pole of a non-collocated control system, which is not followed by a zero, results in a net phase lag of 180° . Hence phase response of a non-collocated system is not bounded to the region of $(0^\circ, -180^\circ)$. This property reduces the gain margin and consequently the control bandwidth. For non-collocated control systems, it is recommended to augment damping of the structure in order to obtain larger gain margins [40].

2.3.2 Positive Position Feedback (PPF)

Positive position feedback (PPF) is one of the most popular collocated modal control methods. Method is firstly proposed by Goh and Caughey [42]. Afterwards, numerous researches have been presented in literature investigating mainly the stability and performance robustness [43–46], optimality [23,47], adaptivity [48,49] of the method.

In PPF method, highly damped second order filters, which target the natural frequencies of the structure to be controlled, are used. Transfer function of the second order positive position feedback compensator is given by

$$H(s) = \frac{K}{s^2 + 2\zeta_f \omega_f s + \omega_f^2} \quad (2.16)$$

where parameters K , ζ_f and ω_f refer to gain, damping ratio and frequency of the PPF filter, respectively. Sign of the transfer function indicates the positive feedback.

Equation of motions for a single degree of freedom oscillatory system and a PPF compensator in modal coordinates are given as:

$$\text{Structure :} \quad \ddot{\xi} + 2\zeta\omega\xi + \omega^2\xi = K\eta \quad (2.17)$$

$$\text{Compensator :} \quad \ddot{\eta} + 2\zeta_f\omega_f\dot{\eta} + \omega_f^2\eta = \omega_f^2\xi \quad (2.18)$$

Resulting stability condition [50] for the gain of PPF compensator is as follows:

$$0 < \frac{K}{\omega^2} < 1 \quad (2.19)$$

In order to show the effects of PPF method, a sample collocated transfer function is defined as:

$$G(s) = \frac{1}{s^2 + 2 \cdot (0.01) \cdot (2\pi \cdot 10)s + (2\pi \cdot 10)^2} + \frac{10}{s^2 + 2 \cdot (0.01) \cdot (2\pi \cdot 50)s + (2\pi \cdot 50)^2} + 10^{-4} \quad (2.20)$$

This transfer function is composed of two modes with natural frequencies of 10 and 50 Hz. In order to represent damping, a modal damping ratio with a magnitude 1% is used for each mode. A positive feed-through term is used to include stiffness effect of the truncated modes on the first two modes.

Effect of a PPF filter targeting the first mode is shown on both root-locus and Bode diagrams in Figure 2-6 and Figure 2-7. Parameters of this PPF filter are $K = 10^6$, $\zeta_f = 0.20$ and $\omega_f = 2\pi \cdot 10$. Effect of another PPF filter (with parameters $K = 5 \cdot 10^7$, $\zeta_f = 0.20$ and $\omega_f = 2\pi \cdot 50$) targeting the second mode is presented in Figure 2-8 and Figure 2-9.

When the effects of PPF filters are examined, following conclusions can be drawn:

- Filter tuned for the first mode does not affect the response around the second mode. This is a result of low-pass characteristic (see Figure 2-10) of PPF filters which prevents control spillover on high frequency modes.
- Filter tuned for the second mode locates the first pole to a lower frequency. Hence, in order to control multiple modes, PPF filters targeting higher frequency modes should be tuned before the ones targeting lower frequency modes.
- Both filters amplify the response in quasi-static region. This behavior is a drawback of positive feedback, and one should be careful while designing a multi-mode PPF controller in order not to saturate the actuators.

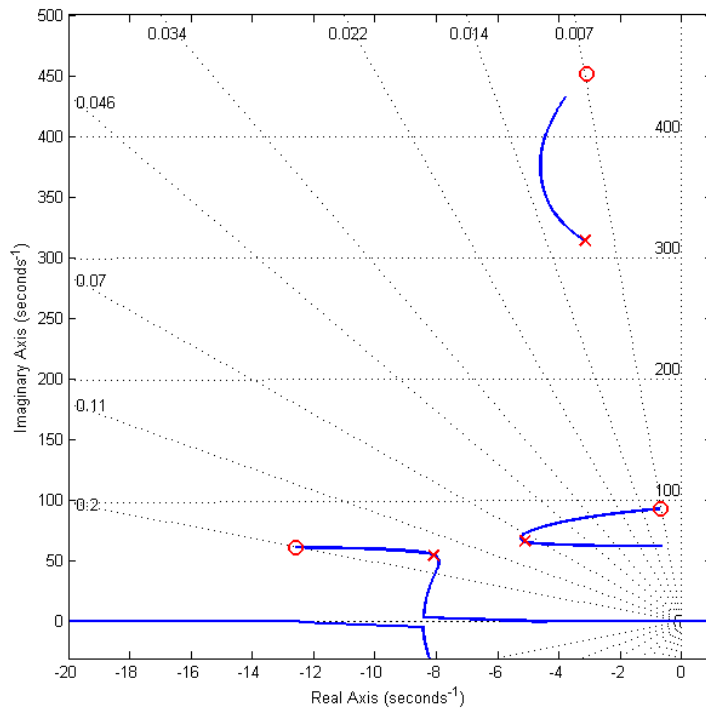


Figure 2-6 Root locus of $G(s)$ compensated by a PPF filter targeting the first mode

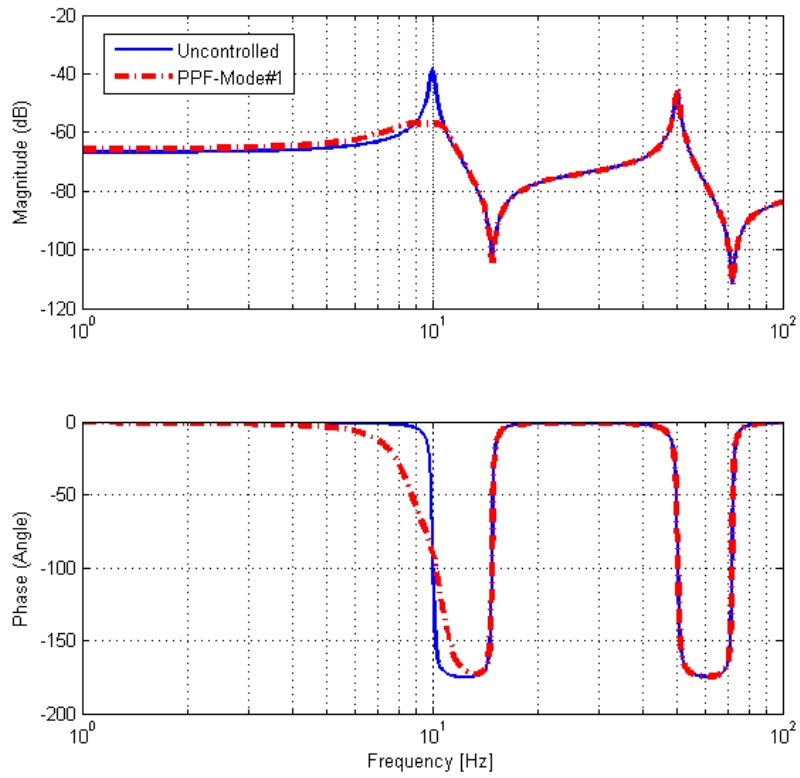


Figure 2-7 Bode plot of $G(s)$ compensated by a PPF filter targeting the first mode

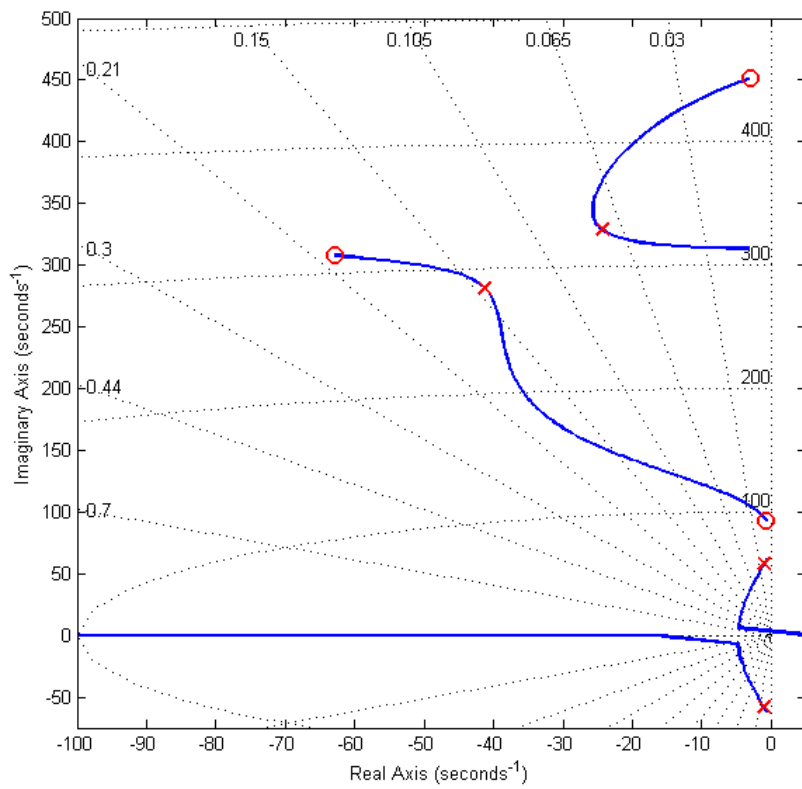


Figure 2-8 Root locus of $G(s)$ compensated by a PPF filter targeting the second mode

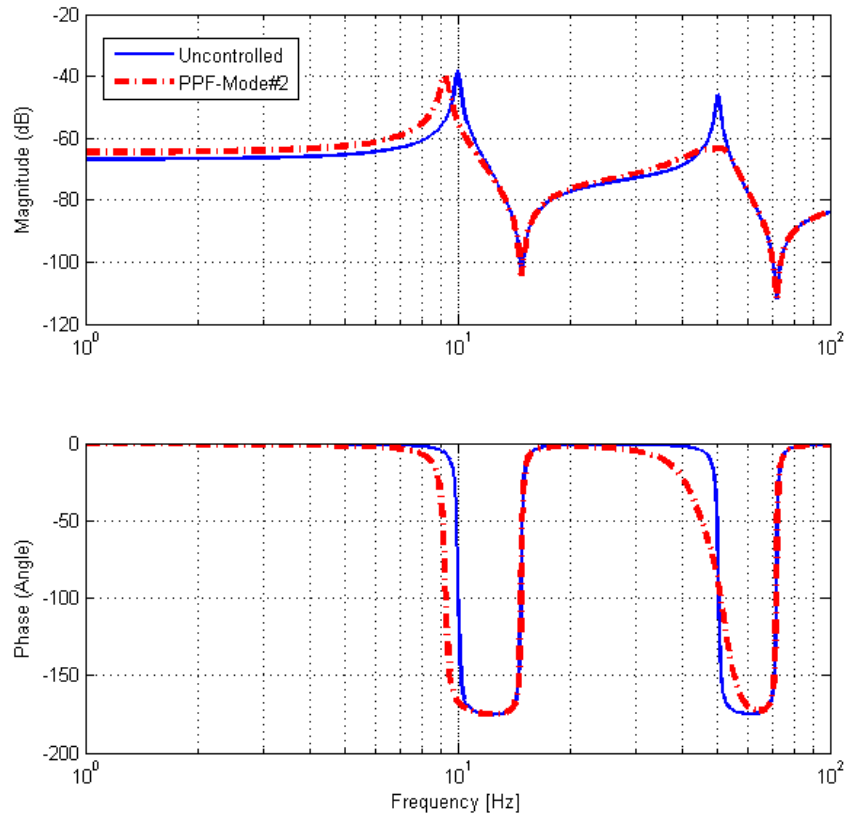


Figure 2-9 Bode plot of $G(s)$ compensated by a PPF filter targeting the second mode

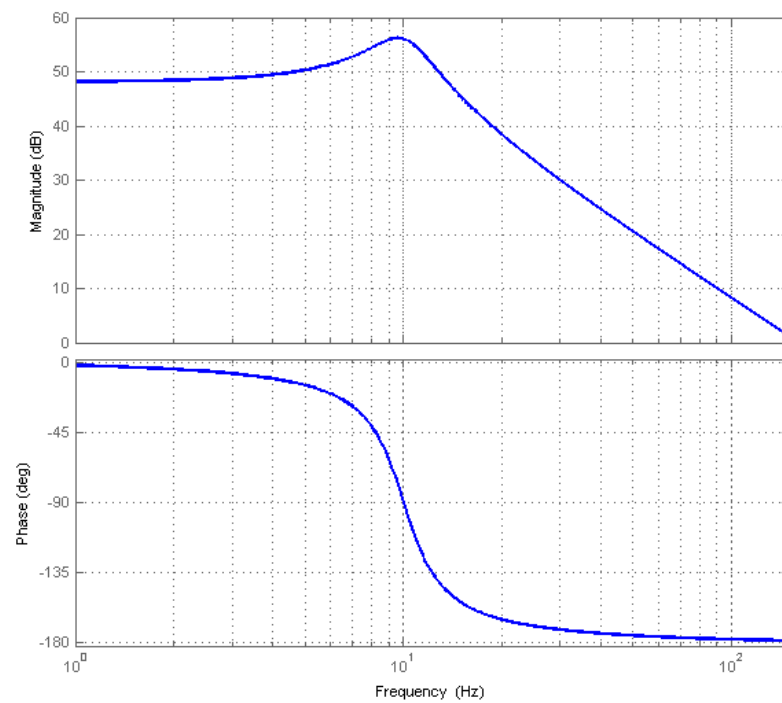


Figure 2-10 Bode plot of PPF filter targeting the first mode

2.3.3 Resonant Control (RC)

Resonant control method is also based on a second order filter, but works with negative feedback. Second order numerator dynamics convert the position feedback to acceleration feedback [41]. Transfer function of the second order positive position feedback compensator is given as

$$H(s) = \frac{-Ks^2}{s^2 + 2\zeta_f\omega_f s + \omega_f^2} \quad (2.21)$$

Several researches have used resonant control method [51–54]. Effects of RC compensators on a collocated transfer function are investigated by using the plant defined in (2.20). Parameters of the RC compensators targeting the first and the second modes are $K_1 = 3 \cdot 10^2$, $K_2 = 5 \cdot 10^2$, $\zeta_{f1} = \zeta_{f2} = 0.20$, $\omega_{f1} = 2\pi \cdot 10$ and $\omega_{f2} = 2\pi \cdot 50$.

Performances of RC compensators on the collocated transfer function are shown in Figure 2-11 to Figure 2-14. When these results are considered, the following conclusions can be drawn:

- RC compensator targeting the first mode also affects the response in the second mode by slightly increasing the natural frequency and modal damping ratio. This is a result of high-pass characteristic of RC compensator (*see Figure 2-15*) which causes amplification of sensor noise and endangers stability robustness when unmodeled dynamics and transportation lag are present.
- Filter tuned for the second mode does not affect the response around the first mode. High-pass characteristic prevents control spillover on low frequency modes. Hence, in order to control multiple modes, RC compensators targeting lower frequency modes should be tuned before the ones targeting higher frequency modes.

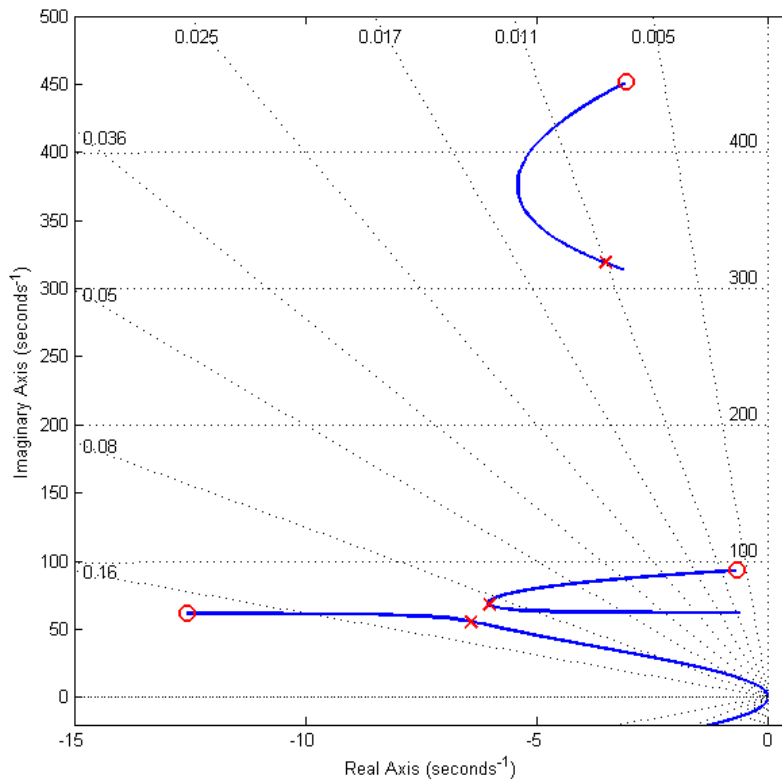


Figure 2-11 Root locus of $G(s)$ compensated by a RC compensator targeting the first mode

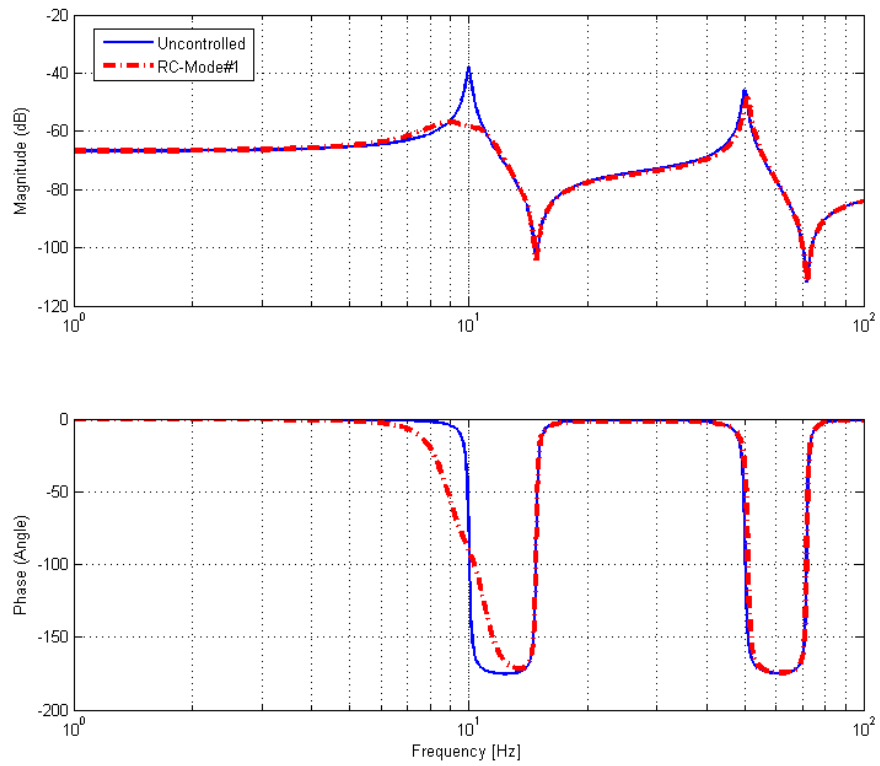


Figure 2-12 Bode plot of $G(s)$ compensated by a RC compensator targeting the first mode

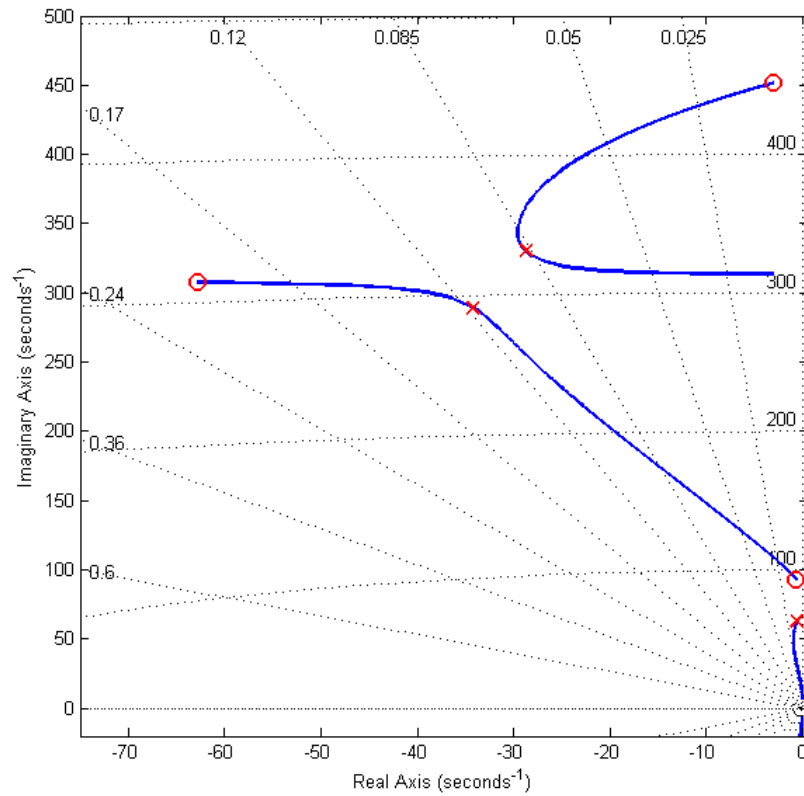


Figure 2-13 Root locus of $G(s)$ compensated by a RC compensator targeting the second mode

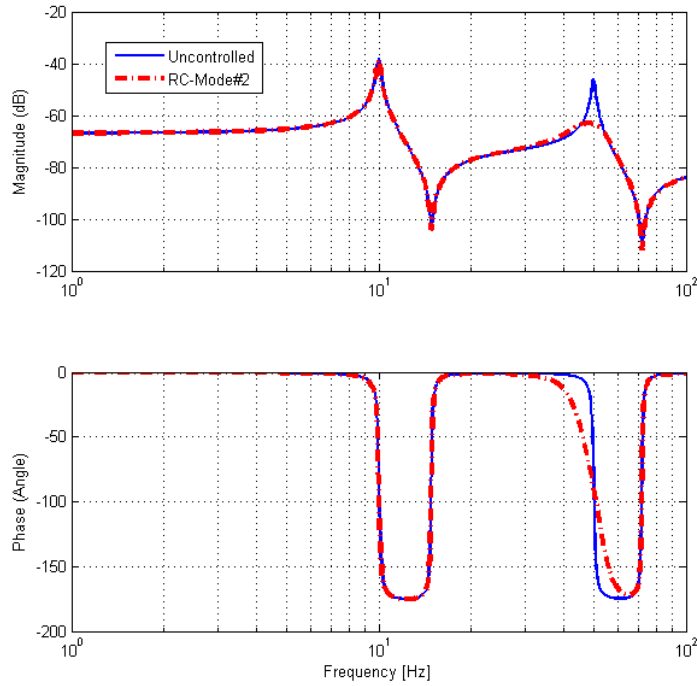


Figure 2-14 Bode plot of $G(s)$ compensated by a RC compensator targeting the second mode

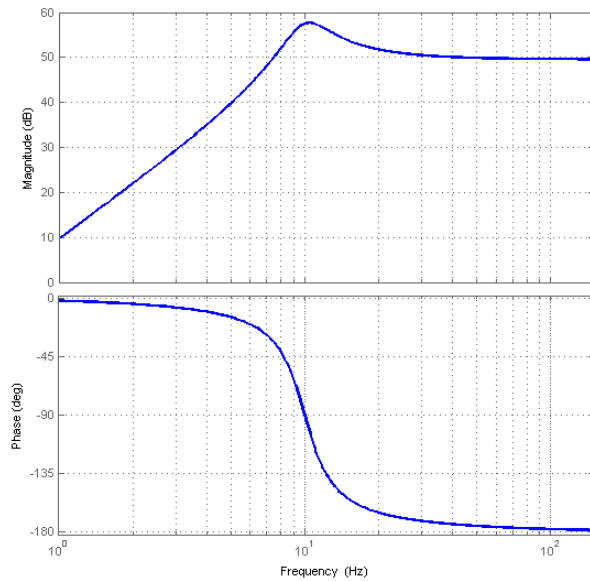


Figure 2-15 Bode plot of RC compensator targeting the second mode

2.3.4 Integral Resonant Control (IRC)

Integral Force Feedback (IFF) method is developed for control systems where displacement actuators, and force sensors are used [40]. That is to say, transfer function of the collocated system to be controlled with this method should represent the dynamic stiffness, not receptance. Hence, this collocated transfer function also shows pole-zero interlacing property but starts with a zero.

It has been proposed to connect a feed-through term to the collocated transfer function in order to convert a receptance type frequency response function (FRF) to a dynamic stiffness FRF [40,55,56].

In this method, a zero (anti-resonance) is placed before the first pole (natural frequency) of a collocated transfer function by the addition of a negative feed-through term. Proposed modification on IFF is called integral resonant control (IRC).

Originally integral resonant controller is a simple positive integrator, and given as:

$$H(s) = \frac{K}{s} \quad (2.22)$$

However, this integrator results in high static gains which may result in actuator saturation. Therefore, in order to reduce the gain in low frequencies two modified versions of IRC are proposed:

$$H(s) = \frac{K}{s + p} \quad (2.23)$$

$$H(s) = \frac{Ks}{(s + p)(s + p)} \quad (2.24)$$

While the first one is in the form of a low-pass filter, second one is a band-pass filter. Bode diagrams of different IRC transfer functions are given in Figure 2-16.

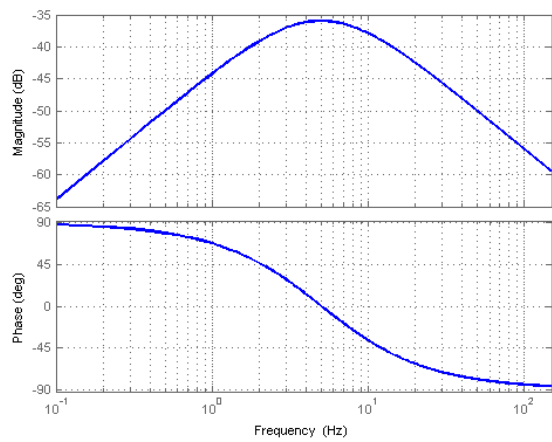
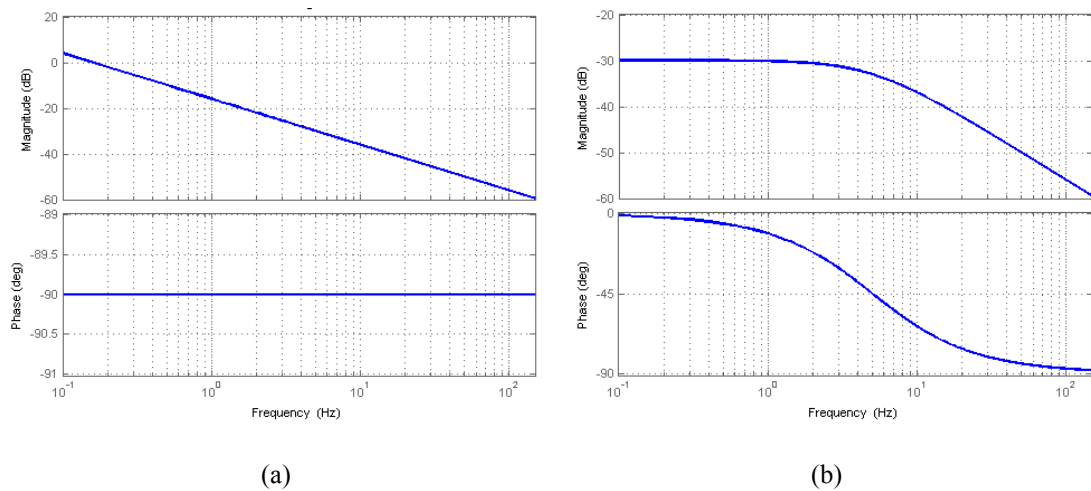


Figure 2-16 Bode plot of different IRC compensators. (a) simple integrator, (b) low-pass (c) band-pass

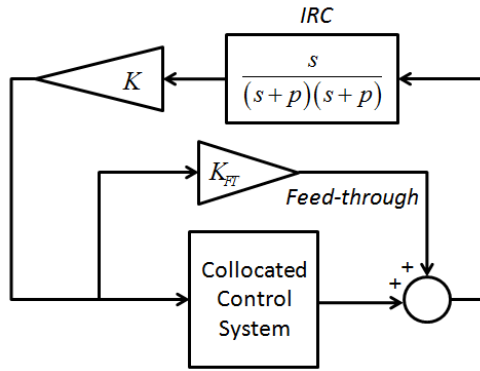


Figure 2-17 Band-pass integral resonant control scheme

A band-pass integral resonant controller (Figure 2-17) is implemented on the collocated transfer function defined in Equation (2.20). Parameters of this compensator are $K = 4 \cdot 10^5$, $p = 2\pi \cdot 1$ and $K_{FT} = -\text{Re}(G(j \cdot 2\pi \cdot 3)) = -4.8 \cdot 10^{-4}$. Effects of IRC compensator are shown on both root-locus and Bode diagrams in Figure 2-18 and Figure 2-19, respectively.

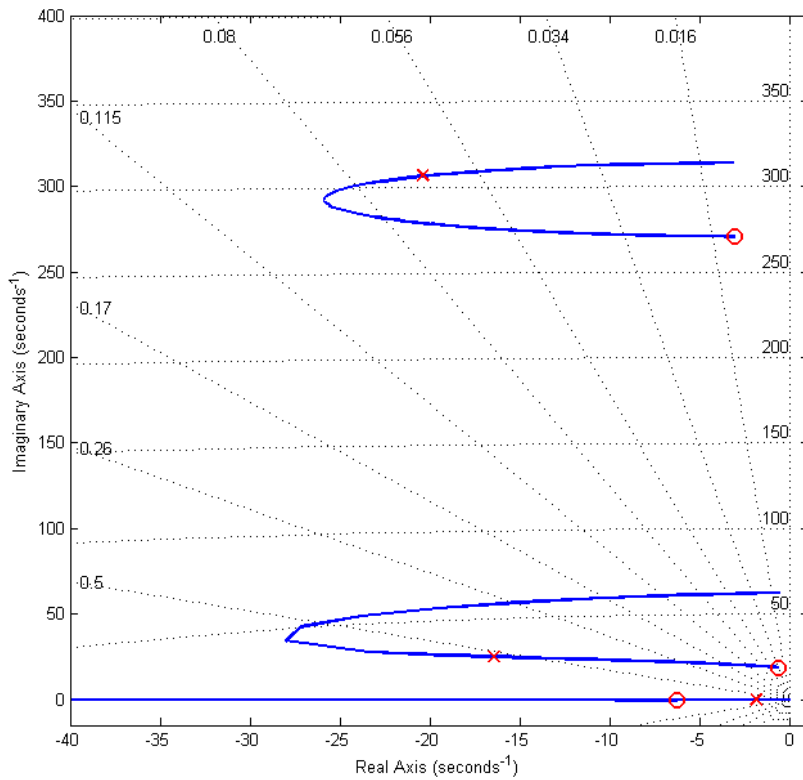


Figure 2-18 Root locus for band-pass IRC compensator

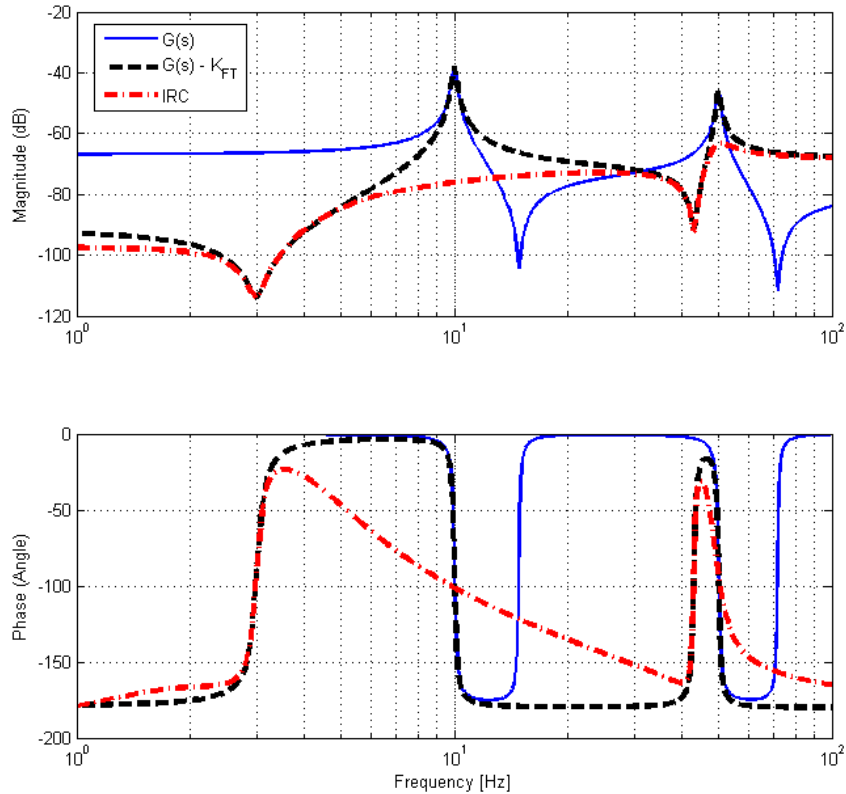


Figure 2-19 Effects of IRC compensator on frequency response

It can be seen that integral resonant control can suppress multiple modes. However, each mode cannot be treated separately. Additionally, since the control gain decreases at higher frequencies, method is less effective for high frequency modes.

2.3.5 Positive Position Feedback with Feed-through (PPFFT)

Positive position feedback is an effective collocated modal control method for damping augmentation. Ease of implementation, non-dynamic stability, low control spillover, minimal sensitivity to noise and unmodeled dynamics are the prominent properties of this method which still attract the researchers.

Of course, deficiencies of this method also exist, and one of them is the low frequency amplification [43,50,52]. This behavior can be seen in Figure 2-7 and Figure 2-9 which represent the results of single mode PPF control. In multi-mode control, mentioned amplification is cumulatively increased which leads to excessive control inputs at low frequencies. As a result of this behavior, controller becomes vulnerable to quasi-static response which causes saturation of the actuator in relatively low feedback gains.

In order to diminish quasi-static amplification behavior of PPF controller, addition of a negative feed-through term to the collocated transfer function is proposed in this study. This modified version of PPF method is named as positive position feedback with feed-through (PPFFT). Control scheme of the suggested method is given in Figure 2-20.

With suggested modification, a zero is placed before the first pole of the collocated transfer function; hence 180° phase lag is introduced between 0 Hz and the located zero. 180° phase lag converts the positive feedback to negative feedback for this frequency range. Hence, quasi-static amplification of PPF controller is reduced.

Effect of negative feed-through term is illustrated on the collocated transfer function defined in Equation (2.20). For example, if one desires to place a zero to 4 Hz, a negative feed-through term with

a magnitude of $K_{FT} = -\text{Re}(G(j \cdot 2\pi \cdot 4)) = -5.04 \cdot 10^{-4}$ should be connected to the collocated transfer function in parallel. Effect of negative feed-through addition on collocated transfer function is shown in Figure 2-21.

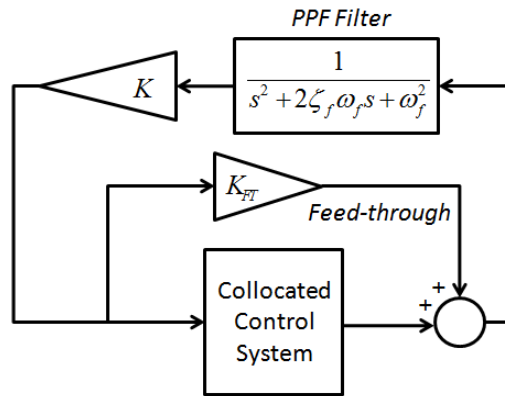


Figure 2-20 Single mode PPFFT control scheme

Addition of feed-through term to a collocated transfer function also changes the phase response characteristics. Frequencies of maximum negative imaginary response are lowered (*see Figure 2-21*). As a result, PPF filter frequencies should be selected lower than the natural frequencies of the targeted modes in PPFFT method.

Effects of PPFFT compensators on a collocated control system is investigated by using the plant defined in Equation (2.20). Parameters of two PPFFT compensators targeting the first and the second modes are $K_1 = 2 \cdot 10^7$, $K_2 = 7 \cdot 10^7$, $\zeta_{f1} = 0.90$, $\zeta_{f2} = 0.30$, $\omega_{f1} = 2\pi \cdot 8$ and $\omega_{f2} = 2\pi \cdot 45$. Performances of PPFFT compensators on the collocated transfer function are shown in Figure 2-22 to Figure 2-25.

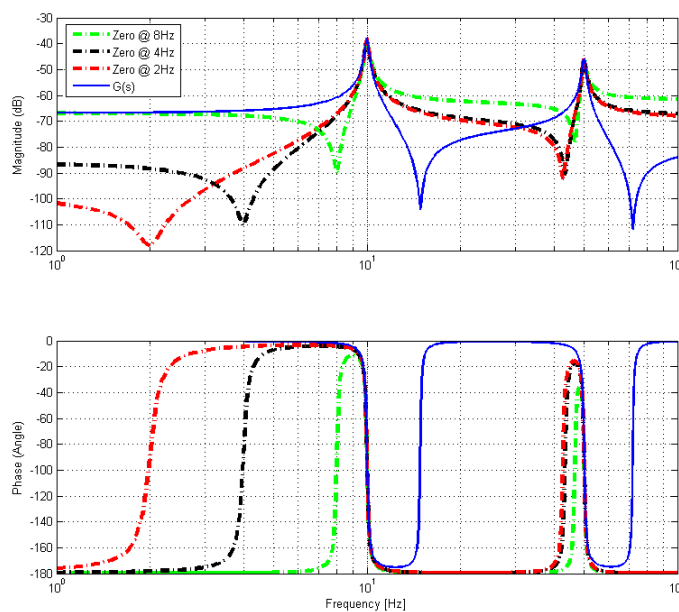


Figure 2-21 Effect of feed-through addition on collocated transfer function

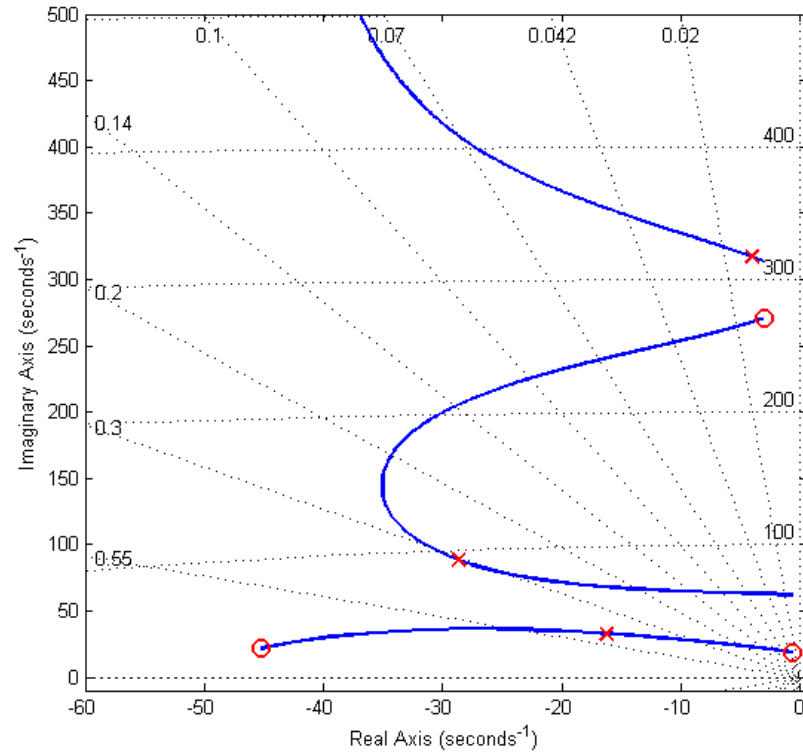


Figure 2-22 Root locus of $G(s)$ compensated by a PPFFT controller targeting the first mode

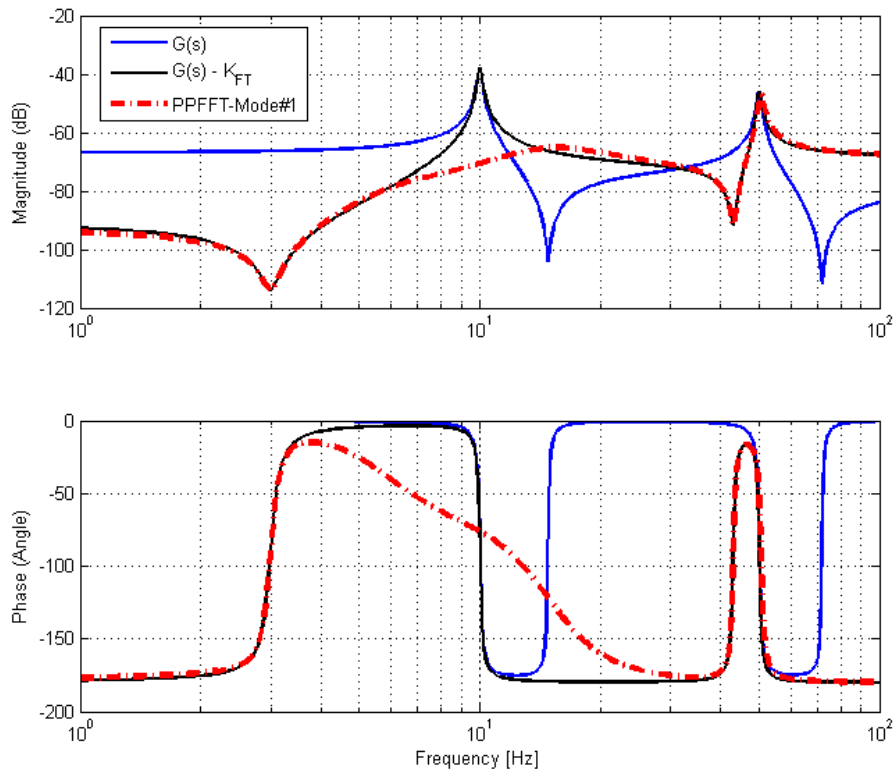


Figure 2-23 Bode plot of $G(s)$ compensated by a PPFFT controller targeting the first mode

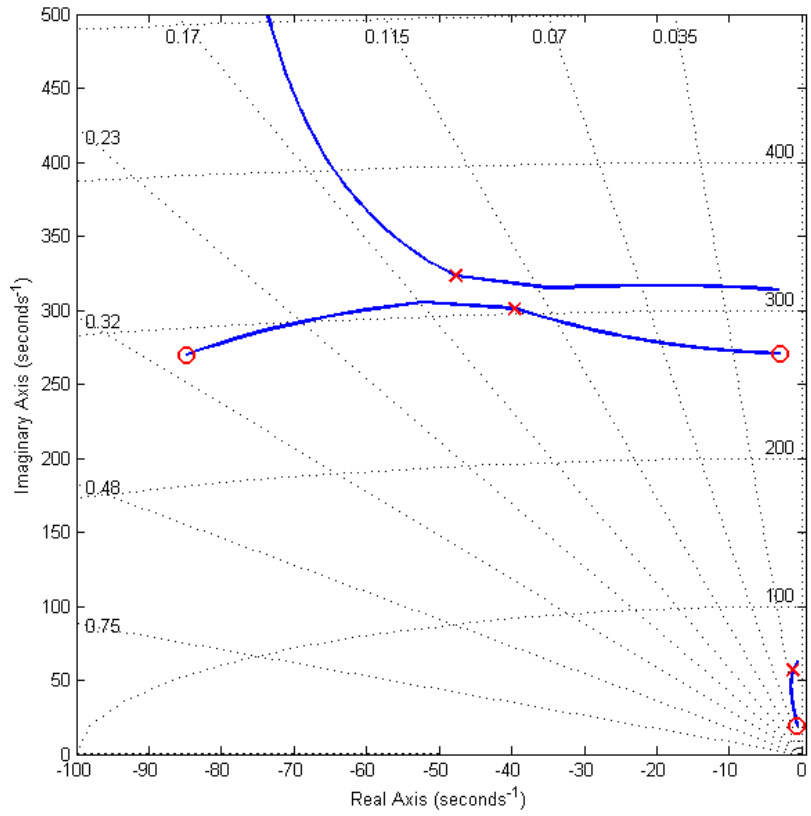


Figure 2-24 Root locus of $G(s)$ compensated by a PPFFT controller targeting the second mode

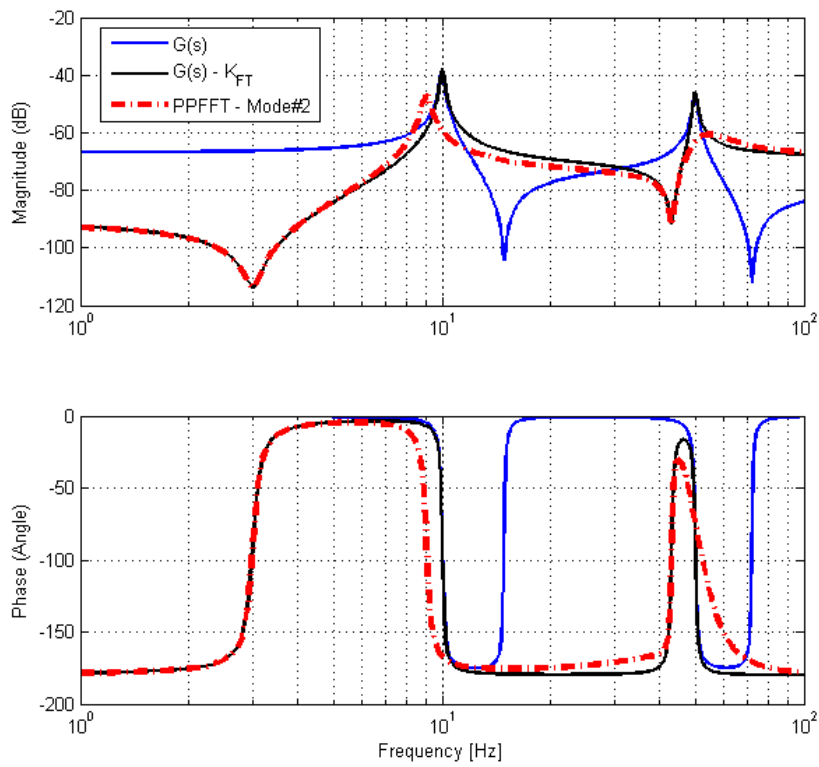


Figure 2-25 Bode plot of $G(s)$ compensated by a PPFFT controller targeting the second mode

When the effects of PPFFT compensators are examined, the following conclusions can be drawn:

- Filter tuned for the second mode shifts the first pole to a lower frequency with higher damping. Hence, in order to control multiple modes, PPFFT controllers targeting higher frequency modes should be tuned before the ones targeting lower frequency modes.
- Both compensators diminish the response in quasi-static region. Hence, it is shown that an important problem of PPF method can be resolved by the addition of a negative feed-through term.

2.4 Placement of Piezoelectric Sensors and Actuators

Piezoelectric materials can be embedded in the structure or they can be surface mounted in the form of distributed layers or patches with smaller sizes. Theoretical study of Tzou and Fu [57] showed that segmented layers of actuators and sensors show better performance than distributed layers in terms of both controllability and observability. The problem in distributed form is identified as the canceling of the charges with different polarities over the entire actuator and sensor surface.

Locations of piezoelectric patches on the host structure affect the performance of the vibration control system significantly [58]. Moreover, misplaced actuator/sensor pairs can cause destabilization of even if they are collocated [59]. For this reason, locations of the piezoelectric actuator/sensor pairs should be selected carefully.

Numerous location alternatives can be generated on the surface of a structure for piezoelectric patch mounting. Selection of the most convenient piezoelectric patch locations is an optimality problem which needs an optimization criterion and method.

Different optimization algorithms have been suggested to solve the mentioned optimality problem. Genetic algorithms [17,60–64] discrete direct pattern search [65], simulated annealing [66] are some examples of optimization methods used in literature. These methods are tools in order to find the best alternatives for the defined optimization criterion. Hence, more attention should be paid on the definition of the optimization criterion.

One of the optimization criteria used in literature is to maximize the modal control forces/moments of the piezoelectric actuators [58]. Bin et al. [67] adopted this optimization criterion and applied on a cantilever plate. They derived the modal control force (Q_j) for the j^{th} mode as

$$Q_j(t) = -a_p b_p \left(\frac{h_p + h_s}{2} \right) L [\psi_j] V_i(t) \quad (2.25)$$

where

$$L = e_{31} \left\{ \left(\frac{\partial^2}{\partial x^2} \right) + \left(\frac{\partial^2}{\partial y^2} \right) \right\} \quad (2.26)$$

Subscripts p and s denote the piezoelectric patch and structure, respectively. Length, width and height are symbolized as a , b and h , respectively. While ψ_j is indicating the normalized modal function for the j^{th} mode, $V_i(t)$ denotes the electric potential on i^{th} piezoelectric patch at time t . At the end of their study, it is concluded that piezoelectric patches should be placed to regions of maximum modal strains in order to produce maximum modal forces in relevant modes.

In some researches, it has been claimed that optimal positions of piezoelectric actuators are the locations where host structure can be deflected maximum [21,68–70]. Hence suggested optimization criterion is the maximization of host structure deformation by piezoelectric actuators. An example of these researches is the work of Yang and Zhang [70] on a simply supported plate. They proposed the

maximization of ‘position mode function’, $\chi_{j,k}$, to find an actuator position maximizing deflection of the host structure at particular mode (j, k) . Definition of this function is given as follows:

$$\chi_{j,k} = \sin^2(j\pi\alpha_0)\sin^2(k\pi\beta_0) \quad (2.27)$$

where α_0 and β_0 denotes the normalized length and width positions of a piezoelectric actuator’s midpoint, respectively. Their study shows that anti-nodes of a mode are the best actuator location alternatives for relevant mode in terms of maximum host structure deformation.

Minimization of control effort and/or maximization of dissipated energy are other optimization criteria for placing piezoelectric actuators to optimal positions [58]. If both criteria are considered simultaneously, performance index of a LQR control should be defined as:

$$J = \int_0^{\infty} (\dot{X}^T Q X + V_{act}^T R V_{act}) dt \quad (2.28)$$

where V_{act} , Q and R refer external control voltage, weighing matrices for energy dissipation and control effort. State-space in Equation (2.28) is represented in modal domain which is given by

$$\begin{aligned} \dot{X}(t) &= AX(t) + BV_{act}(t) \\ Y(t) &= CX(t) \end{aligned} \quad (2.29)$$

Hence, optimal value of the performance index can be defined by

$$\text{Minimize } J = tr[P] \quad (2.30)$$

where P is the solution of algebraic Riccati equation.

In their study, Kumar and Narayanan [71] took the simultaneous minimization of control effort and maximization of dissipated energy while using an LQR controller with full-state feedback. Results of their optimization study showed that optimal locations of actuator/sensor pairs are the regions of high modal strain energy.

Controllability can be defined as the capability of an external input to change internal states of a system from any final state in a finite time interval [72] and it can be checked over rank of controllability matrix:

$$R = [B \quad AB \quad \dots \quad A^{n-1}B] \quad (2.31)$$

However, this controllability check only gives the information that system is controllable or not controllable. Hence, this information is not sufficient while deciding the locations of the piezoelectric patches in structural control.

In order to measure the degree of controllability, some criteria have been developed. Controllability gramian is a matrix

$$G_c = \int_0^{\infty} e^{At} B B^T e^{A^T t} dt \quad (2.32)$$

showing the degree of controllability of a control system [73]. Hence, minimization of control effort means the maximization of controllability gramian. Also, eigenvalues of controllability gramian matrix are indicators of the degree of controllability. In some researches [17,74], optimal piezoelectric actuator locations are determined with following criteria

$$J = \left(\sum_{j=1}^{2n} \lambda_j \right) \sqrt[2n]{\prod_{j=1}^{2n} (\lambda_j)} \quad (2.33)$$

$$J = \text{tr}[G_c] * (\det G_c)^{1/2n} \quad (2.34)$$

based on the eigenvalues (λ_j) of controllability gramian matrix. Since diagonal elements of controllability gramian matrix are indicators of the controllability of individual modes, maximization of each diagonal term of controllability gramian matrix

$$J = \max \{ (G_c)_{11} \quad (G_c)_{22} \quad \dots \quad (G_c)_{nn} \} \quad (2.35)$$

can also be defined as the optimization criterion [74].

Singular values (κ) of control input matrix (B) in Equation (2.29) are indicators of modal control forces. These values obtained by singular value decomposition can be used in maximization of modal control forces. Wang and Wang [75] suggested maximizing the product of these values in order to obtain maximum modal control forces:

$$\Gamma = \prod_{i=1}^n \kappa_i \quad (2.36)$$

H_2 norm of a transfer function indicates the expected root mean square value of the output for an input with unit variance and white noise spectrum. By using this property, square of H_2 norm of a transfer function (G) between electric potential on piezoelectric actuator input and response of a location on the structure to be controlled can also be used as an optimization criterion [76]

$$\|G(r_1)\|_2^2 = \frac{1}{2\pi} \int_{-\infty}^{\infty} \text{tr} \{ G(r_1) G(r_1)^* \} dw \quad (2.37)$$

where r_1 symbolize the location of the piezoelectric actuator. If the response of entire structure is considered, square of H_2 norm of a transfer function (G) in spatial form

$$\langle\langle G \rangle\rangle_2^2 = \frac{1}{2\pi} \int_{-\infty}^{+\infty} \int_R \text{tr} \{ G(r_1) G(r_1)^* \} dr dw \quad (2.38)$$

can be used as optimization criterion by taking advantage of Maxwell's reciprocity theorem [76].

If piezoelectric patches, or other strain measuring instruments, are used as sensors of an active vibration control system, indices defined for degree of observability are almost the same as the ones used to measure degree of controllability [58,73,74], since working principles of both piezoelectric actuators and sensor are both strain based. For instance, instead of using controllability gramian, observability gramian is used for maximization of the degree of observability of a control system [73]:

$$G_o = \int_0^{\infty} e^{At} C C^T e^{A^T t} dt \quad (2.39)$$

The change is replacement of control input matrix (B) with the control output matrix (C). Hence, for a collocated actuator/sensor pair, modal observability and controllability criteria are equivalent [77,78]. Study of Qiu et al. [79] also showed that optimum sensor and actuator locations are the same in case they are collocated.

In their technical review on optimization criteria for optimal piezoelectric patch placement [58], Gupta et al. summarized the prominent criteria and researches. Moreover, results of optimal piezoelectric actuator/sensor placement studies for different boundary conditions of plate are presented in tabulated form. This table is given, as is, in Table 2-3. By considering the results given in this table, the following conclusions can be drawn:

- Optimal actuator/sensor locations for each mode are different.
- Different optimization criteria and boundary conditions may lead different locations of piezoelectric actuators and sensors.
- For cantilever boundary condition, actuators should be on the cantilevered edge for low frequency modes. Regions of maximum modal strain energy are also elaborated in order to maximize controllability and modal forces/moments.
- For simply supported boundary condition, placing actuators to anti-nodes and regions between nodal lines are more effective in terms of maximizing deformation of the host structure and controllability.

Table 2-3 Optimal locations of surface bonded piezoelectric sensor/actuator patches on a plate [58]

| Criterion | Boundary condition | Modes to be controlled | Sensor and actuator locations | Source |
|---|----------------------------------|------------------------|--|--|
| Maximizing modal forces/moments applied by actuator | Cantilevered | First | Two actuators adjacent to each other at mid-point of the cantilevered edge | (Bin et al., 2000) |
| | | Second | Two actuators at extreme corners of the cantilevered edge | |
| | | Third | One actuator at 0.25 times length of cantilevered edge on the cantilevered edge and second actuator at 0.75 times length of cantilevered edge on the cantilevered edge | |
| Maximizing deflection of the host structure | Cantilevered | First | Actuator close to the middle of cantilevered edge | (Ip and Tse, 2001) |
| | | Second and Third | Actuators near the corner of the cantilevered edge | |
| | | Fourth and Fifth | Actuators at anti-nodes | |
| | Cantilevered | First | Collocated sensor–actuator pair must be located near the centerline along the cantilevered edge | (Quek et al., 2003) |
| | | Second | One edge of the collocated sensor–actuator pair is on the free edge of the plate and the other edge is on the cantilevered edge of the plate | |
| | | First and Second | One collocated sensor–actuator pair is placed at the centerline along the cantilevered edge and other is placed adjacent to it along the cantilevered edge | |
| | Simply Supported | First five | Actuators at anti-nodes of modes of interest | (Ip and Tse, 2001; Yang and Zhang, 2006) |
| Minimizing the control efforts | Cantilevered | First and Third | Actuators should cover areas of high strain | (Kim and Kim, 2005) |
| | | Second and Fourth | Optimal distribution of piezoelectric actuator layer is asymmetric | |
| Optimal value of LQR performance index | Cantilevered | First six | Five collocated sensor–actuator pairs at maximum modal strain energies of first two modes, two at maximum modal strain energies of fourth mode, and three around the center of the plate | (Kumar and Narayanan, 2007) |
| Expected value of LQR performance index | Cantilevered (Plate shaped wing) | First torsion mode | Two actuators at leading and trailing edge of the root, one at the edge of the tip, and one at the mid cord of the out board region | (Nam et al., 1996) |
| Maximizing degree of controllability | Cantilevered | First five | Two actuators at extreme corners of cantilevered edge and two adjacent to each other near center of the plate | (Peng et al., 2005) |
| | Simply Supported | First | Actuator at middle of the plate | (Halim and Moheimani, 2003) |
| Maximizing degree of observability and minimizing spillover effects | Cantilevered | First four | Actuators between nodal lines | (Sadri et al., 1999) |
| | | First three | One sensor at one end of cantilevered edge, two actuators exactly below this sensor placed adjacent to each other, and another sensor at other cantilevered end | (Han and Lee, 1999) |

In order to understand the importance of the locations which are presented as optimal, a plate with dimensions 700 x 400 x 1.5 mm (with the same size of plate studied in Chapter 4) is analyzed for two different boundary conditions, one cantilevered edge (the one with 400 mm length) and four simply supported edges.

When the mode shapes (Figure 2-26) and modal strain energy distributions (Figure 2-27) of the cantilever plate are examined, it is seen that maximum strain energy regions are:

- At the center of the cantilevered edge for the first bending mode,
- Near the corners of the cantilevered edge for the first torsion mode.
- Between the center and corner of the cantilevered edge for the second bending mode.

If the results of the studies in Table 2-3 are examined, it can be seen that maximum modal strain energy regions given above coincide with the optimal actuator location conclusions of most of the studies [65,67,68,71,80].

Mode shapes and strain energy distributions of the simply supported plate for the first five modes are given in Figure 2-28 and Figure 2-29, respectively. When the figures are studied, it can be concluded that anti-node locations (which are presented as optimal locations in [62,68,70,78]) are also the regions of maximum strain energy.

Results obtained for both cantilever and simply supported plate show that optimal piezoelectric actuator locations, which have been found using several optimization criteria, indicate the regions of high modal strain energy. Hence, it is decided to use modal strain energy for determining the collocated actuator/sensor locations in this study.

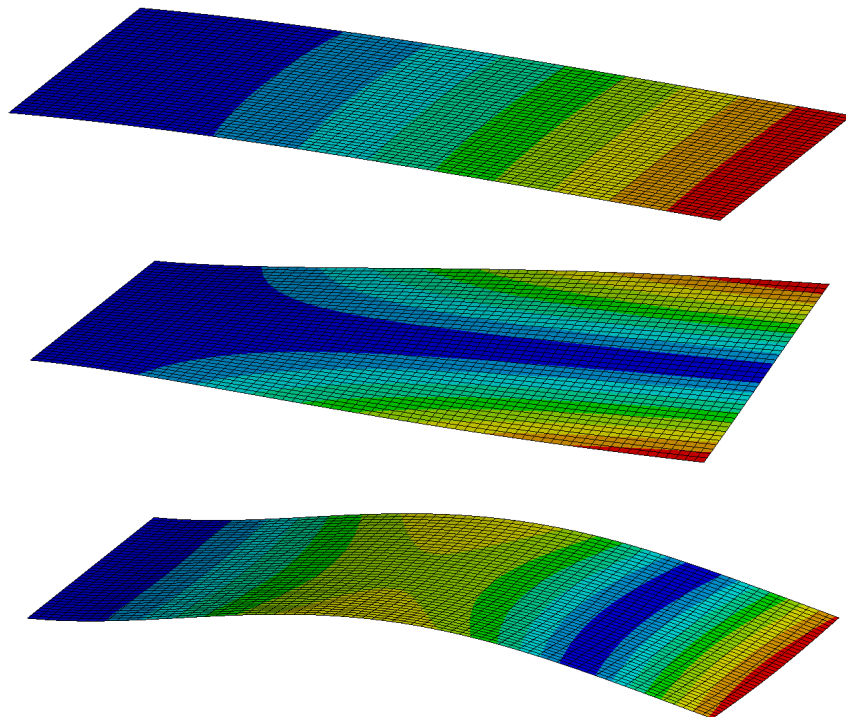


Figure 2-26 First three mode shapes of the cantilever plate

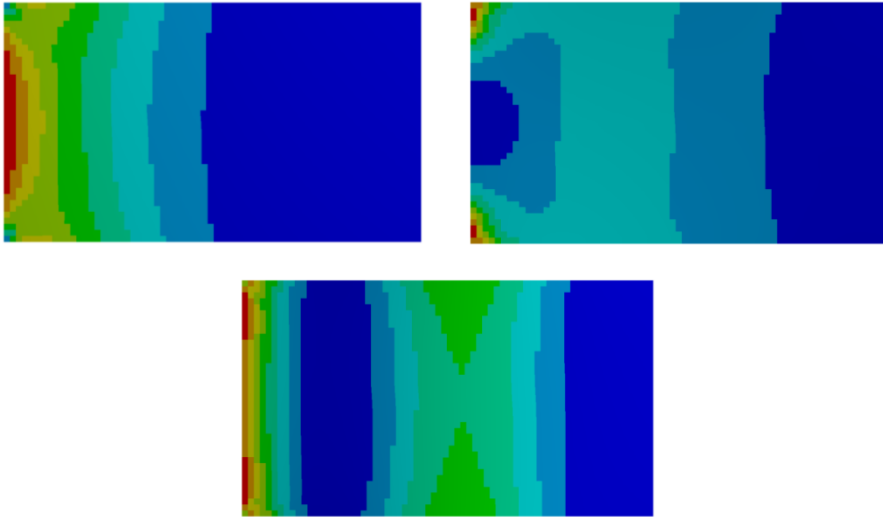


Figure 2-27 Strain energy distribution of the cantilever plate for the first three modes

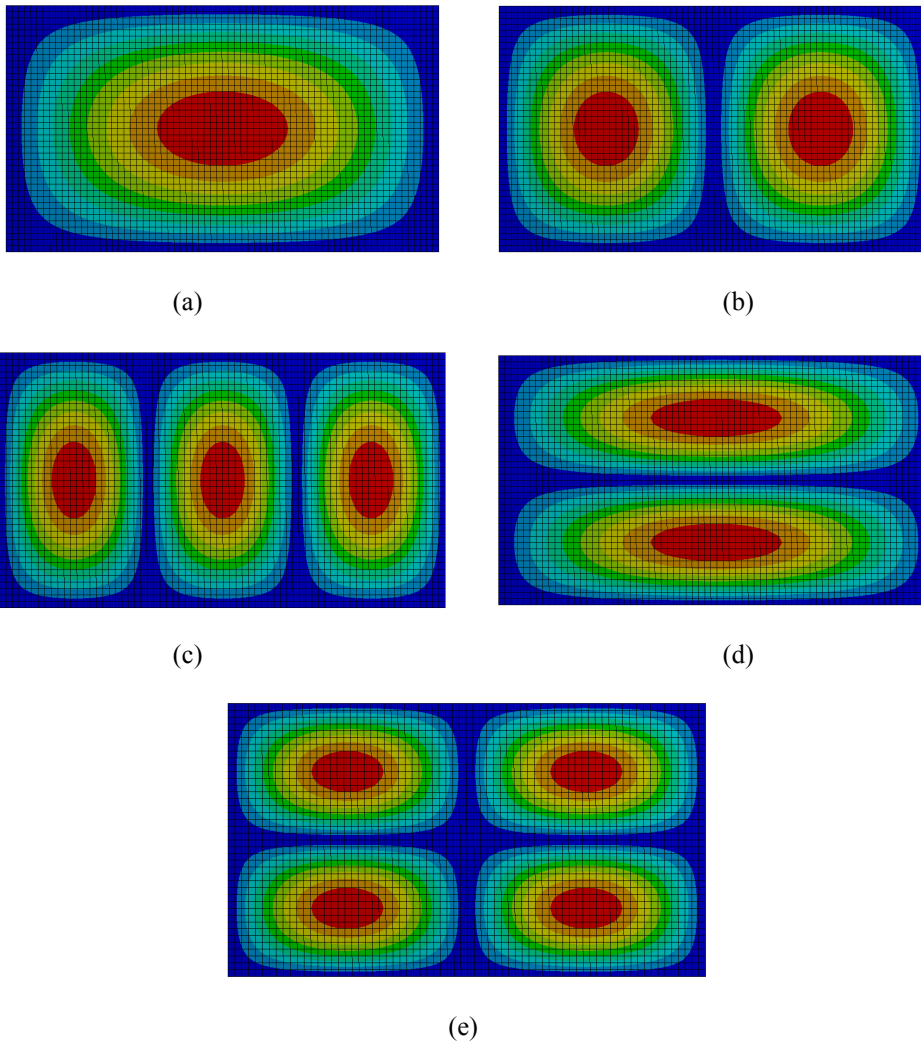


Figure 2-28 First five mode shapes of the simply supported plate.

(a): (1,1), (b): (2,1), (c): (3,1), (d): (1,2) and (e): (2,2)

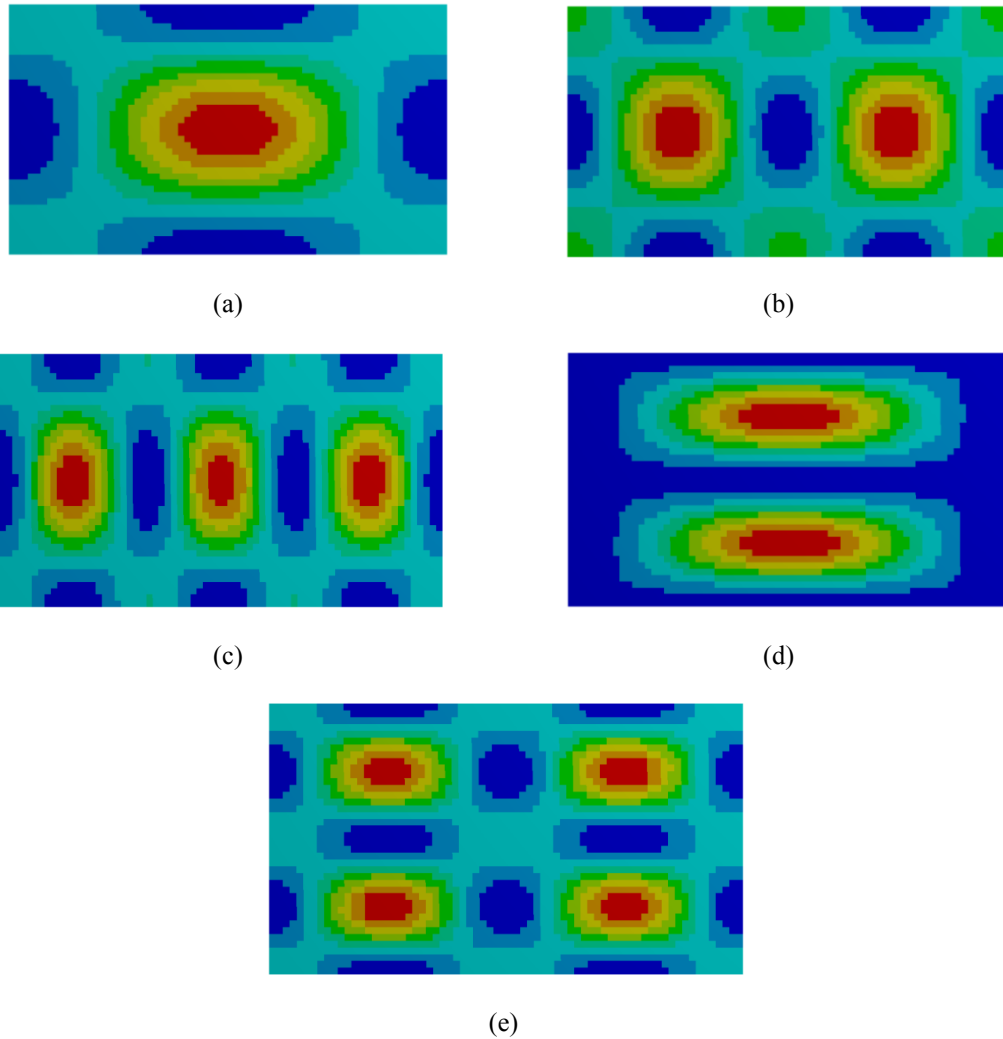


Figure 2-29 Strain energy distribution of the simply supported plate for the first five modes.

(a): (1,1), (b): (2,1), (c): (3,1), (d): (1,2) and (e): (2,2)

2.5 Summary

In this chapter, initially conceptual information on piezoelectricity and piezoelectric material is given. Then derivation of linear constitutive equations of piezoelectricity is presented. By using these equations, required material properties to model piezoelectric behavior in ANSYS are specified. Piezoelectric element types in ANSYS and the coupled finite element matrix equations are also presented.

In the first part of Section 2.3, background information on collocated transfer functions and collocated control is given. Afterwards, details of three different collocated modal control methods (PPF, RC and IRC) are explained with an illustrative problem. Also design of a PPF controller, proposed in this study, is shown on the same problem.

Piezoelectric actuator/sensor placement problem is discussed in Section 2.4. Studies on different optimization criteria and their results are presented. Finally, it has been shown that even if different optimization criteria are used, most of the studies point out high modal strain energy regions. Hence, modal strain energy method is used in this study to locate collocated actuators and sensors.

CHAPTER 3

ACTIVE VIBRATION CONTROL OF A CANTILEVER BEAM

3.1 Introduction

The study presented in this chapter has been dedicated to establish a design process for active vibration control of complex structures with piezoelectric materials. A relatively simple structure, cantilevered beam (1D), has been selected to implement the suggested procedure which is given in Figure 3-1.

Using a commercial finite element software package is a relatively easy way of modeling complex structures in multiphysics domain. In opposition to general trend of using ANSYS Classic for finite element modeling of piezoelectric materials, ANSYS Workbench is preferred for plant modeling in this study. The reason of this choice is the usability of this environment while dealing with complicated models. Although ANSYS Workbench environment is not yet fully supporting piezoelectric modeling, it enables using ANSYS Parametric Design Language (APDL) scripts with command snippets. This method has been used in this study.

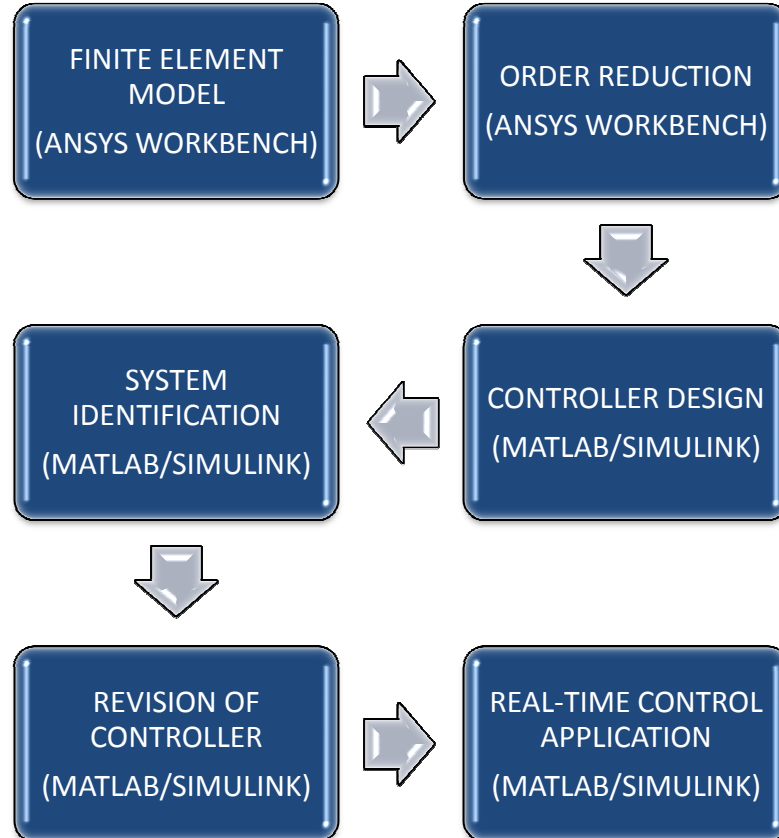


Figure 3-1 Proposed simulation procedure for active vibration control with piezoelectric materials

A successful control action requires, more or less, knowledge on the behavior of the plant. Finite element (FE) modeling is one of the most common ways of extracting this information from a flexible structure. However, FE models contain excessive information (related to all DOFs), some of which will not be needed in controller designs and simulations. Therefore, size of this information should be reduced in order to obviate the waste computation time. This phase, called order reduction, has also been accomplished in ANSYS Workbench by using a specialized APDL command.

A simulation environment which will present the required opportunities for controller design phase is strongly needed. For this purpose, model-based control actions are implemented using another commercial software package, MATLAB/Simulink R2010b.

Some discrepancies always exist between numerical simulations and real-life applications. Likewise, finite element models may not represent the dynamics of the structures properly. For this reason, dynamics of a real structure should be obtained with experiments. Afterwards, it is aimed to acquire a mathematical model of the structure for further control applications. This study, called as system identification, is achieved in MATLAB.

Experimental validation is indispensable to develop such a simulation methodology. MATLAB Real-Time Windows Target software is used for rapid control prototyping. Results of structural dynamics (natural frequency, damping, frequency response functions etc.) and control simulations (closed-loop time and frequency response characteristics) are compared with the ones obtained by experiments.

3.2 Plant Modeling

As mentioned earlier, a cantilevered beam structure is selected to be studied on. Dimensions of the aluminum beam (450 x 35 x 2.5 mm) and the piezoceramics (50 x 30 x 0.2 mm, PI DuraAct P-876.A12, *see Appendix A for details*) are given in Figure 3-2.

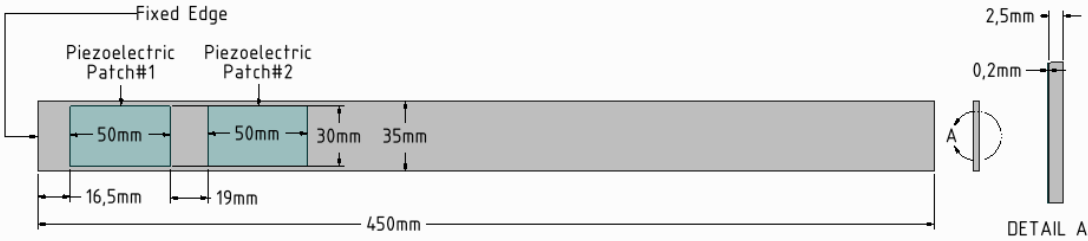


Figure 3-2 Dimensions of the structure to be controlled

Mechanical and electrical material properties of the aluminum beam and ceramic of the piezoelectric patch (PIC 255) are given in Table 3-1. Only mass effect of the electrical insulation layer is included in piezoelectric patch model due to its relatively small stiffness contribution compared to piezoceramic material. Command snippet to define Z-polarized piezoelectric material properties are given in Appendix B.

Table 3-1 Material properties of aluminum and PIC 255

| <i>Aluminum</i> | | <i>PIC 255</i> | | | |
|-----------------|------------------------|----------------|------------------------|------------------------------|-------------|
| ρ | 2770 kg/m ³ | ρ | 7800 kg/m ³ | C_{66}^E | 23.2 GPa |
| E | 69 GPa | C_{11}^E | 123 GPa | e_{31} | -7.15 N/V.m |
| ν | 0.33 | C_{12}^E | 76.7 GPa | e_{33} | 13.7 N/V.m |
| | | C_{13}^E | 70.3 GPa | e_{15} | 11.9 N/V.m |
| | | C_{33}^E | 97.1 GPa | $\epsilon_{11}^S/\epsilon_0$ | 930 |
| | | C_{44}^E | 22.3 GPa | $\epsilon_{33}^S/\epsilon_0$ | 857 |

8 node SOLID5 and 8 node SOLID185 element types are selected for piezoelectric and aluminum materials, respectively. Finite element mesh of the model is shown in Figure 3-3. The first six natural frequencies are calculated for short-circuited electrodes configuration. Results are given in Table 3-2.

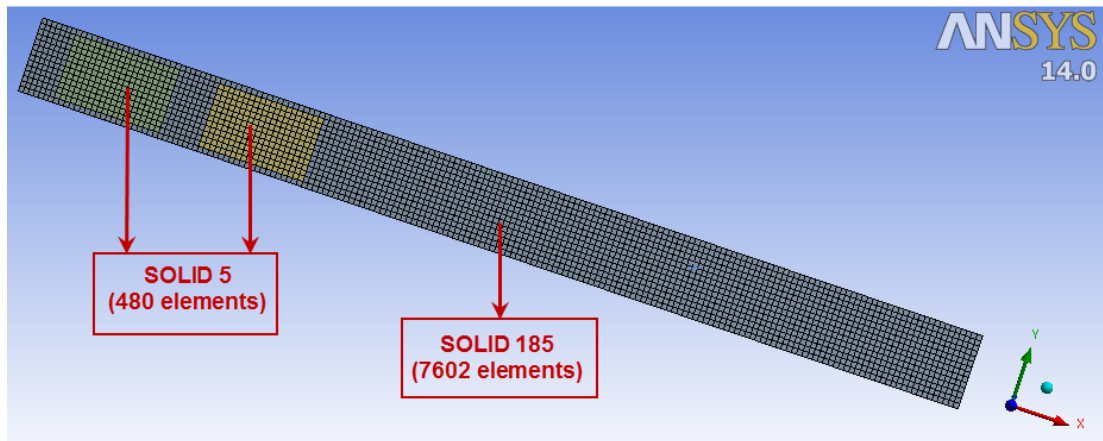


Figure 3-3 Finite element mesh of the model

Table 3-2 First six natural frequencies of the structure

| Mode | Frequency [Hz] | Mode | Frequency [Hz] |
|-------------------------|----------------|-------------------------|----------------|
| 1 st Bending | 10.51 | 3 rd Bending | 173.30 |
| 2 nd Bending | 63.03 | 1 st Torsion | 251.66 |
| 1 st Lateral | 140.46 | 4 th Bending | 339.55 |

In this stage of the process, there is no information at hand about modal damping ratios of the structure to be controlled. Hence, an assumption should be made to define damping properties. In the simulation phase of this study, it is aimed to acquire a damping ratio about 1% for the first and second bending modes. For this reason, Rayleigh damping model, supported by modal, harmonic and

transient response analyses solvers of ANSYS, is selected. By solving the following equations simultaneously:

$$\xi_1 = \frac{\alpha}{2\omega_1} + \frac{\beta\omega_1}{2} \Rightarrow 0.01 = \frac{\alpha}{2 \cdot (2 \cdot \pi \cdot 10.51)} + \frac{\beta(2 \cdot \pi \cdot 10.51)}{2} \quad (3.1)$$

$$\xi_2 = \frac{\alpha}{2\omega_2} + \frac{\beta\omega_2}{2} \Rightarrow 0.01 = \frac{\alpha}{2 \cdot (2 \cdot \pi \cdot 63.03)} + \frac{\beta(2 \cdot \pi \cdot 63.03)}{2} \quad (3.2)$$

required alpha and beta damping coefficients are selected as:

$$\Rightarrow \alpha = 1.1317 \ \& \ \beta = 4.328 \cdot 10^{-5} \quad (3.3)$$

Resulting damping spectrum is plotted in Figure 3-4.

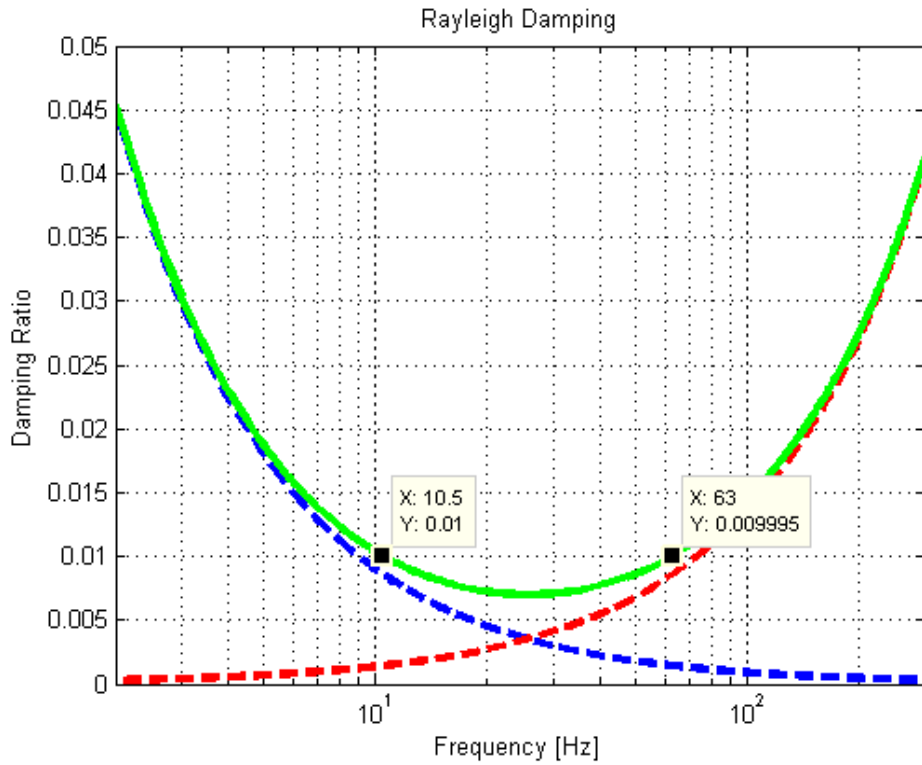


Figure 3-4 Defined Rayleigh damping spectrum

3.3 Order Reduction

Since the created finite element model contains information of numerous nodes, its use in control simulations becomes very time-consuming. A model describing the dynamic behavior of the structure with fewer equations is needed to solve this problem. For this reason, a model order reduction procedure, which has not yet taken part in literature, is suggested. With this procedure, input-output relationships can be exported in state-space representation from the modal analysis results obtained by ANSYS.

SPMWRITE command is a useful tool for exporting state-space matrices even for coupled (e.g. piezoelectric) analyses. While using this command, mode-extraction method, number of modes to be

used, damping properties, load inputs and requested outputs should be defined prior to a modal analysis (see Appendix C). Then, state-space matrices are written to a text file (.spm file) for defined nodal translation and/or rotational outputs. A sample SPM file in dense format can be found in Appendix D. MATLAB script parsing the generated SPM file is given in Appendix E.

States (X) of the state-space representation ($\dot{X} = AX + BU$ & $Y = CX + DU$) are obtained by converting the n second order modal equations, representing n uncoupled modes, to $2n$ first order equations:

$$X = \begin{Bmatrix} \eta_r \\ \dot{\eta}_r \end{Bmatrix} \quad (3.4)$$

where η_r and $\dot{\eta}_r$ denotes r -th modal displacement and velocity, respectively. $2n \times 2n$ system matrix (A) is composed of natural frequencies (ω_r) and effective modal damping ratios (ζ_r) in the form of:

$$A = \begin{bmatrix} 0 & I \\ \Gamma_1 & \Gamma_2 \end{bmatrix} \quad (3.5)$$

where

$$\Gamma_1 = \begin{bmatrix} -\omega_1^2 & 0 & 0 & & \\ 0 & \dots & & & \\ 0 & & -\omega_r^2 & 0 & \\ & & & \dots & 0 \\ & & 0 & 0 & -\omega_n^2 \end{bmatrix} \quad (3.6)$$

$$\Gamma_2 = \begin{bmatrix} -2\zeta_1\omega_1 & 0 & 0 & & \\ 0 & \dots & & & \\ 0 & & -2\zeta_r\omega_r & 0 & \\ & & & \dots & 0 \\ & & 0 & 0 & -2\zeta_n\omega_n \end{bmatrix} \quad (3.7)$$

Input matrix (B) is calculated using normalized modal matrix (Φ) with size $n \times n$ and unit forcing matrix (U) with size $n \times$ (number of inputs):

$$B = \begin{bmatrix} 0 \\ \Gamma_3 \end{bmatrix} \quad (3.8)$$

where

$$\Gamma_3 = \Phi^T U \quad (3.9)$$

Output vector ($Y = \{w \ \dot{w} \ \ddot{w}\}^T$) consists of displacements, velocities and accelerations of the defined output DOFs, respectively. Formulation of output matrix with the size of $3 \times$ (number of outputs) $\times 2n$ is given as follows:

$$C = \begin{bmatrix} \Gamma_4 & 0 \\ 0 & \Gamma_4 \\ \Gamma_4\Gamma_1 & \Gamma_4\Gamma_2 \end{bmatrix} \quad (3.10)$$

where

$$\Gamma_4 = Y \Phi \quad (3.11)$$

and Y denotes unit displacement matrix with size $n \times$ (number of outputs). Direct feed-through matrix (D) with the size of $3 \times$ (number of outputs) \times (number of inputs) is defined by:

$$D = \begin{bmatrix} 0 \\ 0 \\ \Gamma_4 \Gamma_3 \end{bmatrix} \quad (3.12)$$

In order to improve the dynamic response at higher frequencies, residual vector method [81] is used in model order reduction phase. An additional high frequency mode coming with this method improves the transient characteristics of the reduced order model.

Forced and free vibration characteristics are investigated in this chapter. Hence, input and outputs of the plant are chosen accordingly. Electric potentials on piezoelectric patches are defined as inputs for the system. Axial strain read from the strain gage placed beneath the piezoelectric patch #1 and transverse deflection of the tip of the beam are selected as outputs. Hence, the plant is represented by 2 inputs and 2 outputs (Figure 3-5). Resulting 4 transfer functions are numerated as:

$G_{11}(s)$: Strain output for unit control (piezoelectric patch#1) voltage input [1/V]

$G_{21}(s)$: Tip deflection for unit control (piezoelectric patch#1) voltage input [mm/V]

$G_{12}(s)$: Strain output for unit disturbance (piezoelectric patch#2) voltage input [1/V]

$G_{22}(s)$: Tip deflection for unit disturbance (piezoelectric patch#2) voltage input [mm/V]

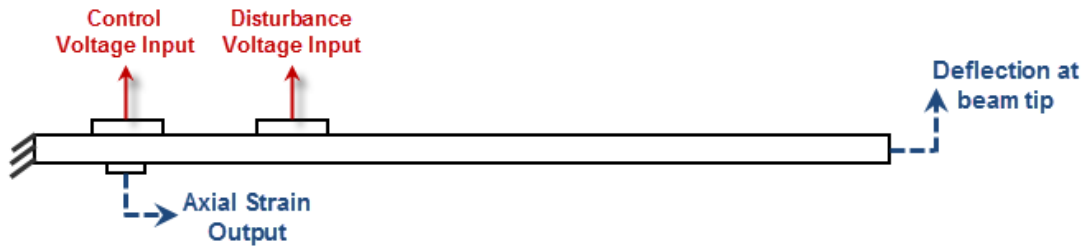


Figure 3-5 Defined input (red) and outputs (blue) of the plant

After the definition of the inputs and outputs, minimum order of the reduced model should be determined. For this reason, frequency and the transient response characteristics of the reduced order model should be compared with the ones of the full order method.

Aforementioned frequency response comparisons (Figure 3-6 to Figure 3-9) have been made for 0-200 Hz frequency band which includes the first three bending modes. Full order frequency response is obtained for this band by harmonic analyses with a resolution of 0.1 Hz. It has been shown that contributions of the first 4 modes (without residual vectors) are sufficient to capture frequency response characteristics up to 200 Hz.

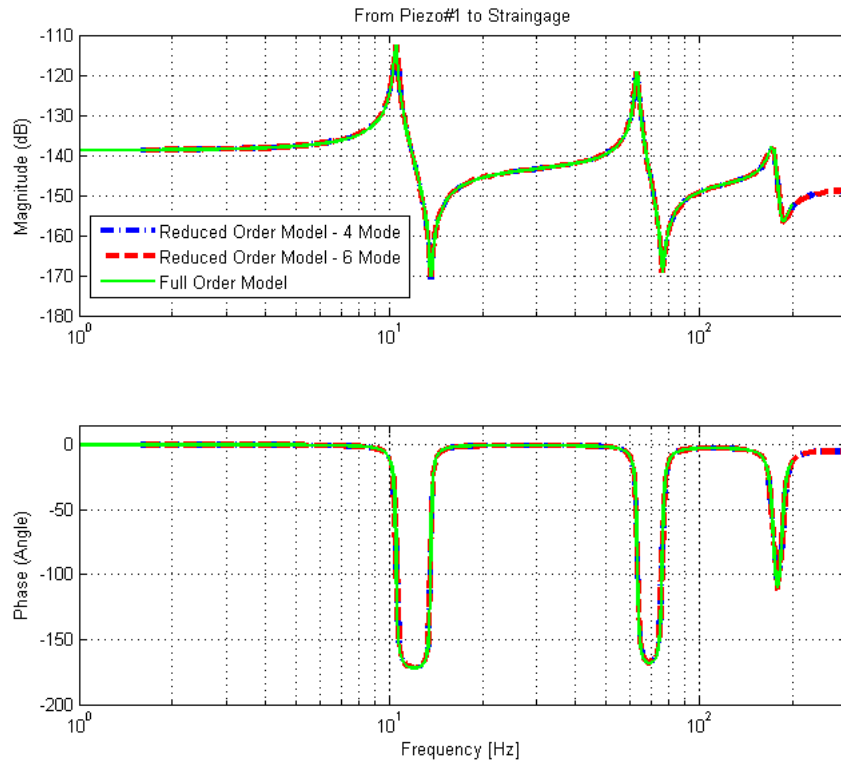


Figure 3-6 Frequency response of reduced and full order $G_{11}(s)$

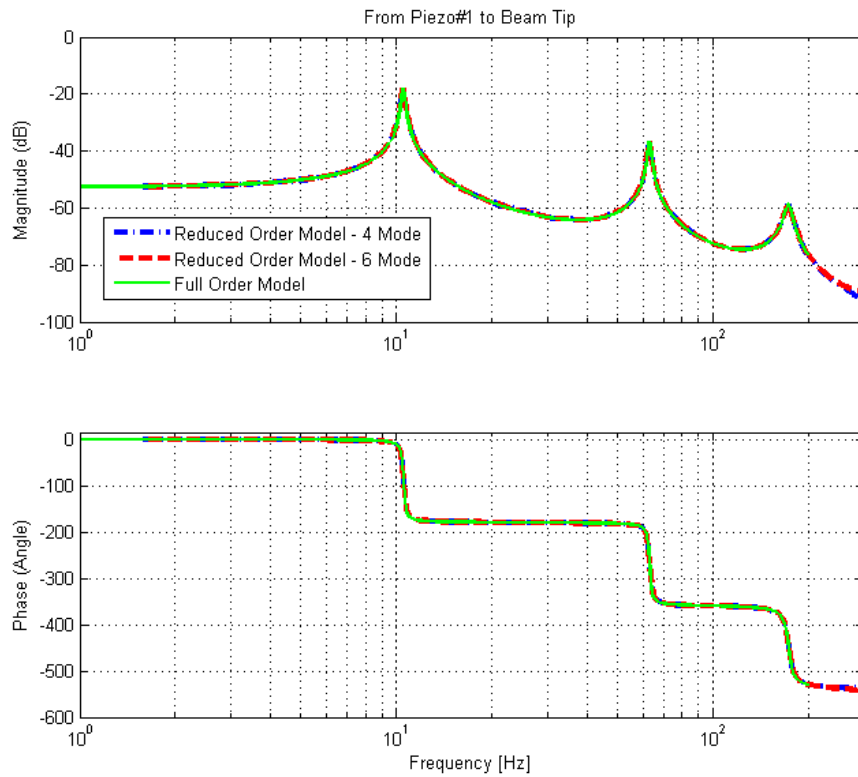


Figure 3-7 Frequency response of reduced and full order $G_{21}(s)$

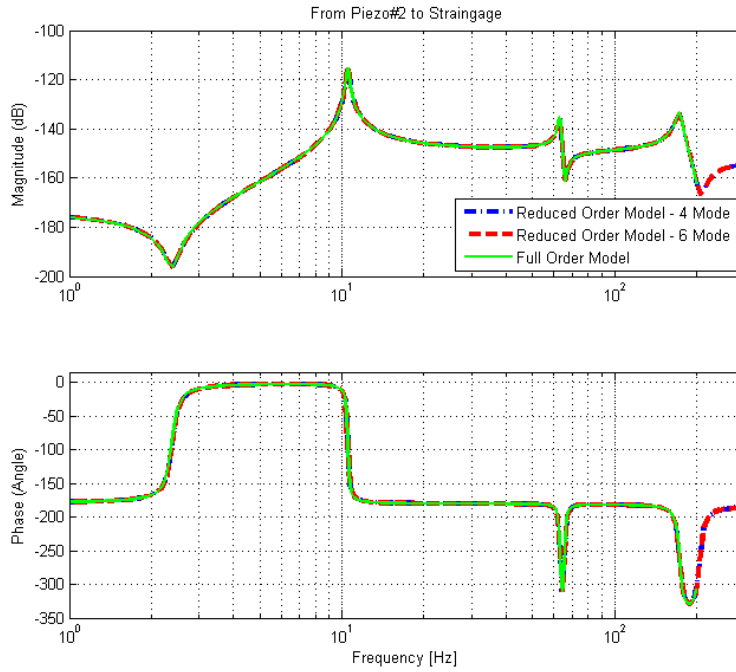


Figure 3-8 Frequency response of reduced and full order $G_{12}(s)$

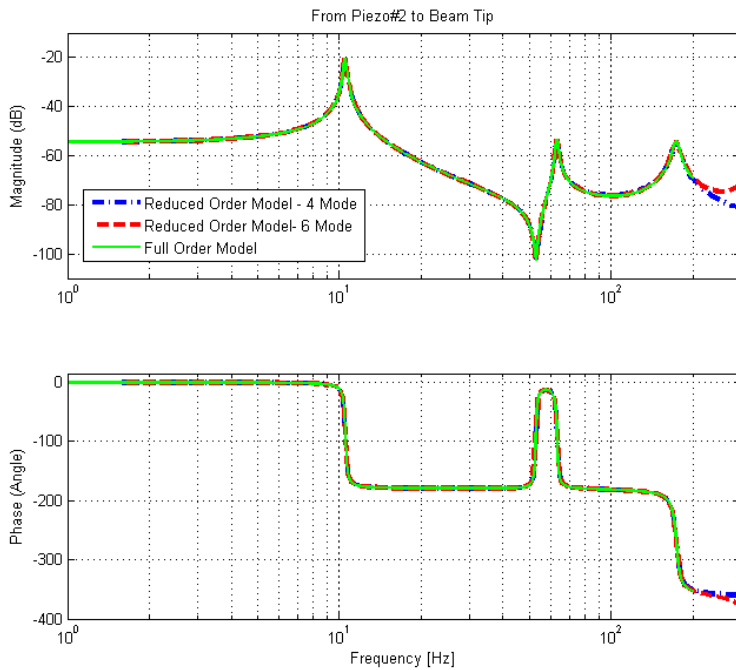
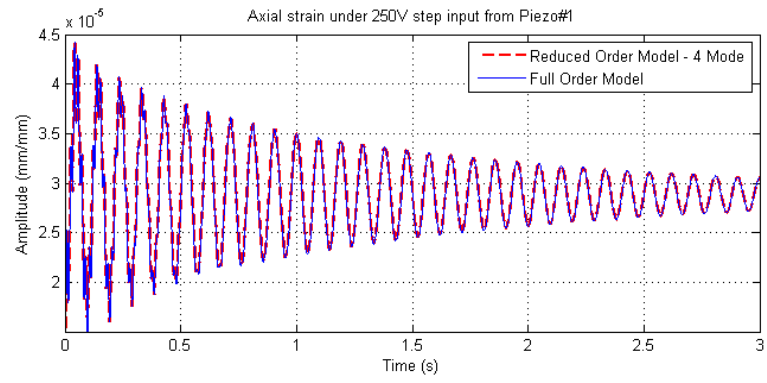
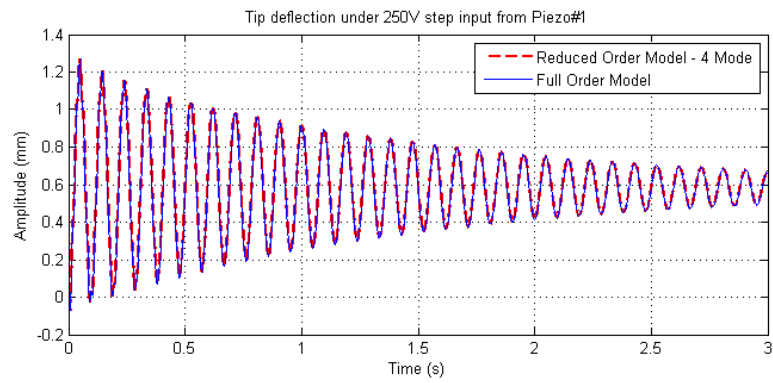


Figure 3-9 Frequency response of reduced and full order $G_{22}(s)$

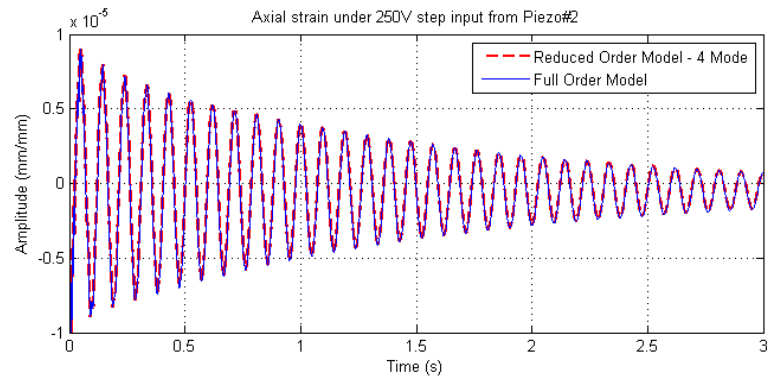
In Figure 3-10, transient responses of reduced order model are also compared with those of full order model. To this end, step responses of 250V control and disturbance input voltage are calculated for both reduced and full order models with a fixed time step of 1 ms. Continuous-time reduced order state-space models are converted to discrete-time equivalents with the help of Tustin (bilinear) transformation. It should be noted that transient behaviors of reduced order discrete-time models are well-matched with the ones of full order model.



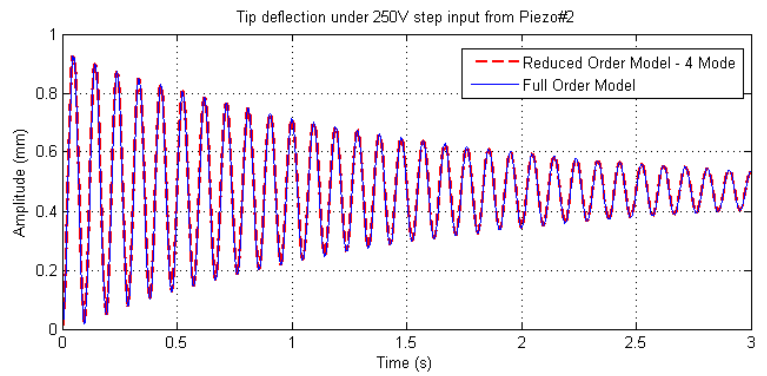
(a)



(b)



(c)



(d)

Figure 3-10 Step response of reduced and full order (a) $G_{11}(s)$ (b) $G_{21}(s)$ (c) $G_{12}(s)$ (d) $G_{22}(s)$

Since it is shown that both frequency and transient responses of the reduced order models are consistent with the ones of the full order model, these models can be used to describe dynamic behavior of the plant for controller simulations.

3.4 Controller Design

In this section, forced and free response performances of three collocated modal control techniques, namely Positive Position Feedback (PPF), Resonant Control (RC) and Integral Resonant Control (IRC), are examined on the reduced order model. Furthermore, a novel modification on Positive Position Feedback method is suggested which is named as Positive Position Feedback with Feed-through (PPFFT). Detailed theoretical backgrounds of these controllers are already given in Chapter 2. Only practical outcomes of them are mentioned in this chapter.

3.4.1 Methodology

Piezoelectric patch#1 and strain gage bonded beneath it (see Figure 3-2) are the actuator and sensor of the control action. Steady-state and transient disturbances are generated with Piezoelectric patch#2. The control scheme used in this chapter is summarized in the block diagram given in Figure 3-11.

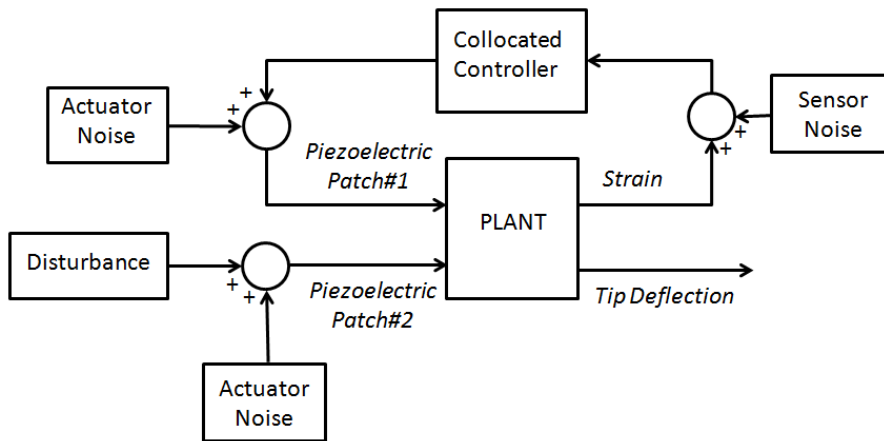


Figure 3-11 Control Scheme

In order to obtain the power spectrum of the noise to be modeled, signals of unloaded piezoelectric amplifiers and strain gages are measured. Time histories and resulting power spectral densities (PSD) of these signals are given in Figure 3-12 to Figure 3-15. Resulting PSD estimates shows that piezoelectric amplifier and strain gage noises can be modeled as white noise with -40 and -150 dB power, respectively. Hence, actuator and sensor noise are included into control scheme by 'Band-Limited White Noise' block of Simulink using mentioned power parameters.

Operating voltage range (-100/+400V) of the piezoelectric patches (PI DuraAct P-876.A12) is considered in simulations. To be in the safe side, control voltages are saturated out of the region of -50/+350V.

Forced response performance is evaluated with a logarithmic chirp disturbance between 1 and 200 Hz. One-sided amplitude of the chirp signal is 150V and duration is 600 seconds. It is not allowed any control voltage to exceed -50/+350V magnitude limit in order to ensure linearity.

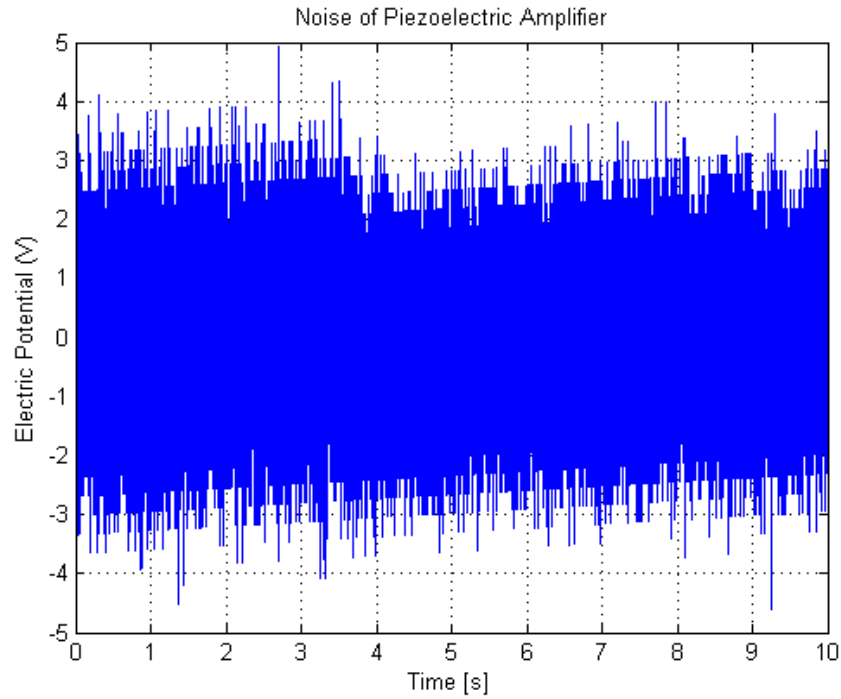


Figure 3-12 Sample time history of piezoelectric amplifier noise

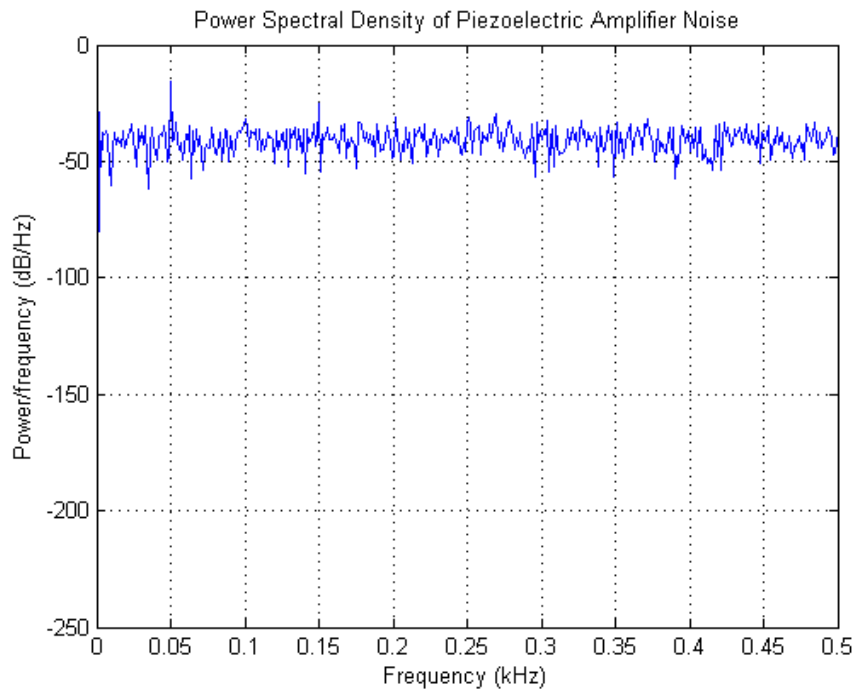


Figure 3-13 Power spectral density of piezoelectric amplifier noise

In order to achieve repeatability in transient performance measurements, a special disturbance is used. First, structure is excited in its first natural frequency for a period of 10 seconds under no control action. After 10 seconds, controller is turned on and elapsed time for the output to fall into noise level is measured. 1% settling time criterion is adopted in transient performance evaluation of both strain and tip displacement responses.

MATLAB/Simulink R2010b is used in control simulations. Fixed-step size of the solver is 0.0001 seconds. View of a sample Simulink model is given in Figure 3-16.

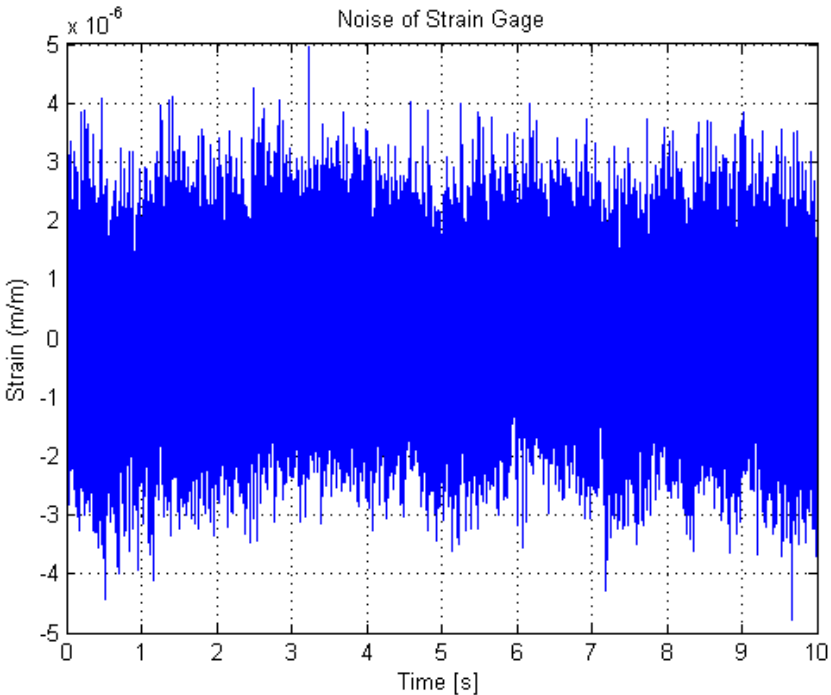


Figure 3-14 Sample time history of strain gage noise

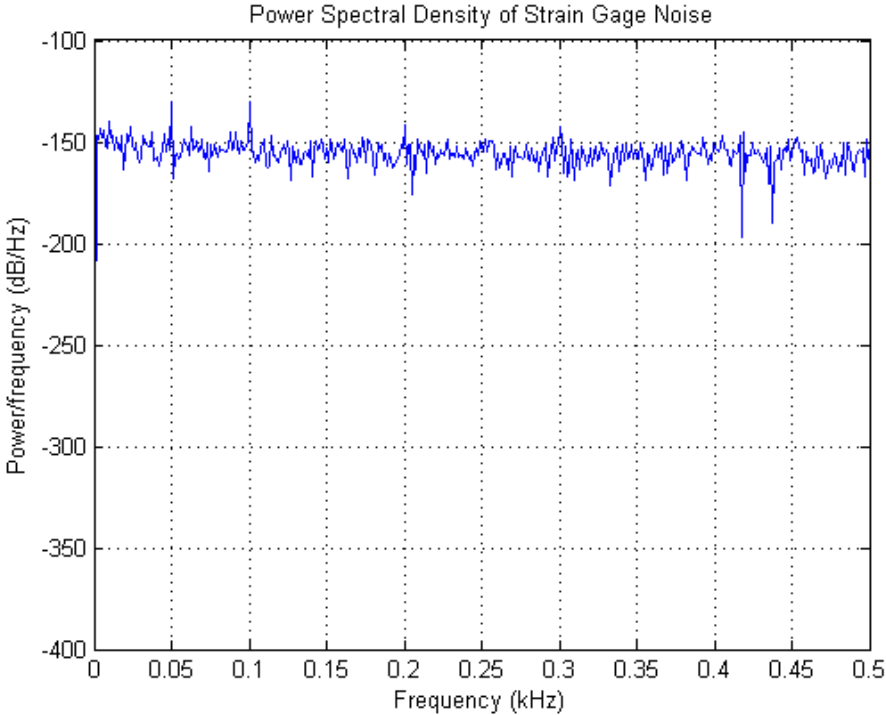


Figure 3-15 Power spectral density of strain gage noise

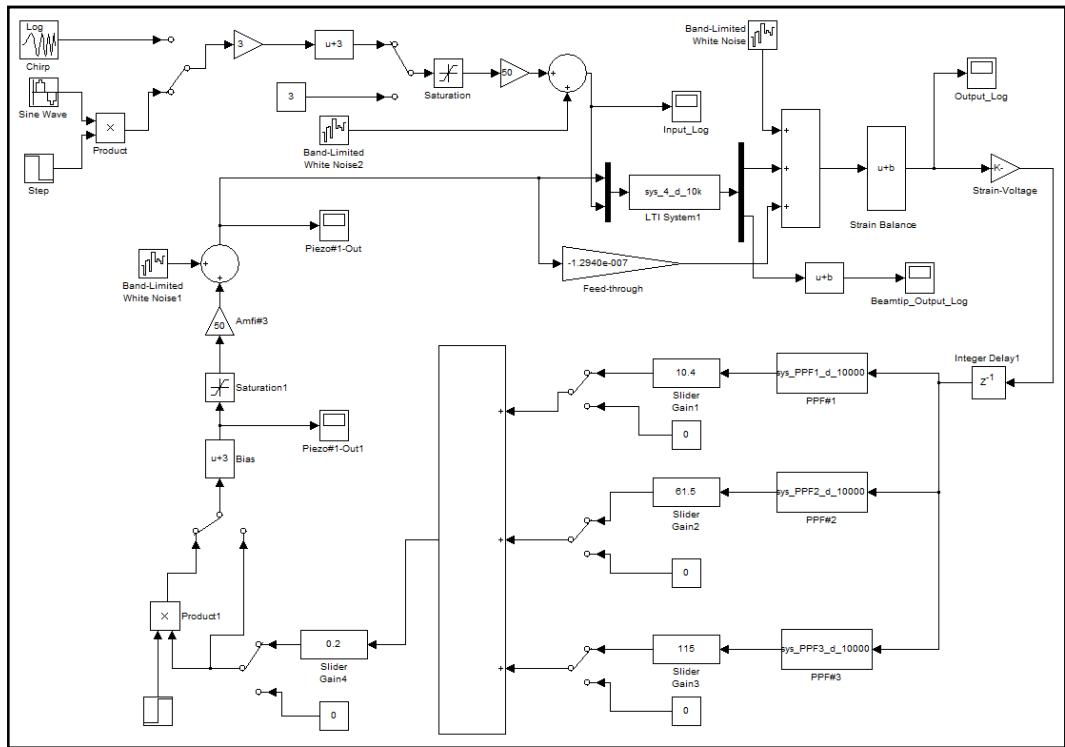


Figure 3-16 View of a sample Simulink model

3.4.2 Positive Position Feedback (PPF)

Positive position feedback is one of the most pronounced modal control techniques in the literature. Each PPF controller targets a specific mode and increases damping of the relevant mode. Several vibration modes can be suppressed by connecting multiple PPF controllers in parallel. Control scheme used in PPF simulations is presented in Figure 3-17.

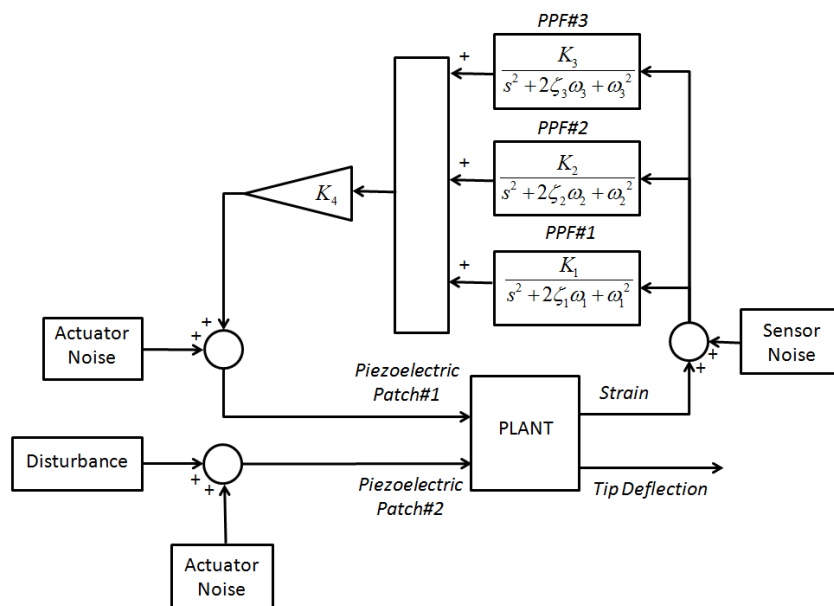


Figure 3-17 Three mode PPF Control Scheme

Each PPF controller has three parameters which are frequency (ω), damping ratio (ζ) and gain (K). Frequency of each PPF controller should be set to the natural frequency of the mode to be suppressed. For the plant discussed these frequencies are circular frequency equivalents of 10.5, 63.0 and 173.3Hz.

Since PPF controllers targeting higher modes affect the response on lower frequencies, it is not possible to tune separate PPF controllers and simply connect with the others. This situation necessitates cumbersome iterations to determine gain and damping parameters of each PPF controller. After numerous iterations 3 mode PPF controller with the parameters given in Table 3-3 is synthesized. Forced and free response performances of this controller are given in Figure 3-18 to Figure 3-21.

Table 3-3 Three mode PPF parameters

| PPF#1 | | PPF#2 | | PPF#3 | | Overall Gain |
|-------|---------------|-------|---------------|-------|---------------|--------------|
| Gain | Damping Ratio | Gain | Damping Ratio | Gain | Damping Ratio | |
| 0.65 | 0.3 | 21 | 0.3 | 155 | 0.2 | 0.35E9 |

Synthesized PPF controller reduces the forced strain response up to 23.2, 8.3 and 4.7 dB for the first three modes, respectively. Reductions in the tip displacement are similar, 26.6, 9.6 and 4.2 dB for the same modes. However, the controller causes the amplification of quasi-static strain response up to 17 dB. This is the documented drawback of PPF method, resulting saturation of the actuator for small gains and limiting the performance of the controller. Since damping of the first mode is significantly increased, PPF controller reduces the settling time of both strain and tip displacement from 7.43 seconds to 0.81 seconds.

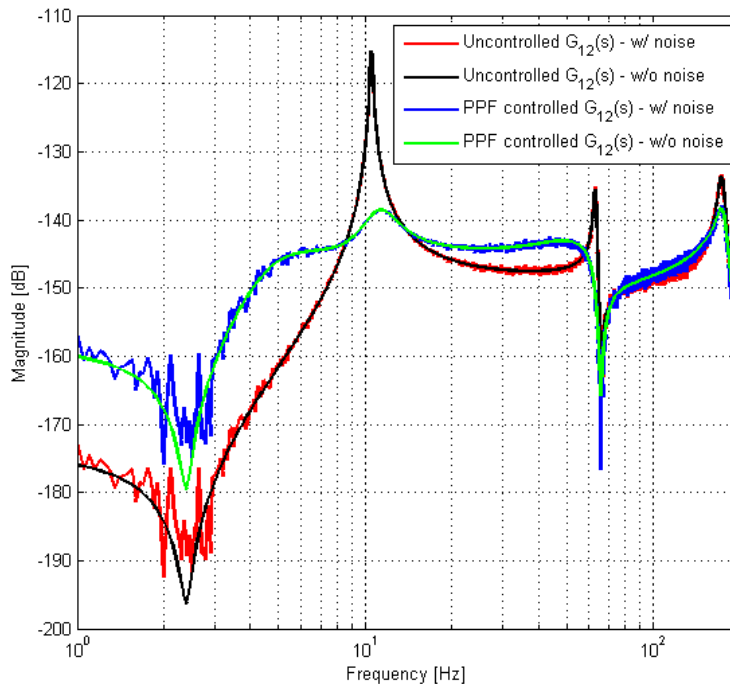


Figure 3-18 Effect of 3 mode PPF controller on $G_{12}(s)$

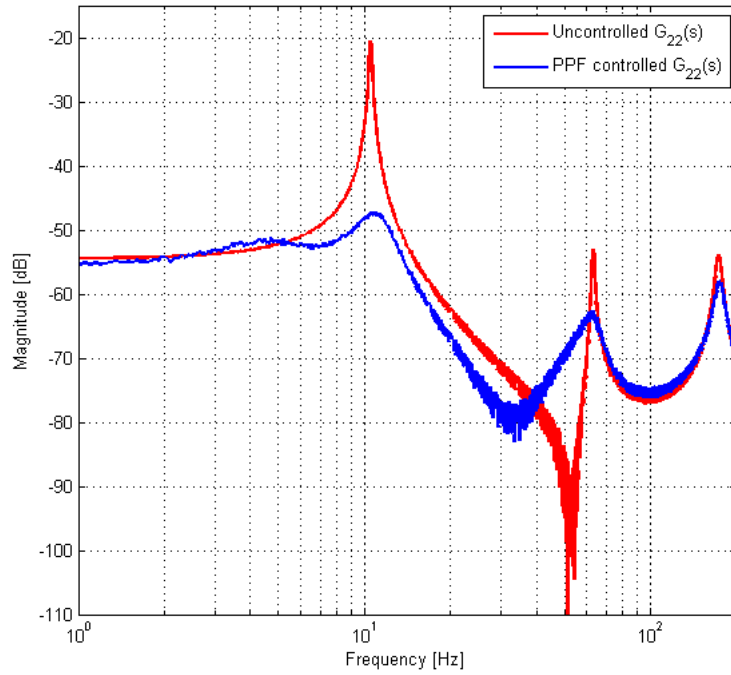


Figure 3-19 Effect of 3 mode PPF controller on $G_{22}(s)$

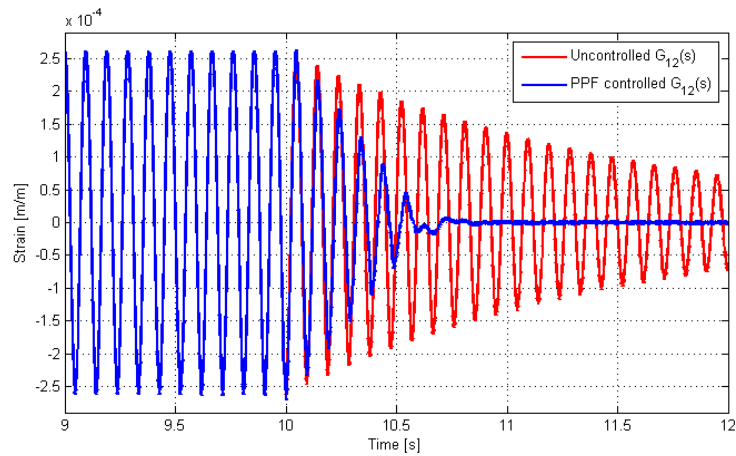


Figure 3-20 Effect of 3 mode PPF controller on transient strain response

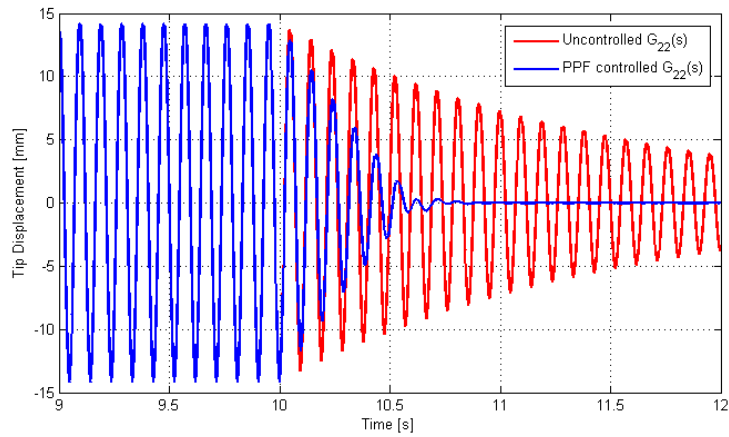


Figure 3-21 Effect of 3 mode PPF controller on transient tip displacement response

In Figure 3-18, both continuous and discrete-time simulation results are shown. Strain gage and amplifier noise models used in discrete time simulations make the quasi-static frequency response very noisy. The main reason of this situation is the low signal-to-noise-ratio. The reader should keep this phenomenon in mind while interpreting following frequency response functions.

3.4.3 Resonant Controller (RC)

Resonant control method relies on negative feedback of position signals. Like PPF method, each resonant controller (RC) targets a specific mode and multiple RCs can be connected in parallel for multi-mode control. Scheme of 3 mode RC control is given in Figure 3-22.

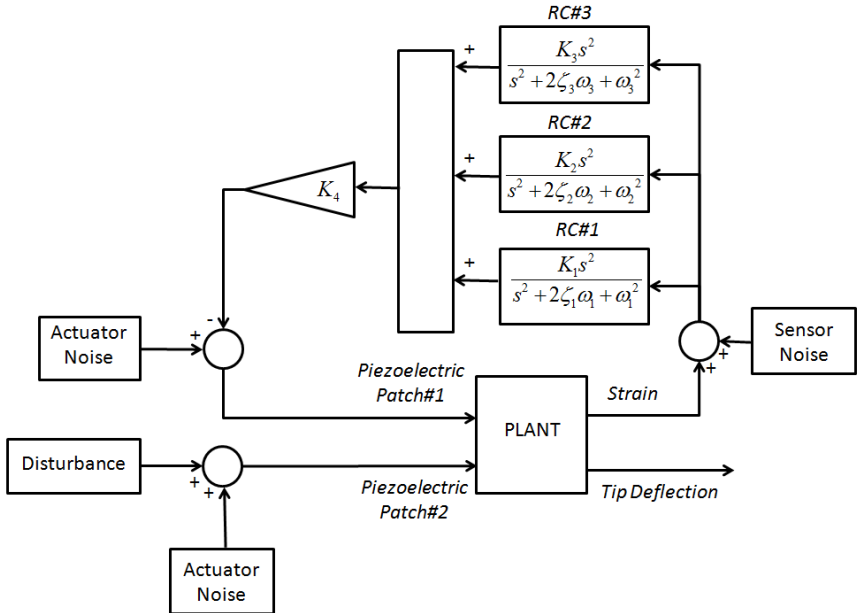


Figure 3-22 3 mode Resonant Control Scheme

Similar to PPF case, each RC has 3 parameters which are frequency (ω), damping ratio (ζ) and gain (K). First, 3 RC frequencies are selected as the natural frequencies of the first three bending modes. Then it is tried to find three sets of damping ratio and gain parameters maximizing the damping performance. Resulting parameters are given in Table 3-4.

Table 3-4 Three mode RC parameters

| RC#1 | | RC#2 | | RC#3 | | Overall Gain |
|--------|---------------|------|---------------|------|---------------|--------------|
| Gain | Damping Ratio | Gain | Damping Ratio | Gain | Damping Ratio | |
| 2.5e-4 | 0.4 | 1E-4 | 0.3 | 2E-5 | 0.15 | 0.45E9 |

Forced and free response performances of this controller are given in Figure 3-23 to Figure 3-26.

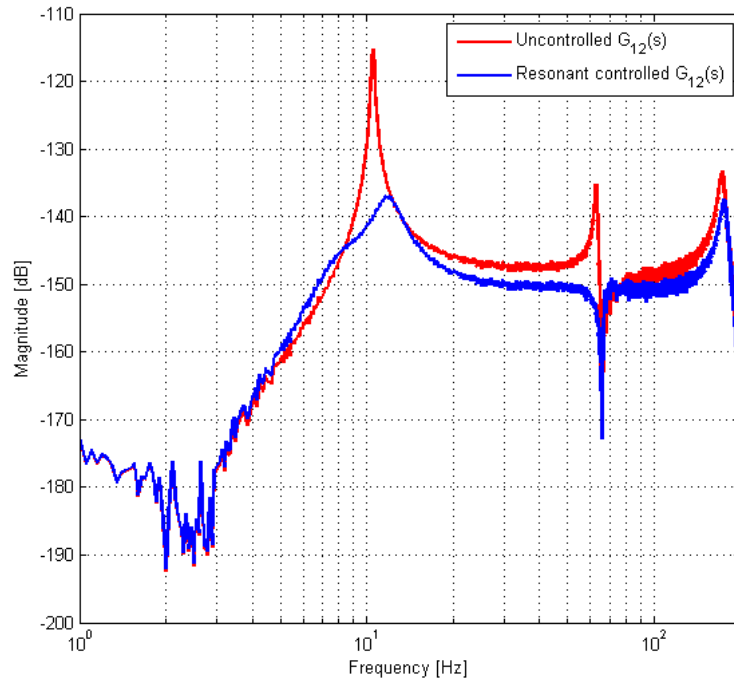


Figure 3-23 Effect of 3 mode resonant controller on $G_{12}(s)$

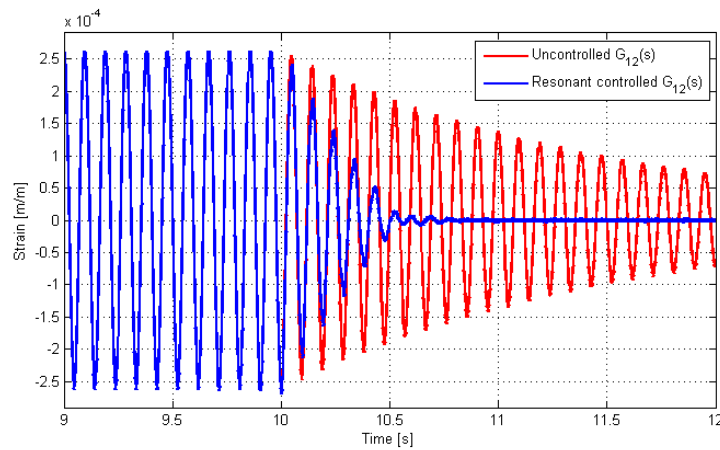


Figure 3-24 Effect of 3 mode RC on transient strain response

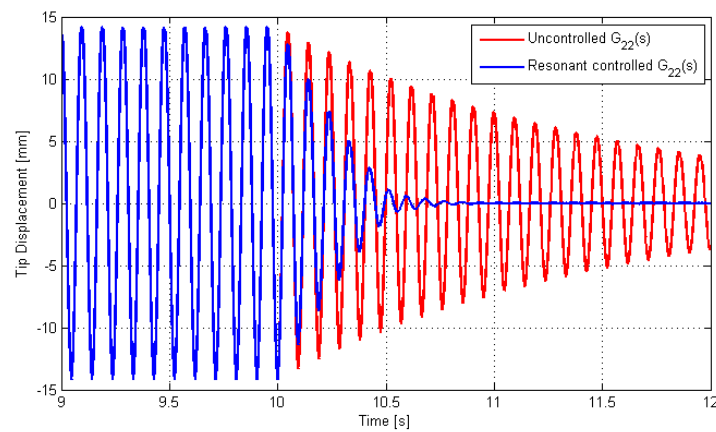


Figure 3-25 Effect of 3 mode RC on transient tip displacement response

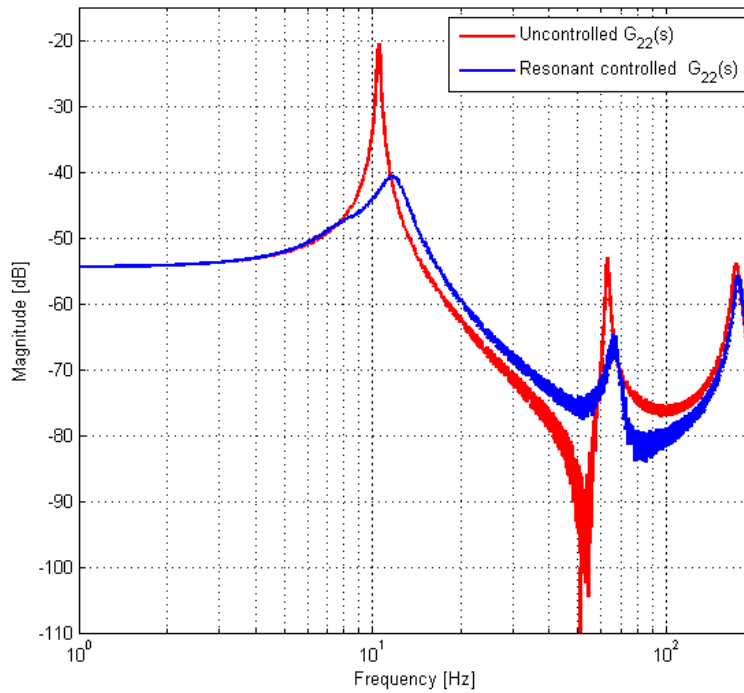


Figure 3-26 Effect of 3 mode resonant controller on $G_{22}(s)$

Strain responses in resonance regions are mitigated by 21.8, 14.9 and 4.2 dB with three mode resonant controller. Likewise, reductions in tip displacement are about 20.1, 11.5 and 1.8 dB. High-pass nature of the RC controller limits its performance especially in the first resonance, since increase in the gain of the first controller (RC#1) amplifies the control effort for higher modes which makes actuator saturated. Another consequence of this nature is the magnification of noise which threatens stability of the controller. When free response of the controller is observed, it is seen that the controller can successfully damp the transient vibrations approximately in 0.78 seconds.

3.4.4 Integral Resonant Controller (IRC)

Integral resonant control method has been developed for a different collocated system configuration. Since original version is based on displacement actuators and force sensors, open-loop transfer functions show a zero-pole interlacing property. In other words, collocated transfer function starts with an anti-resonance.

With the addition of a negative feed-through term to the collocated transfer function, a zero (anti-resonance) can be placed before the first resonance. Magnitude of the feed-through term becomes as the real part of original frequency response function at desired anti-resonance frequency.

It has been seen that placing a zero at 4 Hz yields a satisfactory performance improvement on IRC. Magnitude of the feed-through term is determined as $K_{FT} = -G_{11}(2 \cdot \pi \cdot 4j) = -1.2351 \cdot 10^{-7}$. Comparison of the original and feed-through added $G_{11}(s)$ are shown in Figure 3-27.

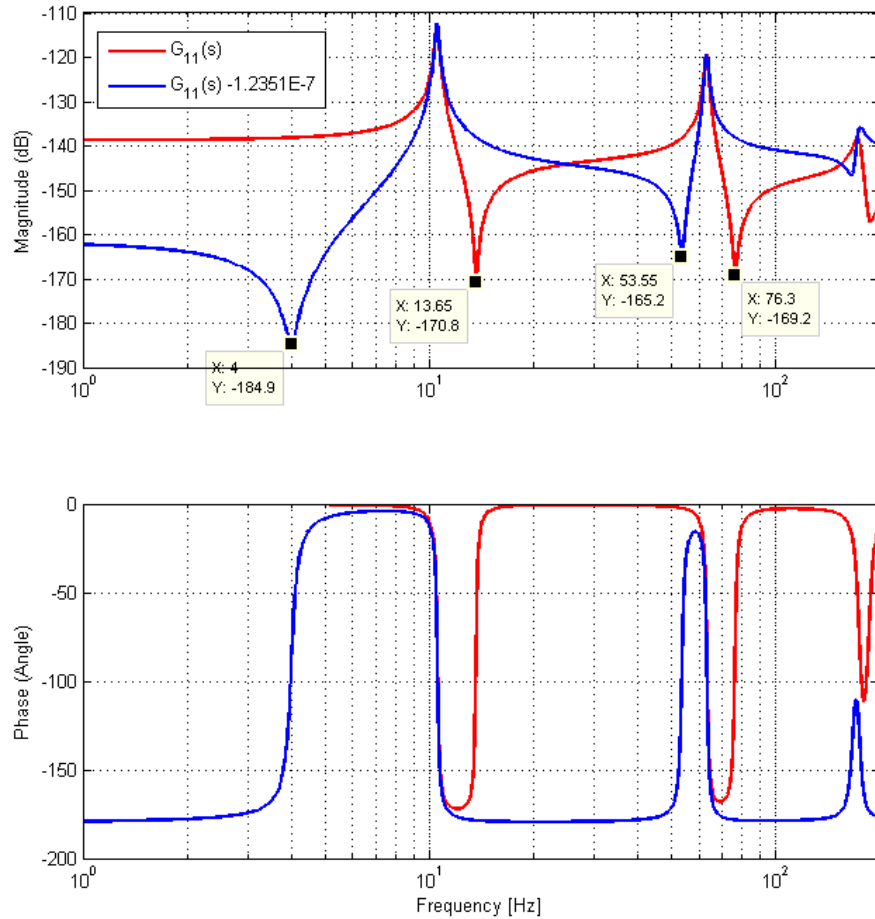


Figure 3-27 Effect of feed-through on collocated frequency response

When the Bode plot given in Figure 3-27 is investigated, it can be seen that feed-through term modifies the collocated open-loop transfer function to have an anti-resonance at 4 Hz. In spite of the changes in the anti-resonance frequencies, resonance frequencies are not affected.

Since direct integral resonant control (K/s) is very susceptible to low frequencies, instead of using it, band-pass filter version ($Ks/(s^2 + 2\omega_b s + \omega_b^2)$) is adopted [55]. Hence, input of controller rolls-off at frequencies lower than ω_b with a slope of -20dB/decade. After numerous iterations it has been decided to select this frequency (ω_b) as 3.75Hz to obtain maximum improvement on the controller. IRC parameters used and resulting control scheme are given in Table 3-5 and Figure 3-28, respectively.

Table 3-5 Integral Resonant Control parameters

| K_G | K_{FT} | ω_b |
|--------|-------------------------|-------------------------|
| 0.35E8 | $-1.2351 \cdot 10^{-7}$ | $2 \cdot \pi \cdot 3.5$ |

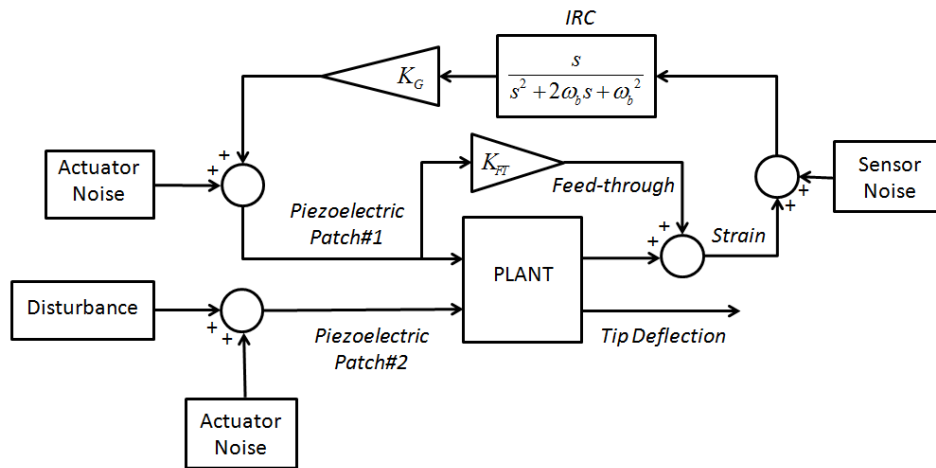


Figure 3-28 Integral Resonant Control Scheme

Disturbance rejection performances of the integral resonant control are given in Figure 3-29 and Figure 3-30. Reductions of strain response in first three resonance regions are 32.8, 10.1 and 1.5 dB. Similarly 24.1, 8.6 and 1.4 dB mitigation is obtained in tip displacement response. These results show that relocated poles (natural frequencies) of the IR controlled structure is more advantageous for sensor position, especially for the first mode. Another indication of the results is the decrease of control performance for the higher modes. This property is a consequence of -20dB/decade roll-off characteristics of the integral control.

Transient response performances of the controller are presented in Figure 3-31 and Figure 3-32. IR controller damps the transients of strain and tip displacement response approximately in 0.74 and 0.89 seconds, respectively. This considerable difference is the reflection of the difference seen in forced response performance.

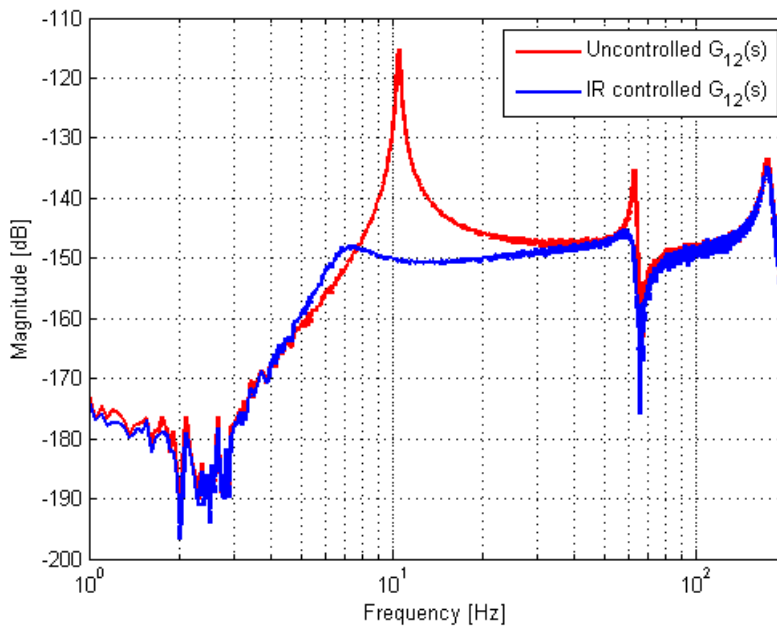


Figure 3-29 Effect integral resonant controller on $G_{12}(s)$

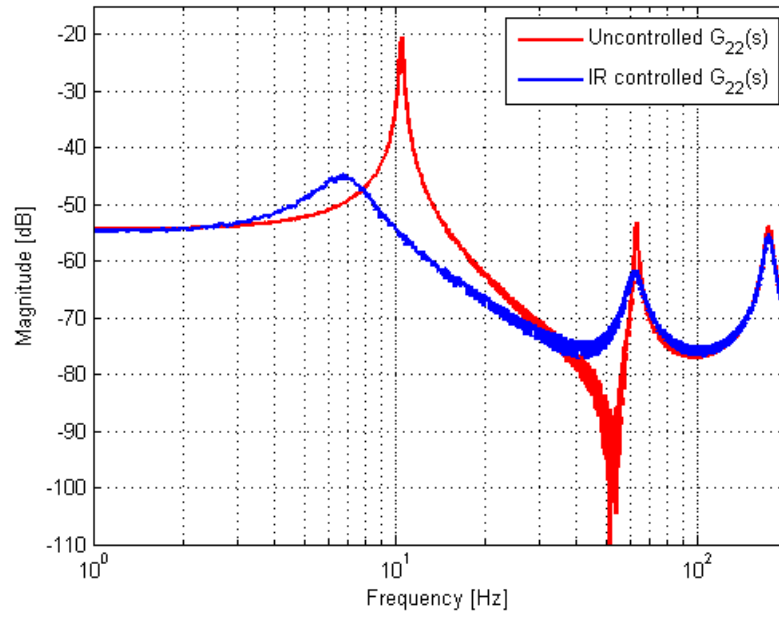


Figure 3-30 Effect integral resonant controller on $G_{22}(s)$

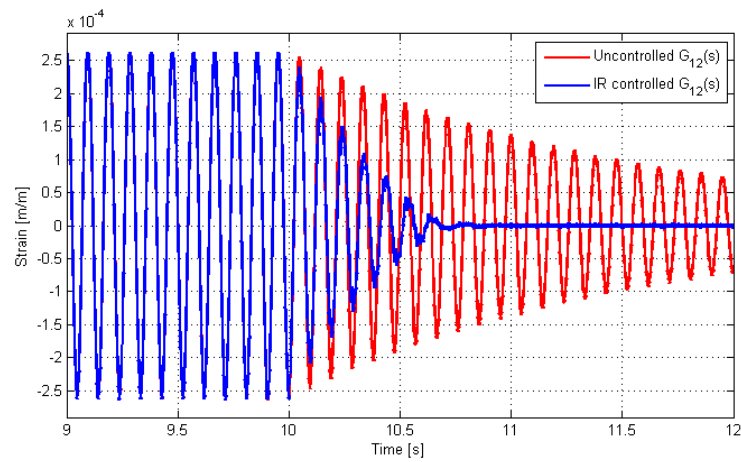


Figure 3-31 Effect of IRC on transient strain response

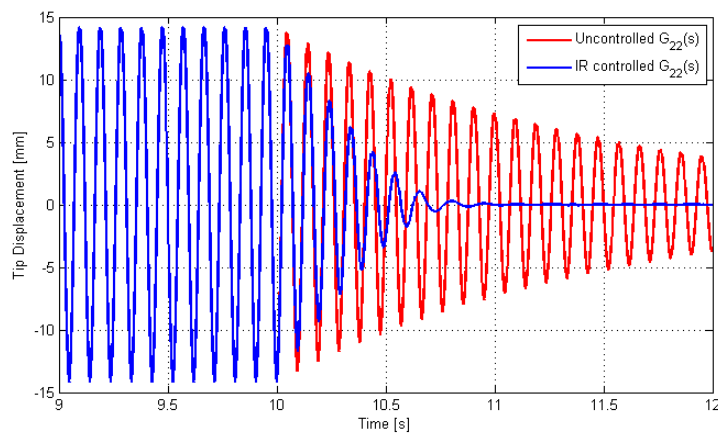


Figure 3-32 Effect of IRC on transient tip displacement response

3.4.5 Positive Position Feedback with Feed-through (PPFFT)

Beside high performance of positive position feedback, it is a simple, robust and stable method for single mode control. However, multi-mode control with PPF method necessitates troublesome tuning effort and worsens its performance in quasi-static region.

In order to improve the quasi-static performance of the PPF controller, addition of a feed-through term is suggested. This modification inhibits amplification of the response in stiffness dominated regions between resonances; contrariwise makes it possible to attenuate it. Suggested control method is named as Positive Position Feedback with Feed-through (PPFFT). Control scheme of the 3 mode PPFFT is presented in Figure 3-33.

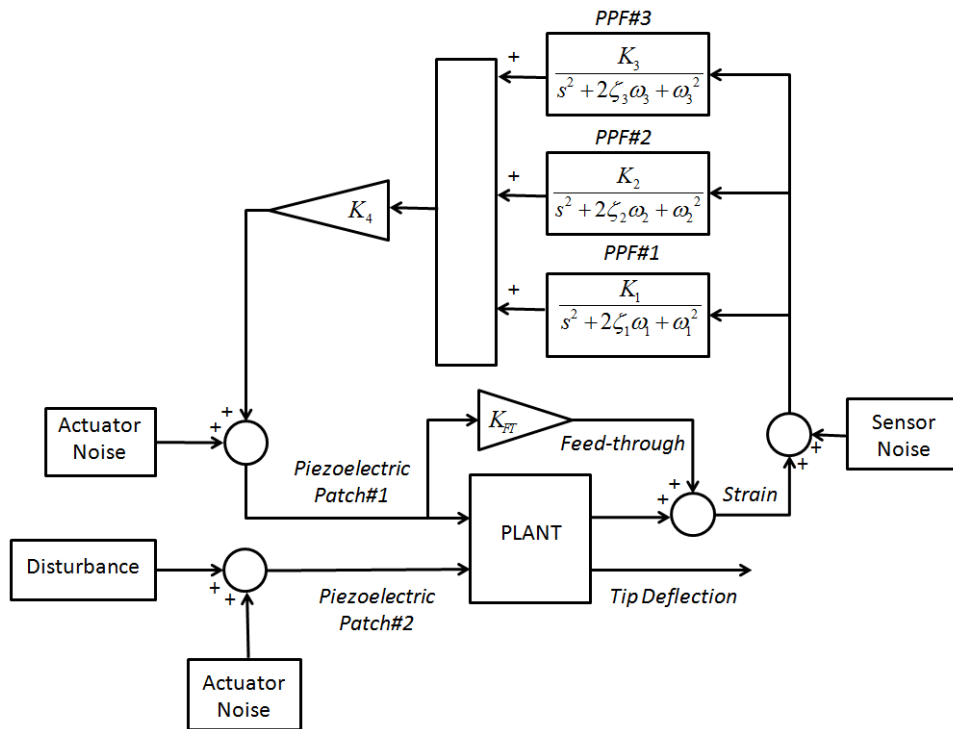


Figure 3-33 Three mode PPFFT Control Scheme

As discussed in integral resonant control section, addition of the feed-through term to the collocated system allows one to place a zero to desired frequency. It is seen that 5 Hz is a suitable choice to position a zero. Feed-through added frequency response of the collocated system ($G_{11}(s)$) is given in Figure 3-34. It can be seen that new anti-resonances of the collocated frequency response are 5, 54.3 and 165.6 Hz. It is important to notice that controller will have less impact at these frequencies.

Addition of feed-through term also changes the phase response of the collocated system. As a result of switching from pole-zero interlacing to zero-pole interlacing system, frequencies of maximum negative imaginary response change. Therefore frequencies of the PPF filters shall not be selected as the natural frequencies of the system in PPFFT configuration.

While using this method, frequency of the each PPF should be lower than the related natural frequency. Although damping and the allowable gain of each PPF affect the optimal location of the filter frequency, superior performance is observed in the neighborhood of anti-resonance frequencies.

Root-locus technique has been used for the selection of controller parameters. As it is common in modal control, aim was to maximize the damping of each mode while guaranteeing the stability of

controller. Chosen parameters of 3 mode PPFFT controller are given in Table 3-6. Resulting root-locus, pole-zero map and Bode diagram of PPFFT controller implemented $G_{11}(s)$ are given in Figure 3-35 and Figure 3-36.

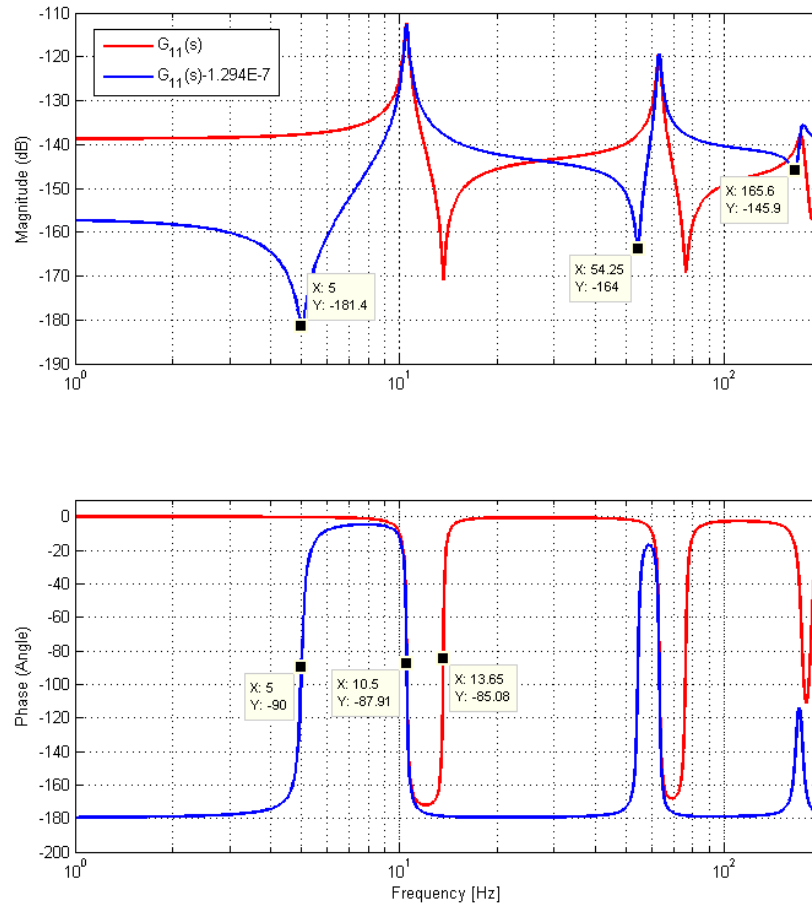


Figure 3-34 Effect of feed-through on collocated frequency response ($G_{11}(s)$)

Table 3-6 Three mode PPFFT controller parameters

| PPF#1 | | | PPF#2 | | | PPF#3 | | | Overall Gain | Feed-through |
|------------|------|---------------|------------|------|---------------|------------|------|---------------|--------------|--------------|
| Freq. [Hz] | Gain | Damping Ratio | Freq. [Hz] | Gain | Damping Ratio | Freq. [Hz] | Gain | Damping Ratio | | |
| 7 | 10.4 | 0.9 | 55 | 61.5 | 0.3 | 166 | 115 | 0.1 | 0.2E9 | -1.294E-7 |

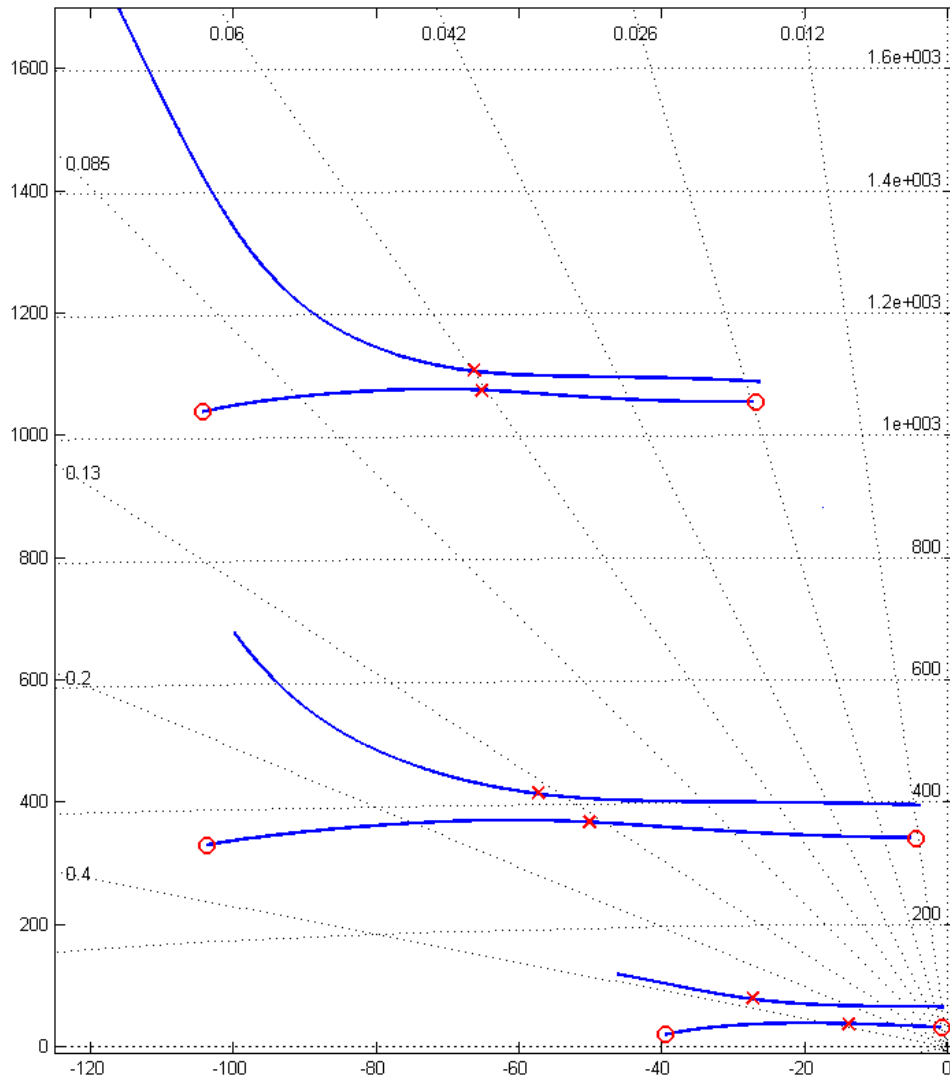


Figure 3-35 Root-locus and pole-zero map of PPFFT controlled $G_{11}(s)$

Disturbance rejection performance of the PPFFT controller is presented in Figure 3-37 and Figure 3-38. First three modal strain reductions are in the order of 30, 11.2 and 3 dB. Similarly 28.7, 10 and 4.7 dB reductions are seen for the first three resonances. Hence, it can be concluded that suggested control method is very effective in modal damping augmentation. Moreover, PPFFT controller shows superior performance in out-of-resonance frequencies compared to its predecessor, PPF controller, especially when sensor response is considered.

Transient response performance of the PPFFT controller is shown in Figure 3-39 and Figure 3-40. PPFFT controller reduces the settling time from 7.43 seconds to 0.57 seconds (*see Figure 3-41*). Hence, suggested modification improves the transient performance of PPF controller (0.81 seconds) by 30 percent.

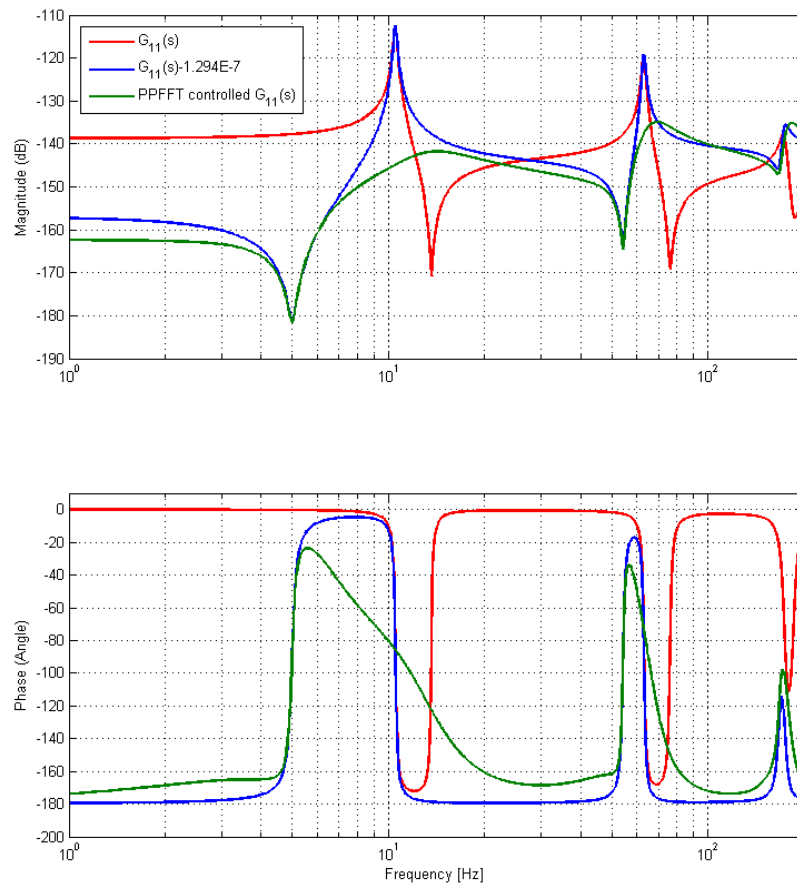


Figure 3-36 Bode diagram of PPF controlled $G_{11}(s)$

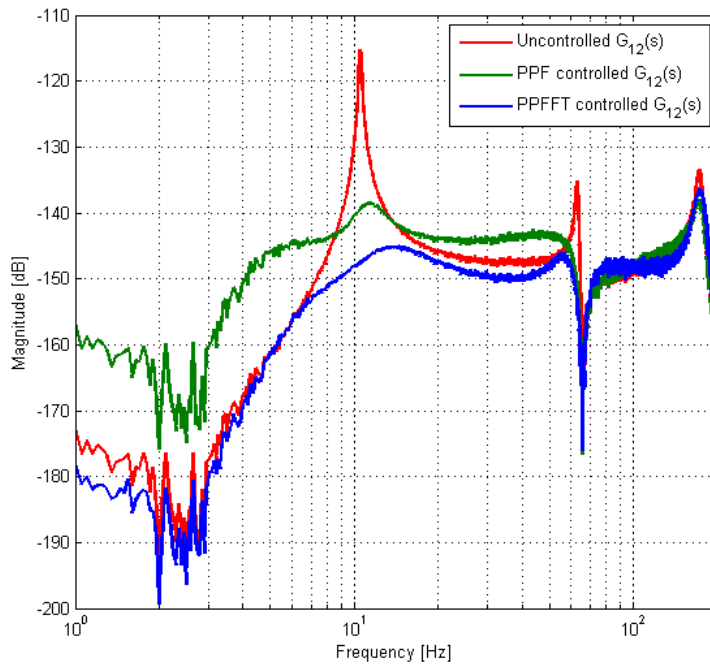


Figure 3-37 Effect of PPF controller on $G_{12}(s)$

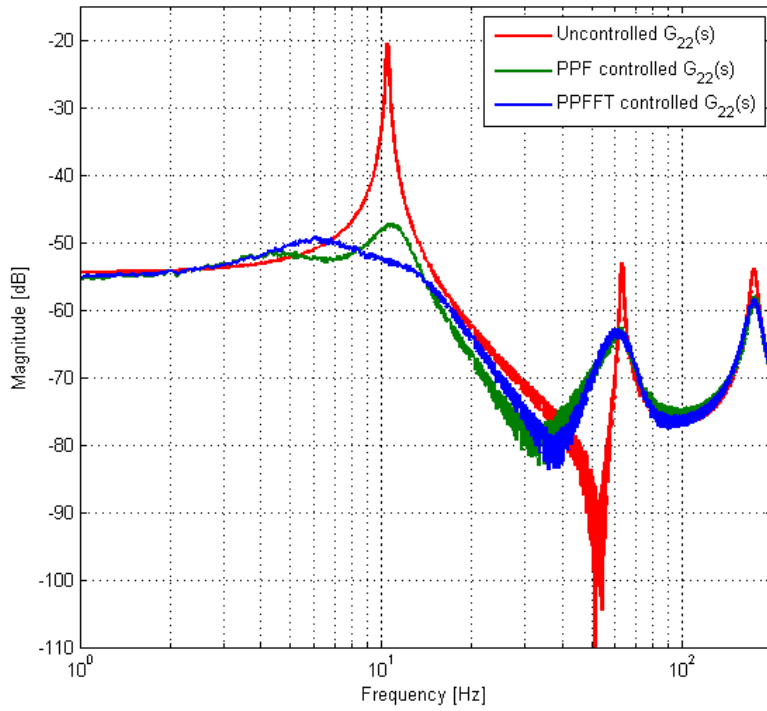


Figure 3-38 Effect of PPFFT controller on $G_{22}(s)$

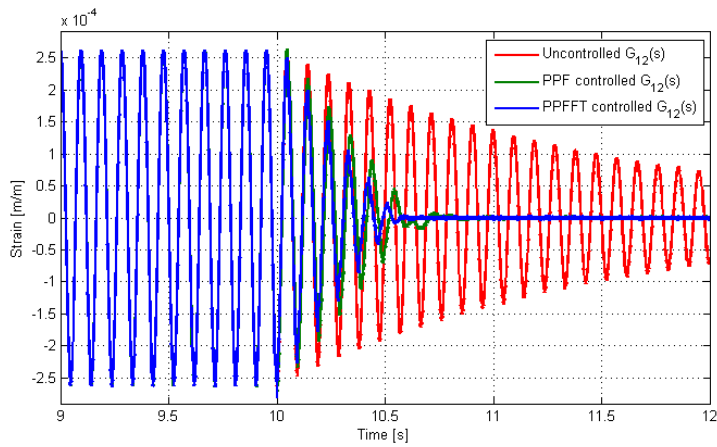


Figure 3-39 Effect of 3 mode PPF on transient strain response

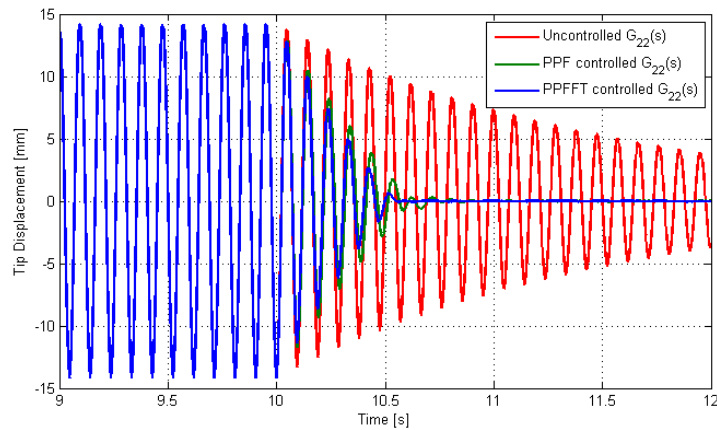


Figure 3-40 Effect of 3 mode PPFFT on transient tip displacement response

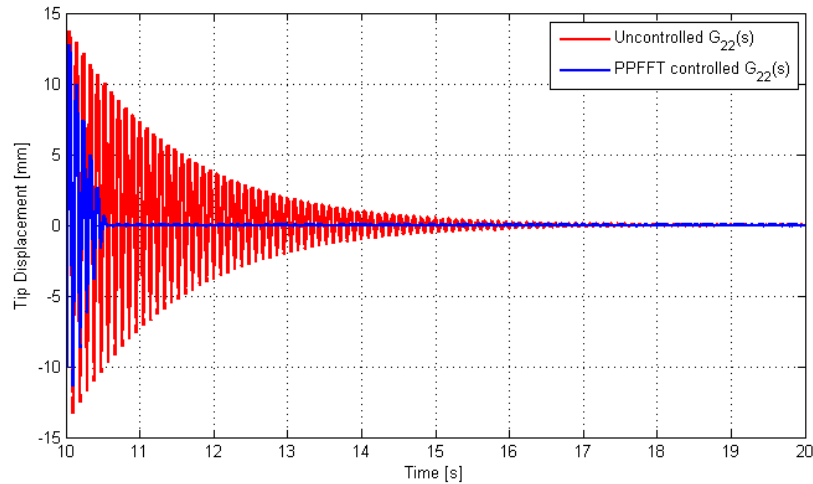


Figure 3-41 Effect of 3 mode PPFFT on transient tip displacement response-2

3.5 System Identification

Finite element analyses give a lot of information about the dynamics of the controlled structure. However, before real-time application of these controllers a more precise plant model has to be obtained. For this purpose, open-loop transfer functions of the controlled structure should be acquired.

Micro-Measurement general purpose quarter-bridge strain gages are used for strain sensing. Traveller StrainMaster multi-channel bridge amplifier is utilized for the conditioning of the strain signal. Analog input and output channels of NI PCI-6259 DAQ card are the interfaces for sensor and actuator signals. Physik Instrumente (PI) E-413.D2 piezoelectric amplifiers multiply voltage of actuation signals by 50 and send them to the PI P-876.A12 piezoelectric patches. MATLAB/Simulink R2010b Real-Time Windows Target (RTWT) is run with 10kHz sampling rate. Schematic diagram and picture of the experimental setup are given in Figure 3-42 and Figure 3-43, respectively. Piezoelectric patches and strain gages bonded to the structure are shown in Figure 3-44 and Figure 3-45, respectively.

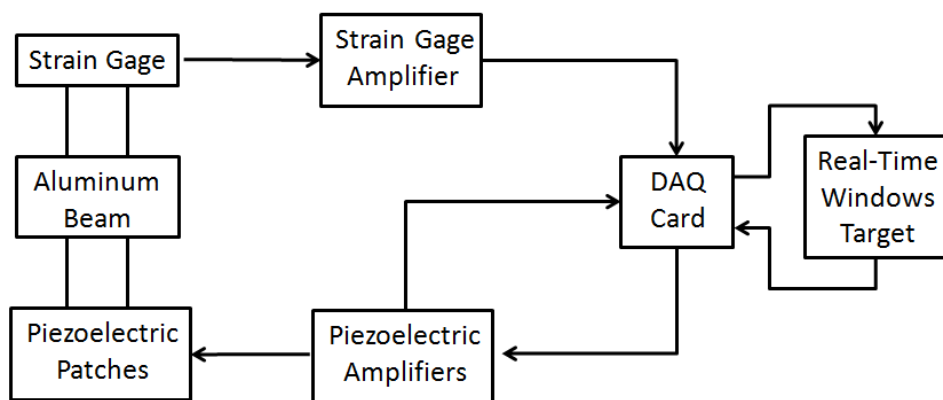


Figure 3-42 Schematic diagram of the experimental setup

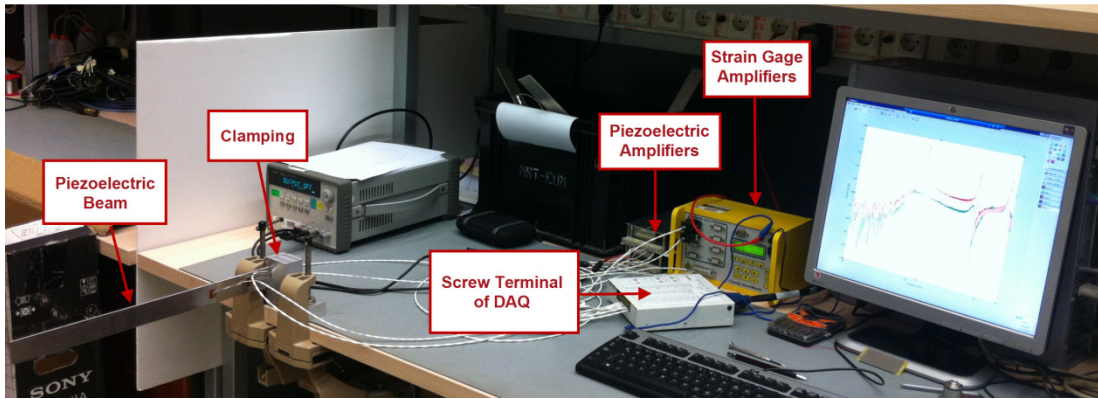


Figure 3-43 Picture of the experimental setup

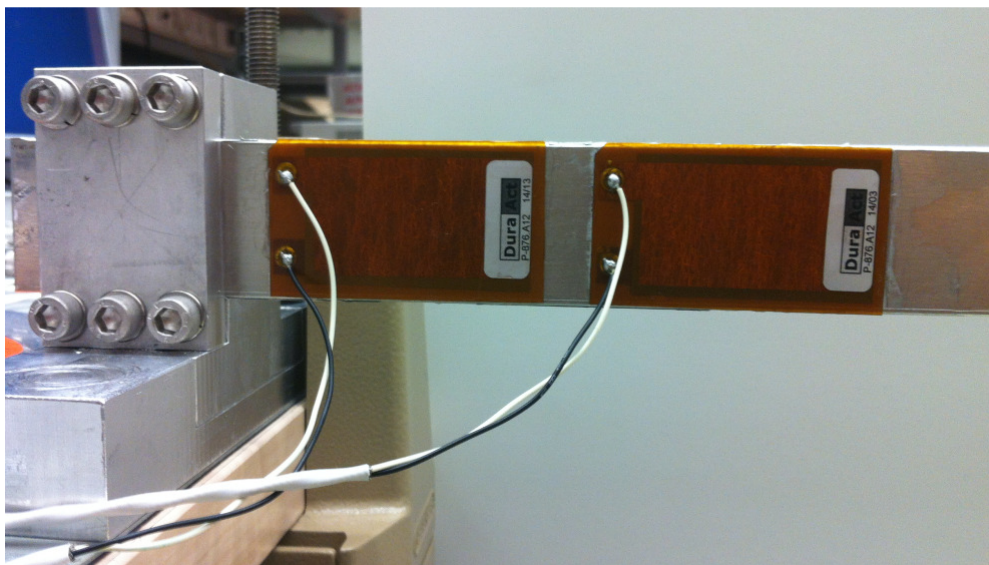


Figure 3-44 Picture of the bonded piezoelectric patches



Figure 3-45 Picture of the bonded strain gages

Excitation of the structure is done by using logarithmic chirp signal. Frequency is swept from 1 to 200 Hz for a period of 600 seconds. Piezoelectric amplifier outputs are used as input signals, and strain gage amplifier responses are used as the output signals of open-loop transfer functions. Full-point FFT method is used to obtain frequency responses for a better resolution. Since there is no laser displacement sensor in hand, tip displacement response could not be obtained. For this reason displacement output transfer functions ($G_{21}(s)$ and $G_{22}(s)$) could not be documented.

Finite element estimation on collocated open-loop transfer function $G_{11}(s)$ is compared with the experimental frequency response in Figure 3-46. First prominent difference is the offset in the quasi-static region. This offset is based on incompatibility of piezoelectric constant (e_{33}) defined in product datasheet. Test results show that real piezoelectric constant is approximately 40% higher than the catalogue value. As expected, actual modal damping ratios of the structure are also different from the assumed values in FE analyses. The discrepancy is noticeable especially for the third mode. It is obvious that third modal damping ratio should be significantly lower than the value assumed in FE analyses.

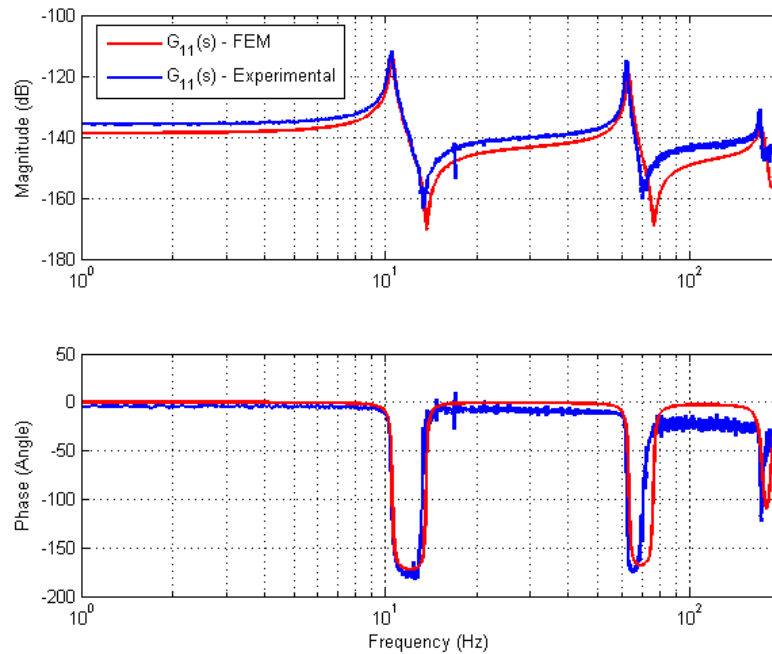


Figure 3-46 Experimental open-loop transfer function of $G_{11}(s)$ in Bode format

Experimental disturbance frequency response ($G_{12}(s)$) is compared with the one estimated by finite element analyses in Figure 3-47. Addition to the differences mentioned for $G_{11}(s)$, an anti-resonance seen in FE analyses at 2.4 Hz is very blurry in experimental frequency response and seen around 1 Hz.

After this stage of the process, study can be continued by following two different approaches. One of them is to update the finite element model until satisfactory agreement with experimental results is achieved, called '*model updating*'. Another alternative is to generate a mathematical model which will represent the dynamics of the structure by using experimental data, known as '*system identification*'. System identification approach is adopted in the scope of this study.

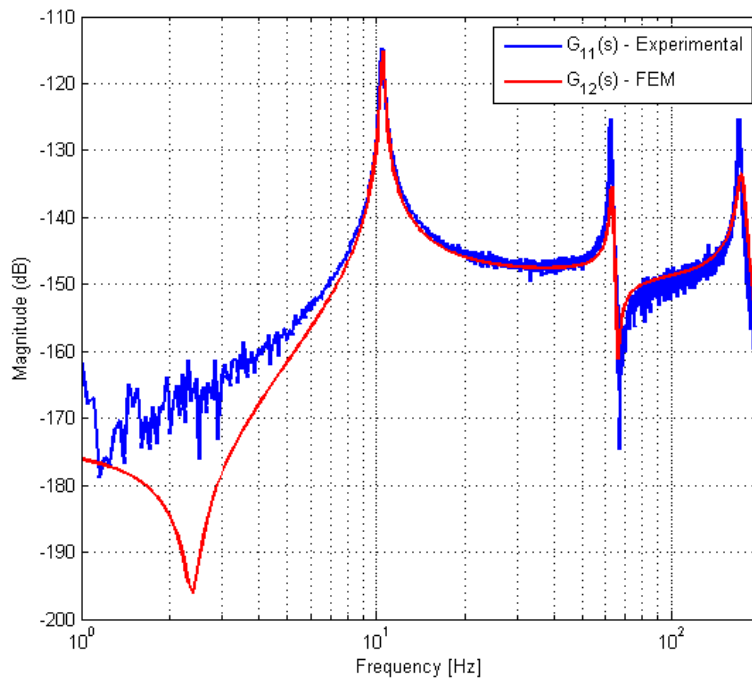


Figure 3-47 Experimental disturbance frequency response ($G_{12}(s)$)

In order to represent these transfer functions as mathematical expressions, a multiple input single output (MISO) model should be developed. In order to accomplish this, a built-in command of MATLAB Signal Processing Toolbox, 'pem', is used. The subspace Gauss-Newton direction ('gn') is the iterative parameter estimation method. Defined frequency weightings of the cost functions for $G_{11}(s)$ and $G_{12}(s)$ are given in Figure 3-48.

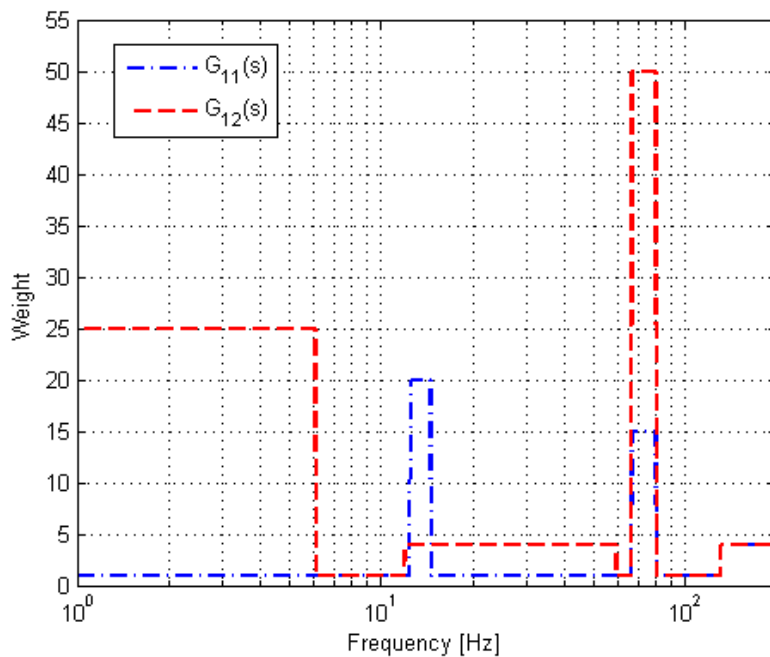


Figure 3-48 Frequency weights used in curve-fitting

Frequency responses of the synthesized 9th order system model are compared with the ones obtained experimentally. Figure 3-49 and Figure 3-50 show the success of the curve-fitting study.

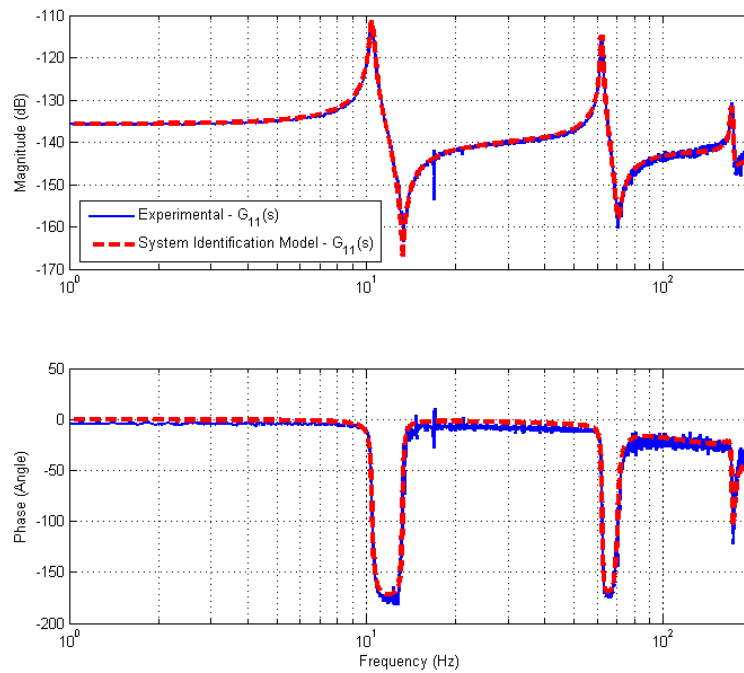


Figure 3-49 Experimental and identified $G_{11}(s)$ in Bode format

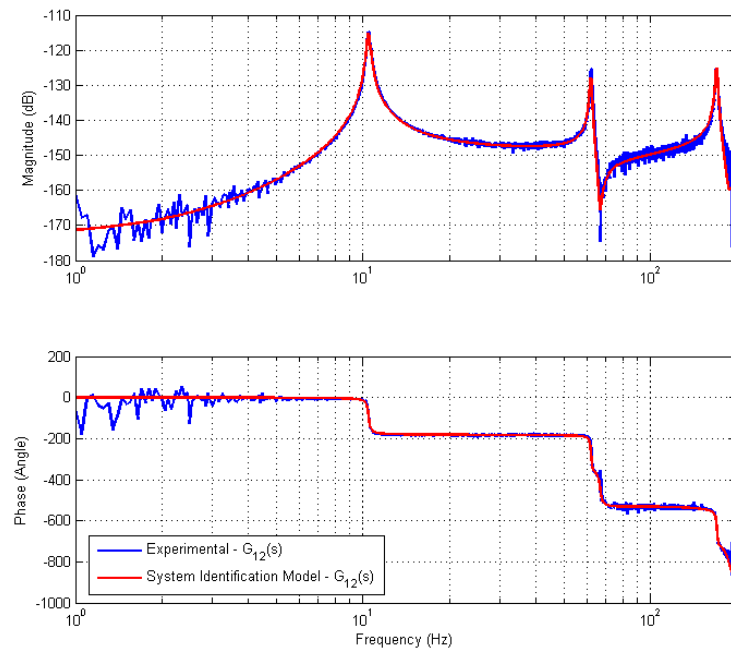


Figure 3-50 Experimental and identified $G_{12}(s)$ in Bode format

Natural frequencies and damping ratios for the first three bending modes of the identified model are given with the ones of finite element model in Table 3-7. When natural frequency deviations

(maximum 2%) between the finite element estimations and experimental frequency responses are considered, it can be said that finite element model is quite successful to capture modal characteristics of the structure. However, damping properties used in finite element model should be revised before a future dynamic analysis.

Table 3-7 Modal properties of identified model vs. finite element model

| Bending Mode | Natural Frequency [Hz] | | Deviation (%) | Damping Ratio | | Deviation (%) |
|-----------------|------------------------|----------------------------|---------------|--------------------|----------------------------|---------------|
| | From Finite Elements | From System Identification | | In Finite Elements | From System Identification | |
| 1 st | 10.51 | 10.45 | 0.55 | 0.0100 | 0.0115 | -13.04 |
| 2 nd | 63.03 | 62.05 | 1.58 | 0.0100 | 0.0064 | 56.25 |
| 3 rd | 173.30 | 170.00 | 1.94 | 0.0241 | 0.0069 | 249.28 |

3.6 Adaptation of Controllers

Even if small, a discrepancy exists between the frequency response of identified model and finite element model. Hence controller parameters (gains, center frequencies, damping ratios) should be updated with respect to the identified model before real-time control application. In this section, details of this adaptation process for different controllers are explained.

3.6.1 Positive Position Feedback (PPF)

First of all, natural frequencies of three parallel PPF controllers are updated with respect to the poles of the identified model (Table 3-7). Then, other relevant parameters (gains and filter damping ratios) are tuned. Parameters used in three mode PPF controller are given in Table 3-8.

Table 3-8 Updated 3 mode PPF parameters

| PPF#1 | | PPF#2 | | PPF#3 | | Overall Gain |
|-------|---------------|-------|---------------|-------|---------------|--------------|
| Gain | Damping Ratio | Gain | Damping Ratio | Gain | Damping Ratio | |
| 0.5 | 0.3 | 18 | 0.3 | 135 | 0.15 | 0.3E9 |

When the forced response spectrum (Figure 3-51) is investigated, it is seen that presented controller attenuates vibrations up to 20.9, 14.4, 8.3 dB for the first, second and third modes, respectively. However, the controller amplifies the vibrations up to 15 dB in out of resonance regions, especially in quasi-static region. On the other hand, controller adds substantial damping to the structure which can eliminate the transient vibrations, resulting from initial displacement and velocity fields, approximately in 0.74 seconds (Figure 3-52).

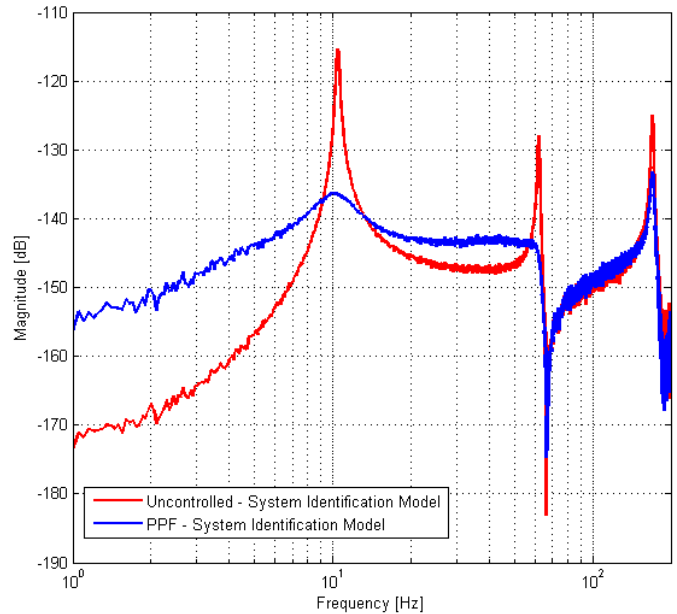


Figure 3-51 Forced response performance of updated 3 mode PPF controller

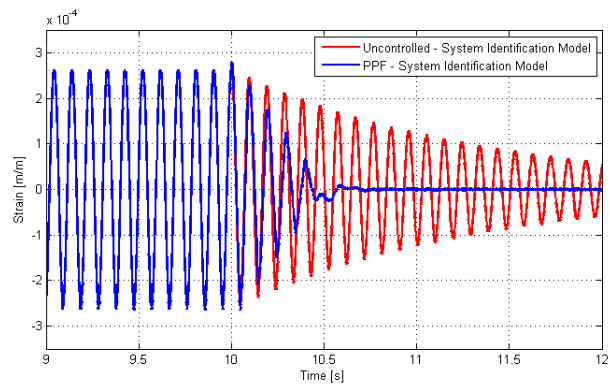


Figure 3-52 Free response performance of updated 3 mode PPF controller

3.6.2 Resonant Controller (RC)

Center frequencies of the 3 mode parallel RC controller are updated with respect to identified model natural frequencies. Gains and damping ratios of the three filters are also updated considering the identified model. Resulting controller parameters are given in Table 3-9.

Table 3-9 Updated three mode RC parameters

| RC#1 | | RC#2 | | RC#3 | | Overall Gain |
|------|---------------|------|---------------|------|---------------|--------------|
| Gain | Damping Ratio | Gain | Damping Ratio | Gain | Damping Ratio | |
| 2e-4 | 0.4 | 1E-4 | 0.2 | 2E-5 | 0.05 | 0.25E9 |

Forced and free response performances of the three mode RC controller are given in Figure 3-53 and Figure 3-54, respectively. Disturbance rejection for the first three modes is 18.1, 18.3 and 6.2 dB, respectively. When free response of the controller is observed, it is seen that controller can successfully damp the transient vibrations approximately in 0.73 seconds.

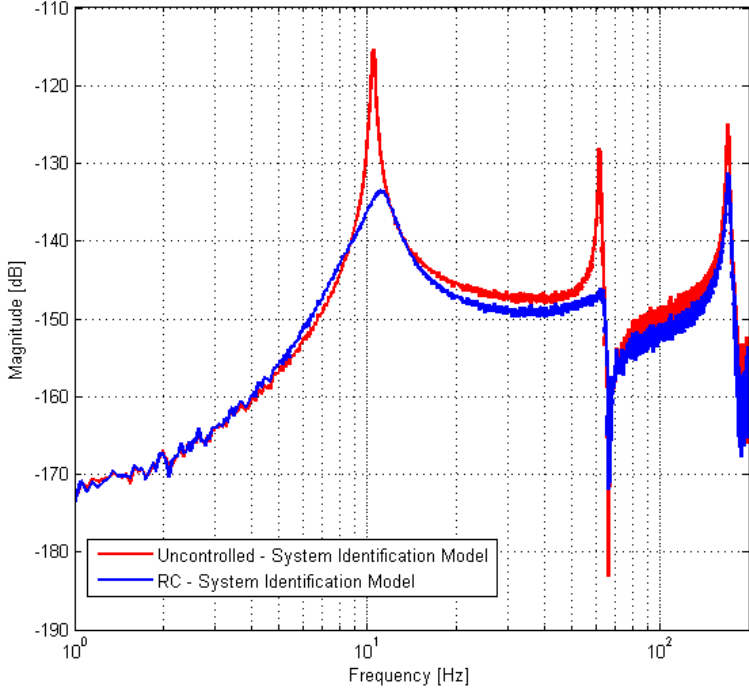


Figure 3-53 Forced response performance of updated 3 mode RC

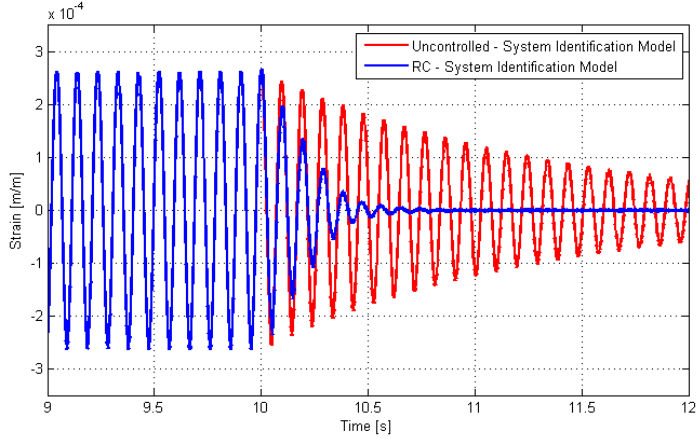


Figure 3-54 Free response performance of updated 3 mode RC

3.6.3 Integral Resonant Controller (IRC)

Updated controller parameters by considering the identified model are given in Table 3-10. Resulting forced and free response performance graphs are presented in Figure 3-55 and Figure 3-56, respectively.

Table 3-10 Updated Integral Resonant Control parameters

| K_G | K_{FT} | ω_b |
|-------|--------------|--------------------------|
| 0.3E8 | $-1.7448E-7$ | $2 \cdot \pi \cdot 3.75$ |

Forced response performance of the IRC controller shows that, vibration suppression in the first mode is 31.2 dB. Attenuations in other two modes are 15.5 and 2.5 dB, respectively. Suppression of the first mode greatly affects the free response performance. IRC controller can suppress the transient vibrations nearly in 0.60 seconds.

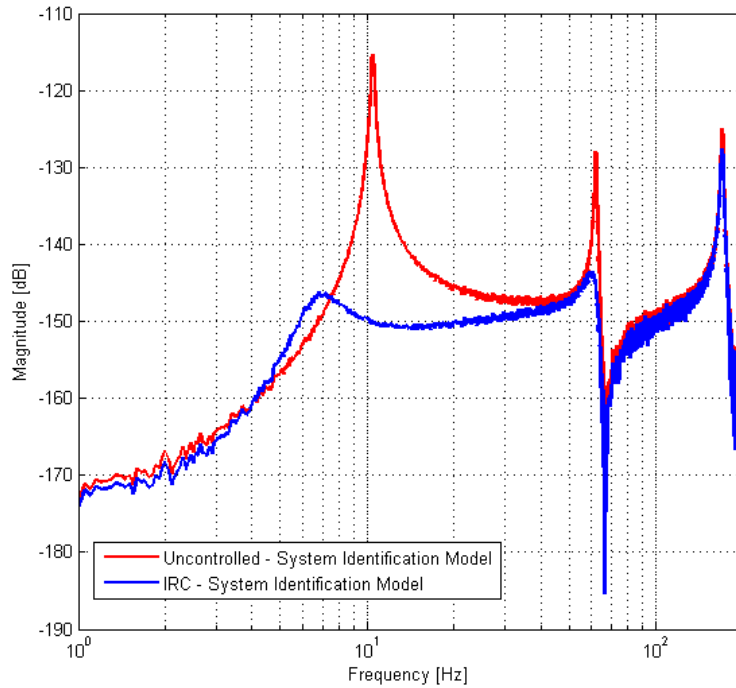


Figure 3-55 Forced response performance of updated IRC

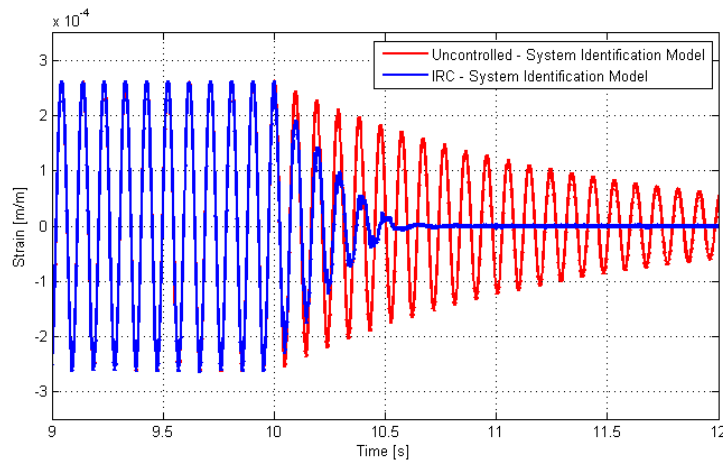


Figure 3-56 Free response performance of updated IRC

3.6.4 Positive Position Feedback with Feed-through (PPFFT)

PPFFT parameters updated with respect to system identification results are given in Table 3-11. Forced and free response performances of the PPFFT controller are given in Figure 3-57 and Figure 3-58, respectively.

Table 3-11 Updated PPFFT parameters

| PPF#1 | | | PPF#2 | | | PPF#3 | | | Overall Gain | Feed-through |
|------------|------|---------------|------------|------|---------------|------------|------|---------------|--------------|--------------|
| Freq. [Hz] | Gain | Damping Ratio | Freq. [Hz] | Gain | Damping Ratio | Freq. [Hz] | Gain | Damping Ratio | | |
| 7 | 9.1 | 0.85 | 51 | 70 | 0.3 | 168 | 26 | 0.025 | 0.2E9 | -1.8235 E-7 |

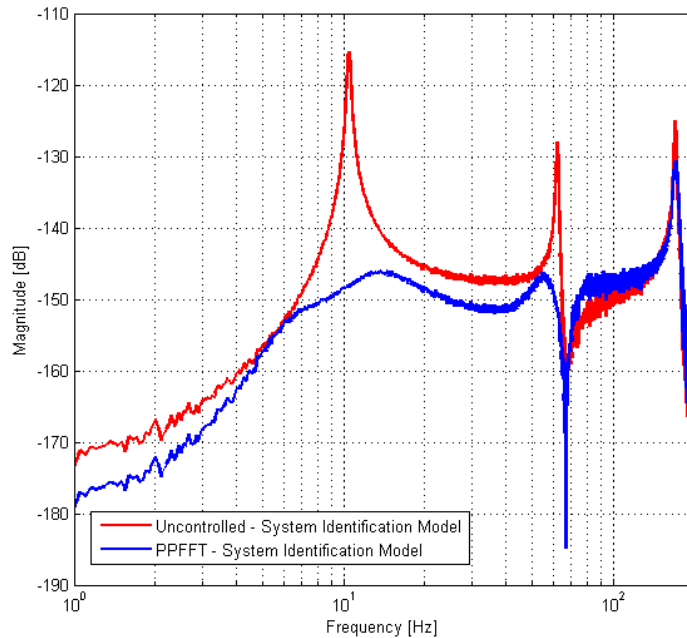


Figure 3-57 Forced response performance of updated PPFFT controller

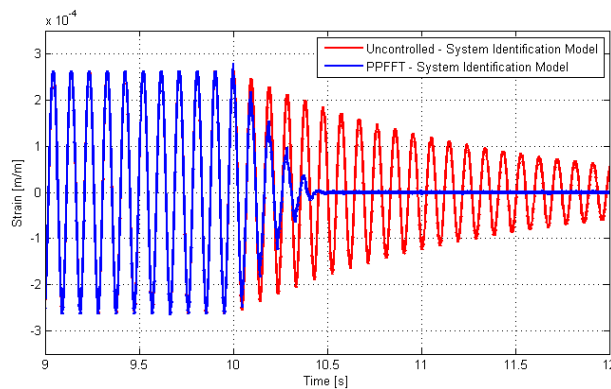


Figure 3-58 Free response performance of updated PPFFT controller

When forced response performance of the PPFFT controller is examined, it is seen that vibrations are suppressed up to 30.6, 18.3 and 5.7 dB for the first three modes, respectively. Free response performance shows that PPFFT controller can damp the transients approximately in 0.46 seconds.

3.7 Real-time applications of designed controllers

After system identification process, designed controllers have been updated. In order to see the performance of these controllers, they are implemented on the real structure. Details of real-time experiments of these controllers are presented in this section.

3.7.1 Positive Position Feedback (PPF)

PPF controller designed after system identification process is implemented on the real structure. Forced and free performance results of the real-time experiment are given in Figure 3-59 and Figure 3-60.

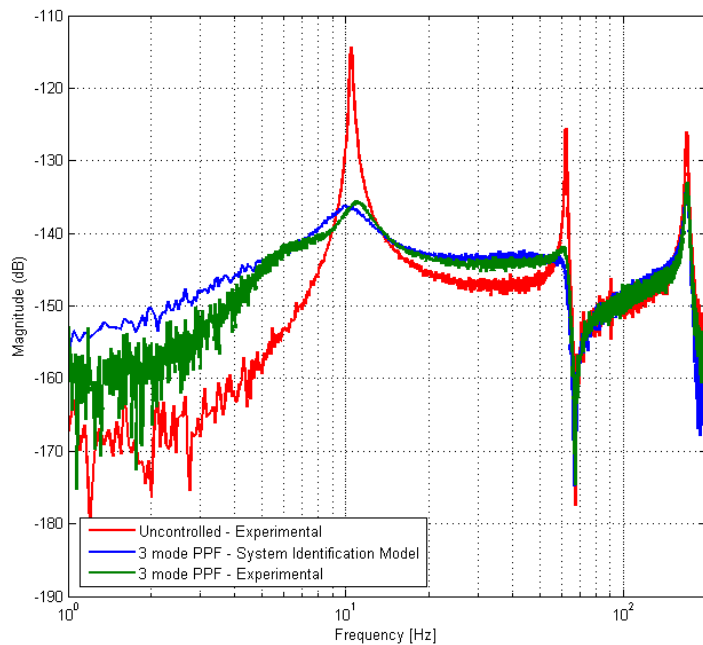


Figure 3-59 Experimental forced response performance of PPF controller

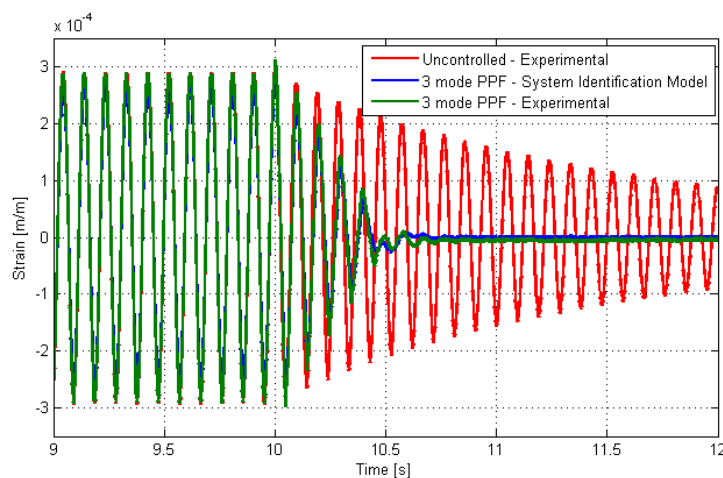


Figure 3-60 Experimental free response performance of PPF controller

When the experimental forced response performance of PPF controller is investigated, it can be seen that it is in good agreement with the estimated one. There exist some small discrepancies in resonance regions (0.6, 0.6 and 0.3 dB for the first three modes, respectively). The offset in free response performance is around 40 milliseconds. Hence, both steady- state and transient response performance of the designed controller are verified by experiments. Results show a highly reasonable consistency.

3.7.2 Resonant Controller (RC)

Real-time experiments show that gains of designed resonant controller make the system unstable. When the basis of this problem is investigated, it is determined that high frequency residual modes (higher than 200 Hz) which are not included in the identified model become unstable. For this reason gains and damping ratios of the designed controller are reduced to obtain a stable system response with maximum damping performance. Parameters of RC used in experiments are given in Table 3-12.

Table 3-12 Experimentally stable 3 mode RC parameters

| RC#1 | | RC#2 | | RC#3 | | Overall Gain |
|------|---------------|------|---------------|------|---------------|--------------|
| Gain | Damping Ratio | Gain | Damping Ratio | Gain | Damping Ratio | |
| 1e-4 | 0.10 | 1E-4 | 0.10 | 2E-5 | 0.05 | 0.6E8 |

Forced and free response performances of experimentally stable, resonant controller are given in Figure 3-61 and Figure 3-62.

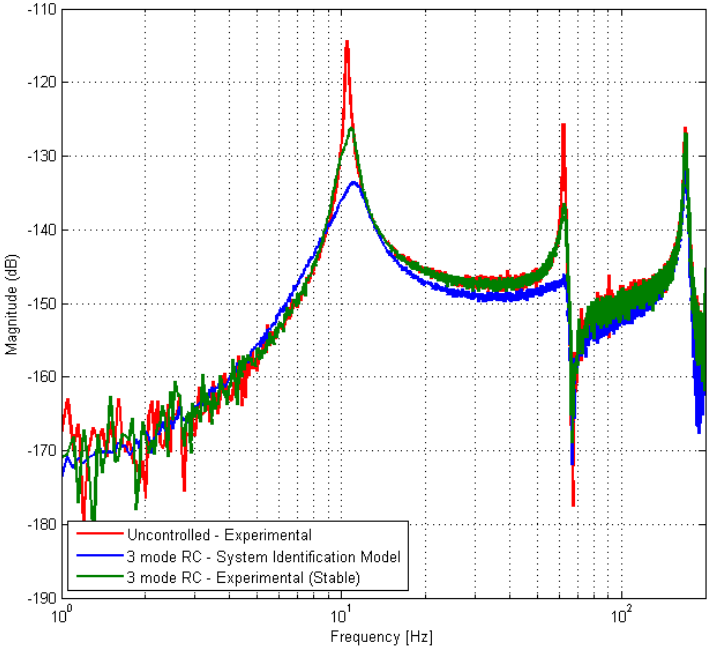


Figure 3-61 Experimental forced response performance of RC

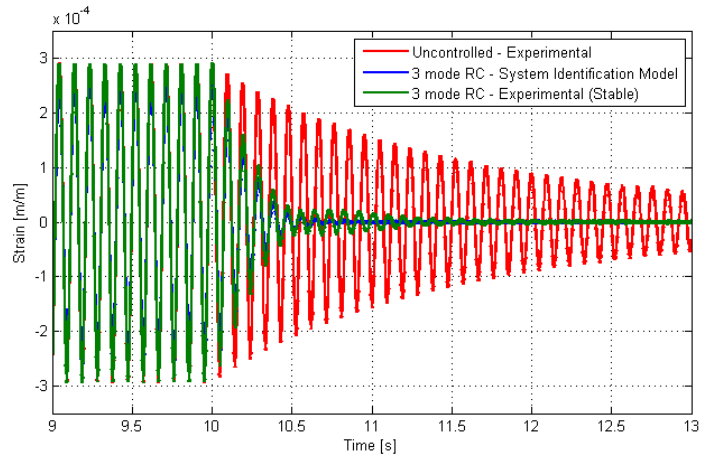


Figure 3-62 Experimental free response performance of RC

Performance of the experimentally stable RC is much worse than the designed stable RC. The differences in frequency domain response reach to 7.3, 9.9 and 4.3 dB for the first three resonances, respectively. Transient performance of the experimentally stable RC is approximately 1 second inferior to the one of designed stable RC.

Experimental results show that, for resonant controller design, the number of modes included in dynamic plant model should be higher than the highest mode to be controlled.

3.7.3 Integral Resonant Controller (IRC)

Integral resonant controller designed on the identified model is implemented to the real structure. Experimental forced and free response performance of this controller is presented in Figure 3-63 and Figure 3-64, respectively.

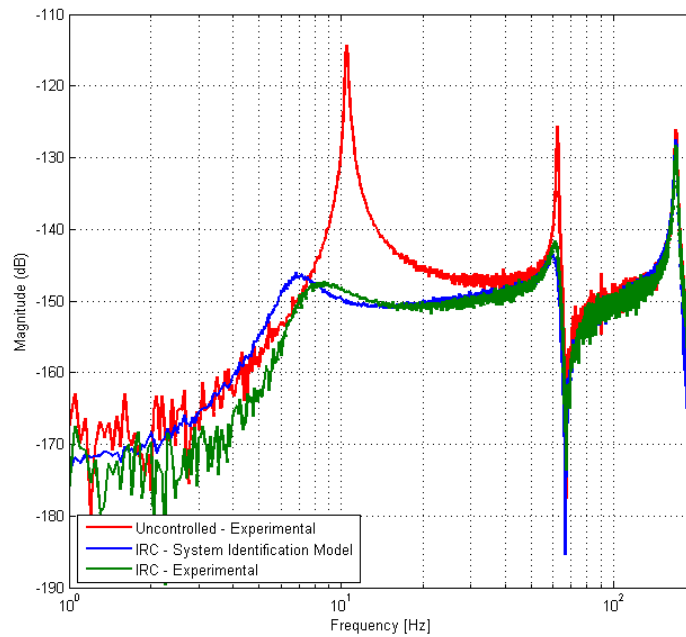


Figure 3-63 Experimental forced response performance of IRC

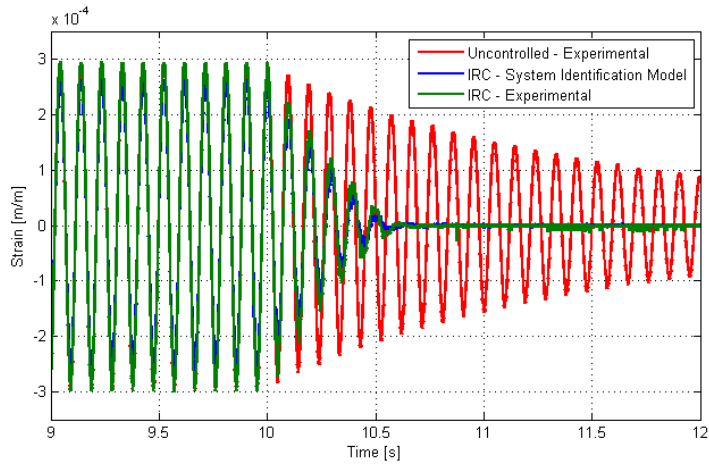


Figure 3-64 Experimental free response performance of IRC

Experimental steady-state performance of IRC differs 0.6, 1.9 and 1 dB from the performance estimations based on the identified model for the first three resonances. Discrepancy in transient performance is in the order of 20 milliseconds. Hence it can be concluded that experimental performance results of integral resonant controller are consistent with the ones obtained in simulations.

3.7.4 Positive Position Feedback with Feed-through (PPFFT)

Experimental forced and free response performances of designed PPFFT are given in Figure 3-65 and Figure 3-66.

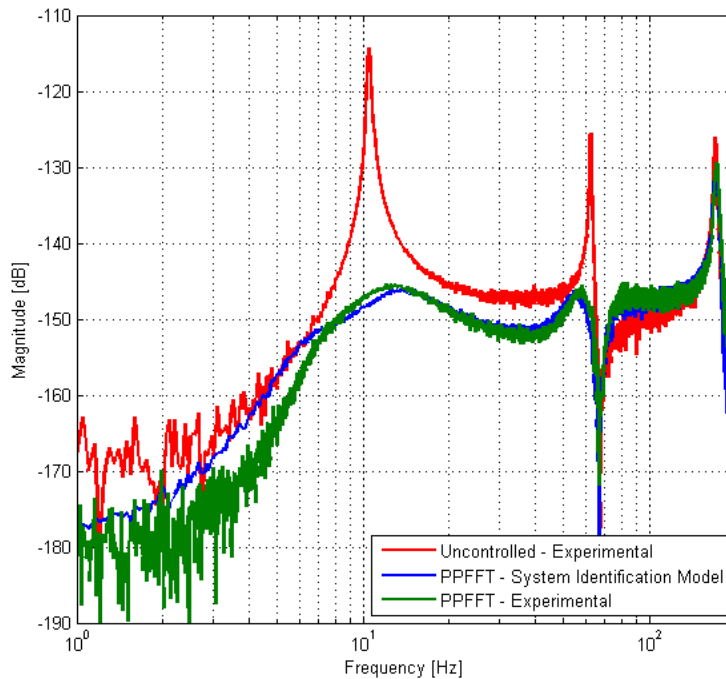


Figure 3-65 Experimental forced response performance of PPFFT controller

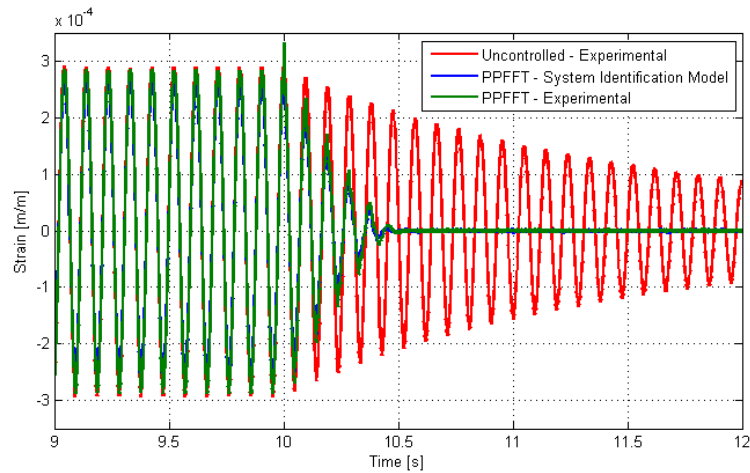


Figure 3-66 Experimental free response performance of PPFFT controller

Real-time forced response performance of the PPFFT controller is 0.6, 0.7 and 0.8 dB lower than the one obtained in design simulations. Moreover, it is experimentally shown that, designed PPFFT controller can also reduce the settling time of defined transients from 11.9 seconds to 0.48 seconds (see Figure 3-67). Deviation from the estimation is about 20 milliseconds. Considering the close agreement between the results of simulations and experiments, it can be said that performance estimations on PPFFT control are verified experimentally.

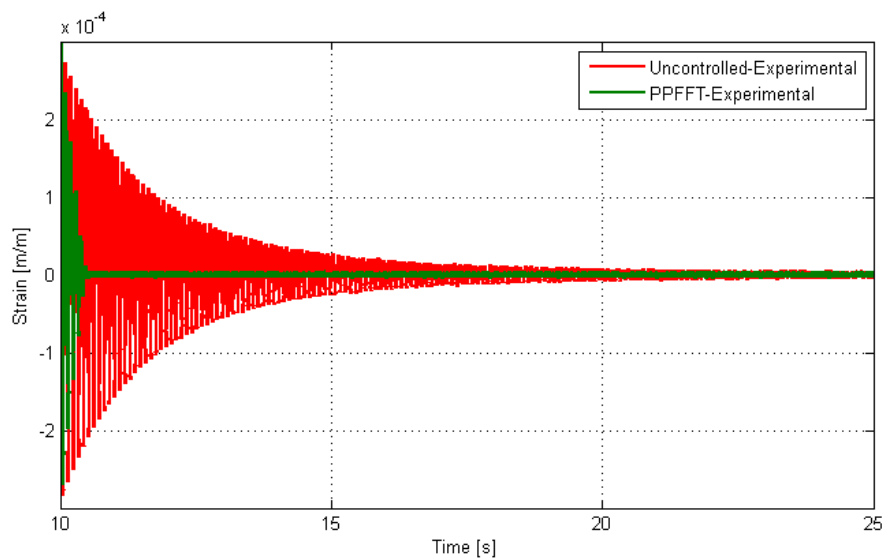


Figure 3-67 Experimental free response performance of PPFFT controller (2)

3.8 Conclusions

Forced and free response performances of Positive Position Feedback (PPF), Resonant Control (RC), Integral Resonant Control (IRC) and Positive Position Feedback with Feed-through (PPFFT) controllers are summarized in Table 3-13. It should be noted that parameters of all of these controllers are chosen in order to obtain maximum modal damping while not causing the actuator be saturated. While comparing the performance results of these controllers, this objective should be kept in mind.

Table 3-13 Summary of the performance of controllers

| | | Strain Response | | | | Tip Displacement Response | | | |
|---------------------|--------------|-----------------|-----------------|-----------------|-----------------|---------------------------|-----------------|-----------------|-----------------|
| | | Free (s) | Forced (dB) | | | Free (s) | Forced (dB) | | |
| | | | 1 st | 2 nd | 3 rd | | 1 st | 2 nd | 3 rd |
| FEM | Uncontrolled | 7,43 | -115,2 | -135,1 | -133,3 | 7,43 | -20,5 | -53,1 | -53,8 |
| | PPF | 0,81 | -138,4 | -143,4 | -138 | 0,81 | -47,1 | -62,7 | -58 |
| | RC | 0,75 | -137 | -150 | -137,5 | 0,78 | -40,6 | -64,6 | -55,6 |
| | IRC | 0,74 | -148 | -145,2 | -134,8 | 0,89 | -44,6 | -61,7 | -55,2 |
| | PPFFT | 0,57 | -145,2 | -146,3 | -136,3 | 0,54 | -49,2 | -63,1 | -58,5 |
| Identified | Uncontrolled | 6,71 | -115,4 | -128 | -125 | - | - | - | - |
| | PPF | 0,74 | -136,3 | -142,4 | -133,3 | - | - | - | - |
| | RC | 0,73 | -133,5 | -146,3 | -131,2 | - | - | - | - |
| | IRC | 0,6 | -146,6 | -143,5 | -127,5 | - | - | - | - |
| | PPFFT | 0,46 | -146 | -146,3 | -130,7 | - | - | - | - |
| Experimental | Uncontrolled | 11,9 | -114,4 | -125,6 | -126,3 | - | - | - | - |
| | PPF | 0,78 | -135,7 | -141,8 | -133 | - | - | - | - |
| | RC | 1,71 | -126,2 | -136,4 | -126,9 | - | - | - | - |
| | IRC | 0,62 | -147,2 | -141,6 | -128,5 | - | - | - | - |
| | PPFFT | 0,48 | -145,4 | -145,6 | -129,9 | - | - | - | - |

The following conclusions are drawn considering the results obtained:

- Controller performance estimations based on reduced order finite element model are successful when the damping assumptions are close to the real damping properties (see Table 3-7 and Table 3-13). In order to prepare a realistic finite element model, modal damping ratios of the structure to be controlled can be obtained with experimental modal analyses.
- Plant model synthesized after system identification is quite successful to reflect the dynamics of the real structure. Controller performance predictions based on identified model are in pretty good agreement with experimental results.

- Due to its low-pass nature, PPF method causes amplification of quasi-static response, especially in multi-mode case. This effect is perceived more severely in collocated sensor location, which yields saturation of the actuator for small gains, limiting the performance of the controller.
- RC method is very vulnerable to noise and truncated high frequency modes, because of its high-pass nature. Hence, while designing a resonant controller, one should be really careful about the number of modes included in plant model and noise characteristics. Unmodeled dynamics and misinterpreted noise may cause the system to be unstable, as observed in this study.
- Low-pass characteristic (-20dB/decade roll-off) of the IRC method reduces its susceptibility to noise and truncated modes. However, it diminishes the authority of the controller on higher modes. Moreover, higher gains in lower frequencies may lead actuator to be saturated if not filtered.
- PPFFT method suggested in this study presents superior performance in out-of-resonance frequencies compared to its predecessor, PPF controller, especially when quasi-static sensor response is considered. This prevents the saturation in relatively low control gains; hence, results in improvement of steady-state response performance. PPFFT controller also shows better performance in transient response compared to other three (PPF, RC and IRC) controllers.
- It should be noted that noisy frequency responses are obtained in both discrete-time simulations and experiments, especially for the frequencies with low response levels. The reason of this problem is the low signal-to-noise-ratio. A thinner host structure or a thicker piezoelectric patch actuator can be used in further studies to eliminate this problem.
- All control methods fail to effectively suppress the third bending mode, because of the lower controllability of the third mode which is a result of actuator location choice. Detailed discussion of influence of actuator location on controllability is presented in Chapter 2 and Chapter 4.

CHAPTER 4

ACTIVE VIBRATION CONTROL OF A RECTANGULAR PLATE WITH FOUR CLAMPED EDGES

4.1 Introduction

In Chapter 3, a design procedure including coupled-field (piezoelectric) finite element analyses in ANSYS Workbench, model order reduction and modal controller design in MATLAB/SIMULINK is presented in order to control the first three modes of a cantilever beam. In this chapter, the proposed design procedure is implemented on a rectangular plate with four clamped edges.

For the structures having more than one dimension (2D/3D), actuator and sensor locations significantly affect the performance of a modal control system. Hence, actuators and sensors should be placed in regions where controllability and observability is high, respectively. However, for a vibration control system these regions are dissimilar for infinite number of modes of the structure. For structures with complex geometries and/or boundary conditions this task is more crucial and troublesome.

In literature, different optimization criteria have been suggested to determine locations of the actuators and sensors including maximizing modal forces/moments, maximizing deformation of the structure, minimizing control effort, maximizing controllability and maximizing observability which are explained in Chapter 2 in details. However, most of these studies are based on an analytical model of a plate with simply supported or cantilever boundary conditions. In other studies, finite element models are used. In this case reduced order models for each possible location of actuators and sensors need to be generated which requires tremendous computation time for a structure with complex geometry and/or boundary conditions. If the finite dimensions of commercially available piezoelectric patches are taken into account, problem becomes more complicated.

An alternative approach mentioned in literature is to place actuators and sensors to the regions where modal strain energies are high. This approach is more reasonable when complex structures are considered. Because in most of the cases one finite element modal analysis will be sufficient in order to obtain the required information. By considering its practical advantages, modal strain energy method has been adopted in determination of piezoelectric actuator locations. Since suggested control method works in collocated actuator and sensor configuration, strain sensors should be placed beneath the actuators.

Successful implementation of suggested PPFFT method on a cantilever beam structure is presented in Chapter 3. In this chapter, validity of the proposed method has been demonstrated for a multi-input multi-output case. In the design of the PPFFT controller, it is aimed to suppress vibrations of the first three modes of the structure with three actuator/sensor pairs. Due to hardware limitations, designed controller could not be validated with experiments on a real structure. However, the results presented in Chapter 3 shows that real-time performance of PPFFT controller can be estimated by control simulations based on reduced order finite element models.

4.2 Structure to be Controlled

A rectangular aluminum plate (700 x 400 x 1.5 mm) with four clamped edges is studied in this chapter. Aluminum material properties used in the simulations are given in Table 4-1.

Table 4-1 Material properties of aluminum

| Property | Value |
|------------------------------|-------|
| Density (kg/m ³) | 2770 |
| Modulus of Elasticity (GPa) | 71 |
| Poisson's Ratio | 0.33 |

Natural frequencies of the first six flexural vibration modes of the structure are given in Table 4-2. Extracted mode shapes for these modes are presented in Figure 4-1. It is assumed that all modes have the same, 1%, modal damping ratio.

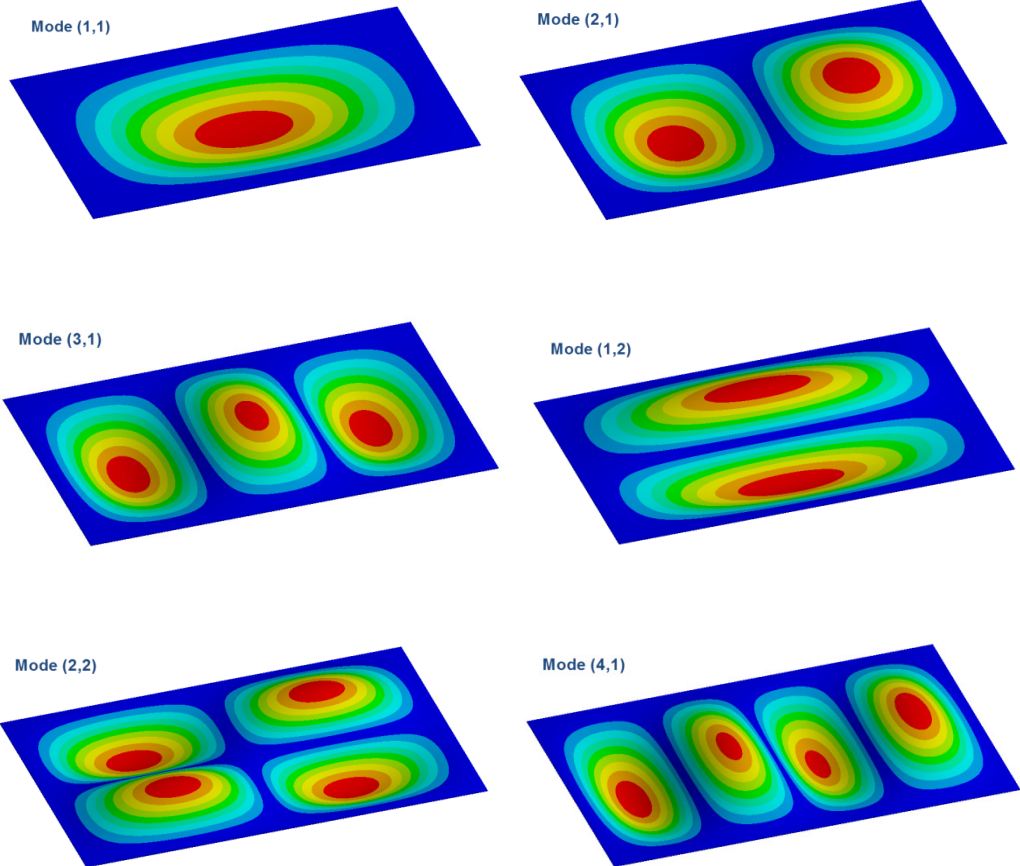


Figure 4-1 First six flexural mode shapes of the structure

Table 4-2 First six natural frequencies of the structure

| Mode | Frequency [Hz] | Mode | Frequency [Hz] |
|-------|----------------|-------|----------------|
| (1,1) | 58.87 | (1,2) | 149.85 |
| (2,1) | 82.20 | (2,2) | 172.07 |
| (3,1) | 122.91 | (4,1) | 180.25 |

4.3 Actuator and Sensor Placement

In this study, it is aimed to place the actuators and sensors to the areas with high modal strain energy. Since it is aimed to control the first three modes, strain energies in these modes are investigated. Strain energy distributions on the structure for the first three modes are given in Figure 4-2 to Figure 4-4.

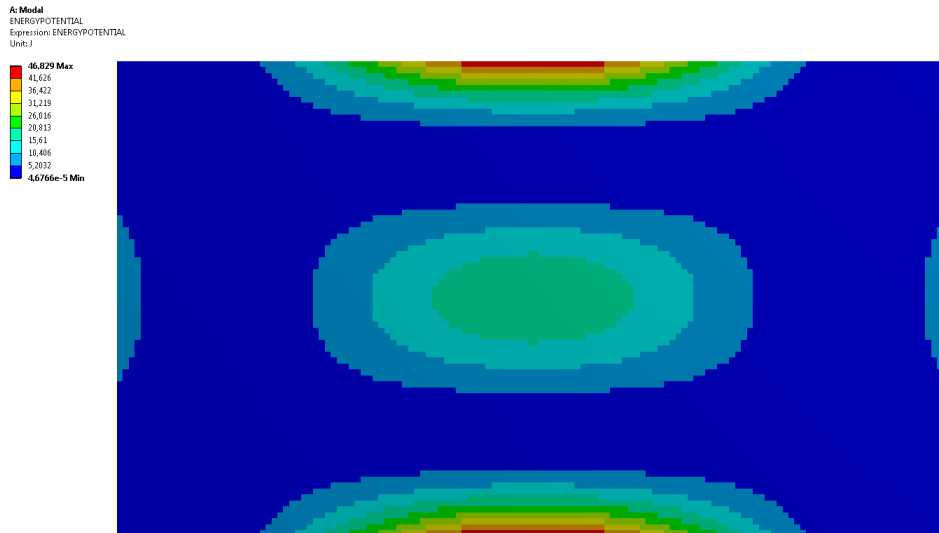


Figure 4-2 Strain energy distribution for the first mode

Determined design limitations for the placement of the piezoelectric patches are listed below:

- There should be 5 mm clearance from each clamped edge considering practical issues.
- Three piezoelectric patches (PI DuraAct P-876.A12) with 50 x 30 x 0.2 piezoceramic layer dimensions will be used.
- Control input for each piezoelectric patch is generated by using feedback of the collocated single axis strain sensor. Hence not only energies but also directivities of modal strains should also be considered.
- None of the modes has priority over the other modes. That is to say, each one of the first three modes has the same importance.

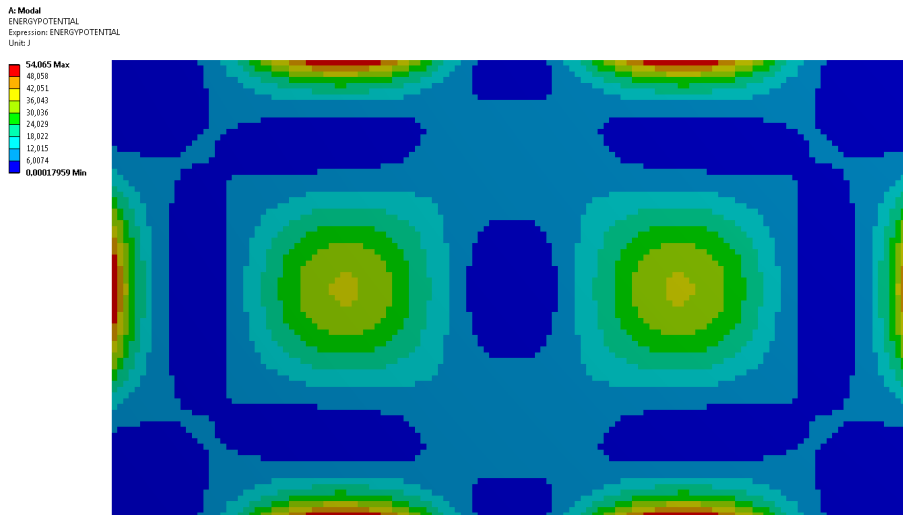


Figure 4-3 Strain energy distribution for the second mode

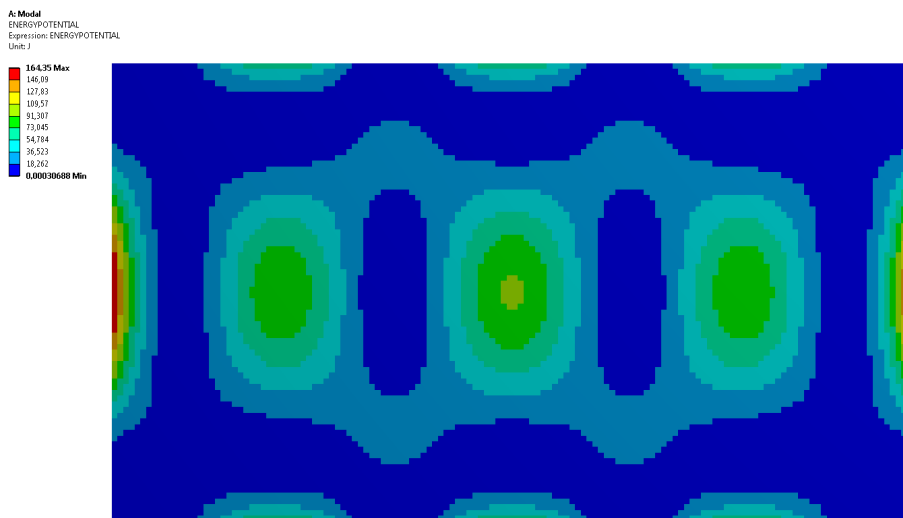


Figure 4-4 Strain energy distribution for the third mode

By considering the limitations mentioned above, seven different patch location alternatives have been defined. These alternatives are shown on a drawing in Figure 4-5. In order to define directions of strain feedback for these location alternatives, maximum modal normal strains are considered. Hence feedback directions given in Table 4-3 are defined for each patch location alternative.

Table 4-3 Directions of strain feedback for seven patch location alternatives

| | | Alternatives | | | | | | |
|-----------|---|--------------|----|----|----|----|----|----|
| | | #1 | #2 | #3 | #4 | #5 | #6 | #7 |
| Direction | Y | X | Y | X | Y | X | X | |

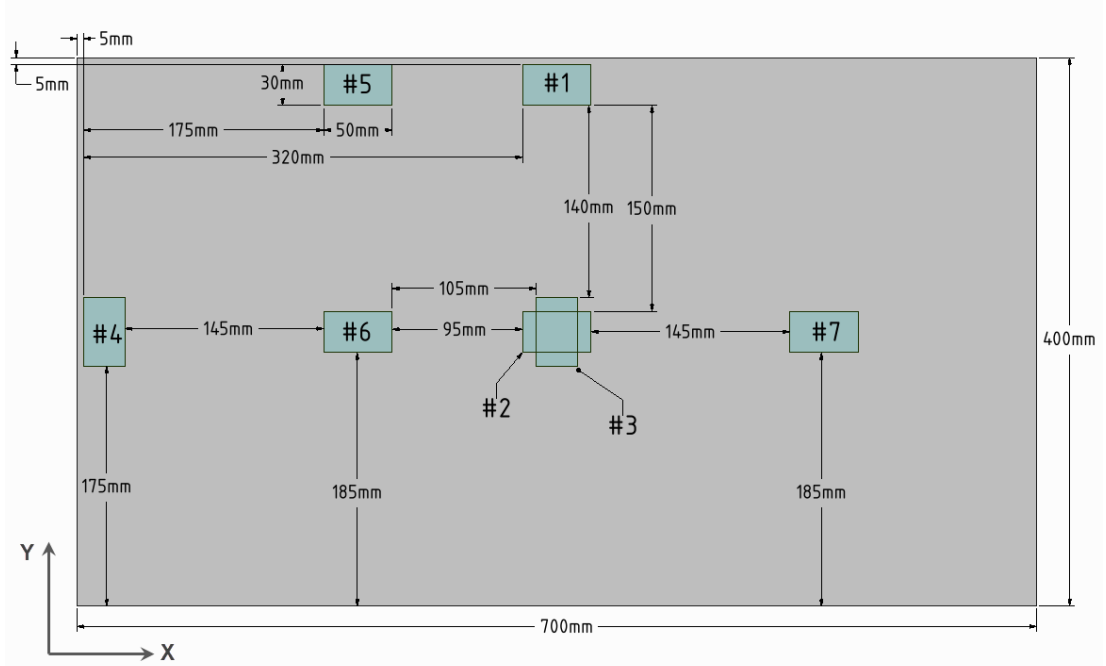


Figure 4-5 Seven location alternatives for piezoelectric patch bonding

Distributions of modal normal strains in X axis on the alternative patch locations (#2, #4, #6 and #7), which work with strain feedback in X axis (see Table 4-3), are given in Figure 4-6 to Figure 4-8. Modal normal strains (in Y axis) on the alternative patch locations (#1, #3 and #5) are given in Figure 4-9 to Figure 4-11. In order to determine the final patch locations, sum of directional modal strain energies for different location alternatives are compared. Equation used for calculation of the performance index (PI) for patch location selection is as follows:

$$PI = \sum_{Mod=1}^3 (PI_{Mod}) \quad (4.1)$$

where

$$PI_{Mod} = \left(\left(\frac{\text{Average of nodal strains on patch location alternative}}{\text{Maximum nodal strain on the entire structure}} \right)^2 \cdot 100 \right)_{Mod} \quad (4.2)$$

Square term in (4.2) indicates the proportionality of strain energy to the square of strain.

Based on the defined performance index in Equation (4.1), seven different piezoelectric patch location alternatives are compared in Table 4-4. When the performance indices are investigated, it is seen that modal controllability is highest in the patch location alternatives #1, #5 and #4 for the first three modes, respectively. Moreover, these locations are the best alternatives if the cumulative controllability over three modes is considered. Therefore, location alternatives #1, #4 and #5 are selected to bond the piezoelectric patches.

Table 4-4 Comparison of the patch location alternatives

| Mod | Performance Indices for Location Alternatives | | | | | | |
|-----|---|---------|---------|-------|------|------|------|
| | #1 | #2 | #3 | #4 | #5 | #6 | #7 |
| #1 | 62.7 | 2.9 | 34.1 | 12.7 | 31.0 | 0.9 | 0.1 |
| #2 | 1.7E-19 | 9.2E-21 | 1.3E-19 | 54.4 | 55.2 | 28.5 | 18.6 |
| #3 | 18.4 | 42.1 | 6.4 | 48.0 | 7.0 | 14.6 | 36.7 |
| Sum | 81.2 | 44.9 | 40.5 | 115.1 | 93.1 | 44.0 | 55.4 |

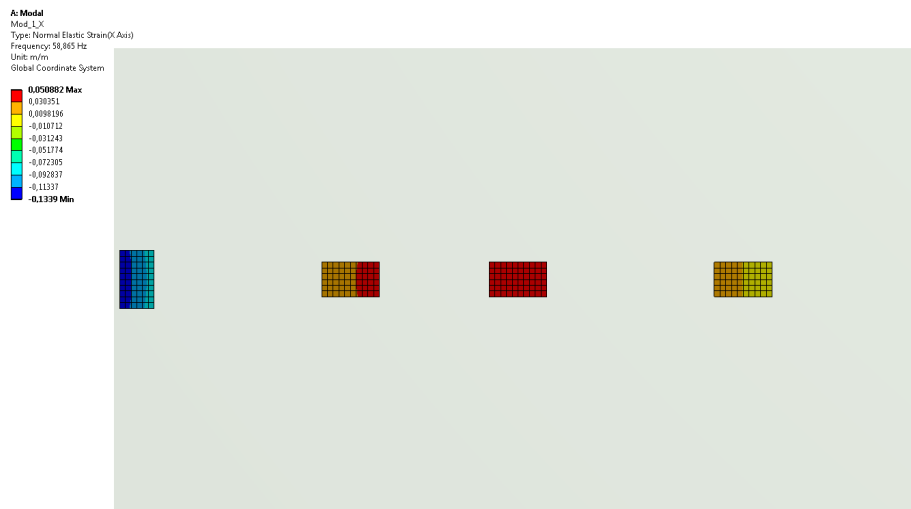


Figure 4-6 Normal strain -X on alternative patch locations for the first mode

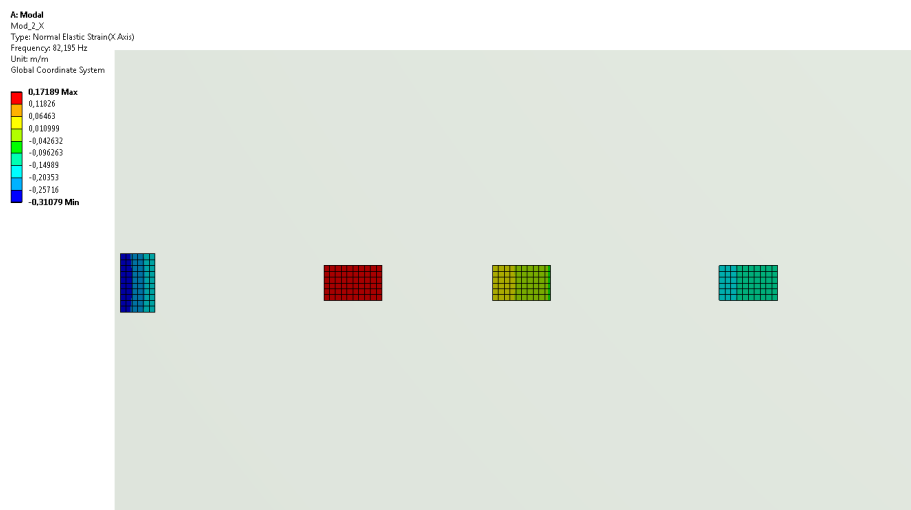


Figure 4-7 Normal strain -X on alternative patch locations for the second mode

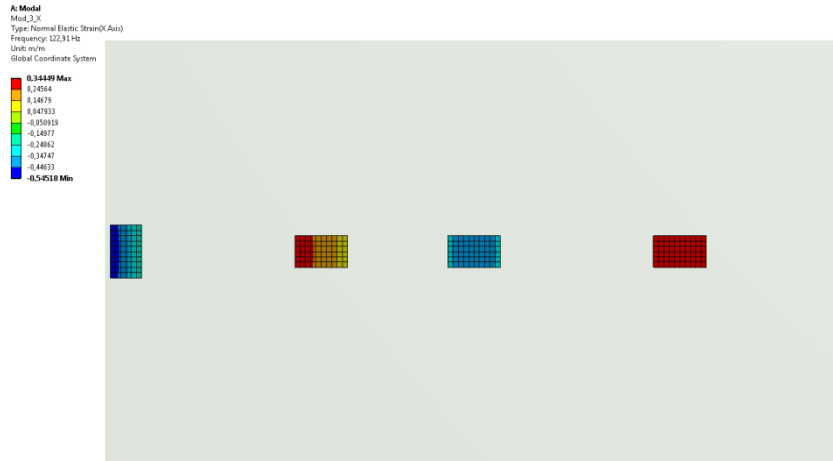


Figure 4-8 Normal strain $-X$ on alternative patch locations for the third mode

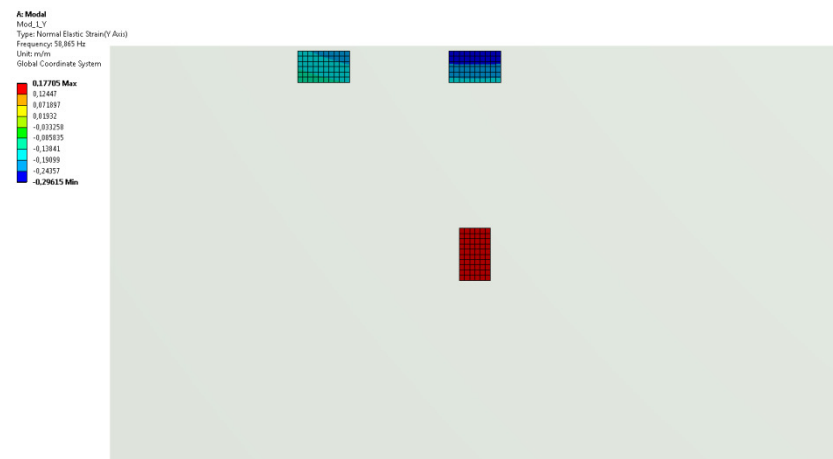


Figure 4-9 Normal strain $-Y$ on alternative patch locations for the first mode

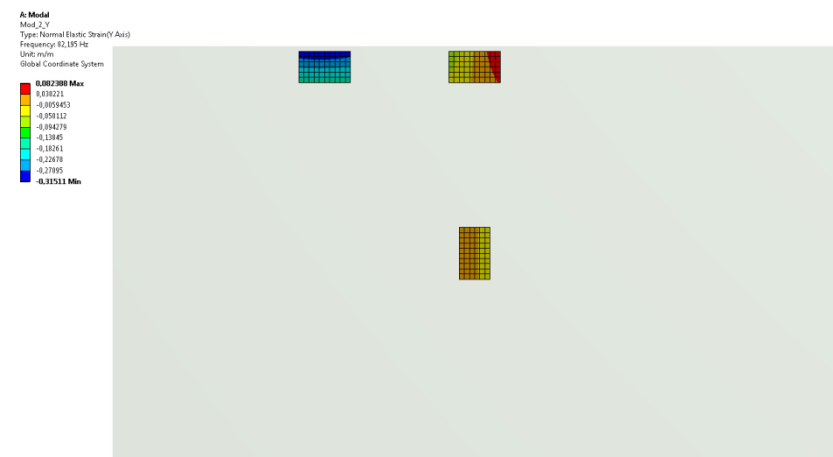


Figure 4-10 Normal strain $-Y$ on alternative patch locations for the second mode

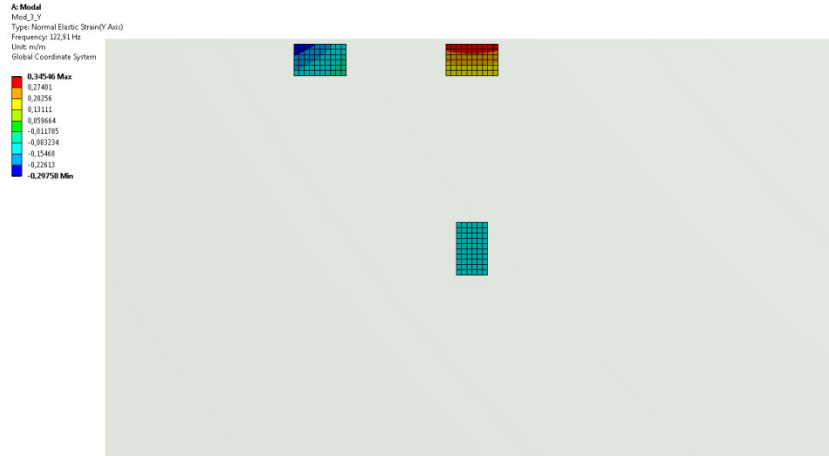


Figure 4-11 Normal strain –Y on alternative patch locations for the third mode

4.4 Finite Element Model

After the determination of the piezoelectric patch locations, finite element model of the plant to be controlled has been prepared in ANSYS Workbench 14.0. Mechanical and electrical material properties of the ceramic of the piezoelectric patch (PIC 255) are given in Table 4-5. Mesh of the finite element model has been shown in Figure 4-12.

Table 4-5 Material properties of PIC 255

| PIC 255 | | | |
|----------------|------------------------|------------------------------|-------------|
| ρ | 7800 kg/m ³ | C_{66}^E | 23.2 GPa |
| C_{11}^E | 123 GPa | e_{31} | -7.15 N/V.m |
| C_{12}^E | 76.7 GPa | e_{33} | 13.7 N/V.m |
| C_{13}^E | 70.3 GPa | e_{15} | 11.9 N/V.m |
| C_{33}^E | 97.1 GPa | $\epsilon_{11}^S/\epsilon_0$ | 930 |
| C_{44}^E | 22.3 GPa | $\epsilon_{33}^S/\epsilon_0$ | 857 |

First twelve natural frequencies of the structure are calculated again considering the short-circuited piezoelectric patch integration. Natural frequency results of the modal analysis are shown in Table 4-6. When these natural frequency results are compared with the ones obtained considering only host structure (plate with four clamped edges, *see Table 4-2*), it is obviously seen that piezoelectric patch integration to high modal strain areas slightly (in the order of 0.5%) shifts the natural frequencies of the host structure by increasing the stiffness of the structure.

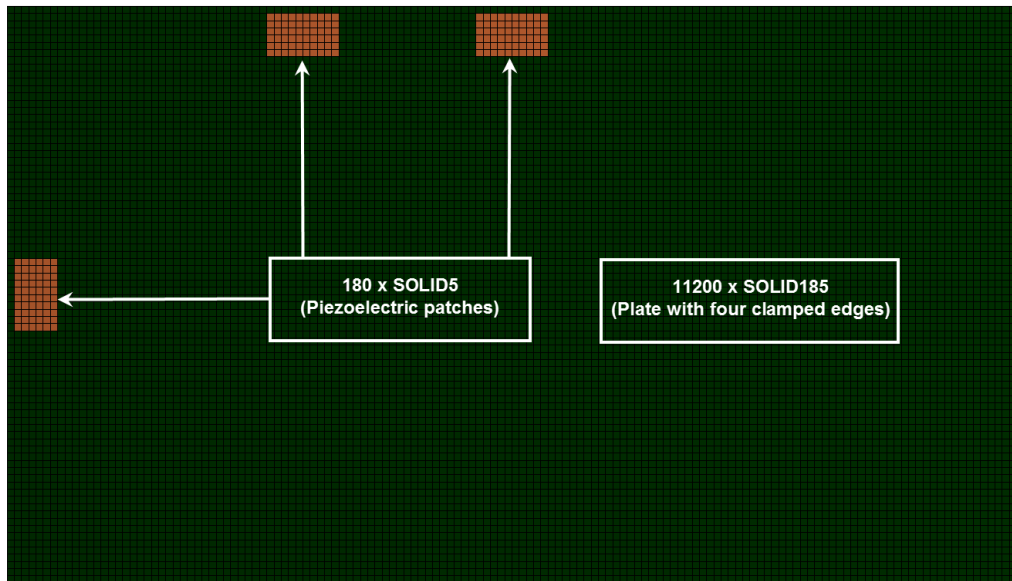


Figure 4-12 Mesh of the finite element model

Table 4-6 First twelve natural frequencies (short-circuited piezoelectric electrodes)

| Mode | Frequency [Hz] | Mode | Frequency [Hz] |
|-------|----------------|-------|----------------|
| (1,1) | 59.31 | (3,2) | 210.78 |
| (2,1) | 82.59 | (5,1) | 254.10 |
| (3,1) | 123.43 | (4,2) | 265.14 |
| (1,2) | 150.59 | (1,3) | 287.96 |
| (2,2) | 172.56 | (2,3) | 309.69 |
| (4,1) | 180.78 | (5,2) | 336.06 |

4.5 Order Reduction

Dynamic characteristics of the structure have been obtained from finite element analyses. However, presented finite element model includes approximately 70000 DOFs, which makes it almost impossible to be used in control simulations. Therefore, order of the plant obtained from finite element analyses should be reduced.

Prior to an order reduction process, inputs and outputs of the plant should be defined. Electric potentials on piezoelectric patches, a disturbance force which can excite the first three structural modes and an acceleration field are defined as inputs for the plant. Three axial strain responses obtained from the strain gages bonded beneath the piezoelectric patches and two acceleration responses which will monitor the behavior of the structure are defined as outputs for the plant. Figure 4-13 depicts the locations of the sensors and actuators, Table 4-7 represents numbering of the resulting 25 transfer functions.

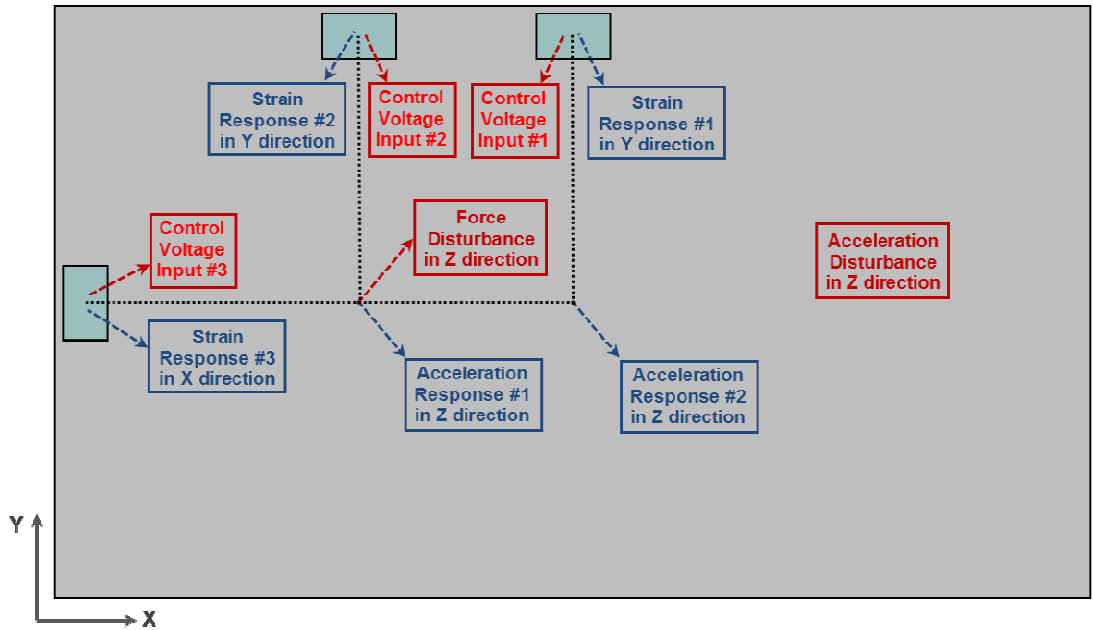


Figure 4-13 Inputs and outputs of the plant

Table 4-7 Numbering of the transfer functions

| Inputs \ Outputs | Control Voltage #1 [V] | Control Voltage #2 [V] | Control Voltage #3 [V] | Force Disturbance [N] | Acceleration Disturbance [g] |
|--------------------|------------------------|------------------------|------------------------|-----------------------|------------------------------|
| Strain#1 [m/m] | $G_{11}(s)$ | $G_{12}(s)$ | $G_{13}(s)$ | $G_{14}(s)$ | $G_{15}(s)$ |
| Strain#2 [m/m] | $G_{21}(s)$ | $G_{22}(s)$ | $G_{23}(s)$ | $G_{24}(s)$ | $G_{25}(s)$ |
| Strain#3 [m/m] | $G_{31}(s)$ | $G_{32}(s)$ | $G_{33}(s)$ | $G_{34}(s)$ | $G_{35}(s)$ |
| Acceleration#1 [g] | $G_{41}(s)$ | $G_{42}(s)$ | $G_{43}(s)$ | $G_{44}(s)$ | $G_{45}(s)$ |
| Acceleration#2 [g] | $G_{51}(s)$ | $G_{52}(s)$ | $G_{53}(s)$ | $G_{54}(s)$ | $G_{55}(s)$ |

Frequency response characteristics of the reduced order model should be in good agreement with the ones of the full order model at the frequency range of interest. By considering the desire to suppress first three modes, mentioned frequency range is determined as 0-160 Hz.

Frequency responses of reduced order model have been compared with the ones obtained by harmonic analyses in which complete stiffness, damping and mass matrices are used. After a few iterations, it has been concluded that contributions of minimum 12 modes (without residual vectors) are required to

capture frequency response characteristics up to 160 Hz. Sample comparison graphs are presented in Figure 4-14 to Figure 4-20.

By the way, it is desired to attract attention to an important property of collocated transfer functions ($G_{11}(s)$, $G_{22}(s)$ and $G_{33}(s)$). When frequency responses of these transfer functions (Figure 4-14, Figure 4-16 and Figure 4-18) and controllability indices (Table 4-4) generated based on modal strain energies are examined carefully, it can be seen that there is a correlation between magnitude of resonance responses and the controllability of modes. When the first resonance responses of these transfer functions are compared, it can be seen that first resonance response is maximum in $G_{11}(s)$ and minimum in $G_{33}(s)$. If the performance indices obtained for the first mode (see Table 4-4) are examined, it can be seen that controllability over the first mode is maximum for the location of the first patch and minimum for the location of the third patch.

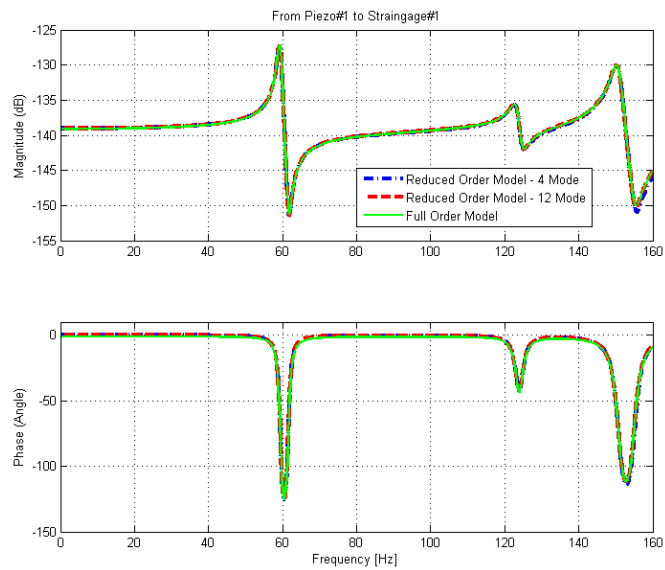


Figure 4-14 Frequency response of reduced and full order $G_{11}(s)$

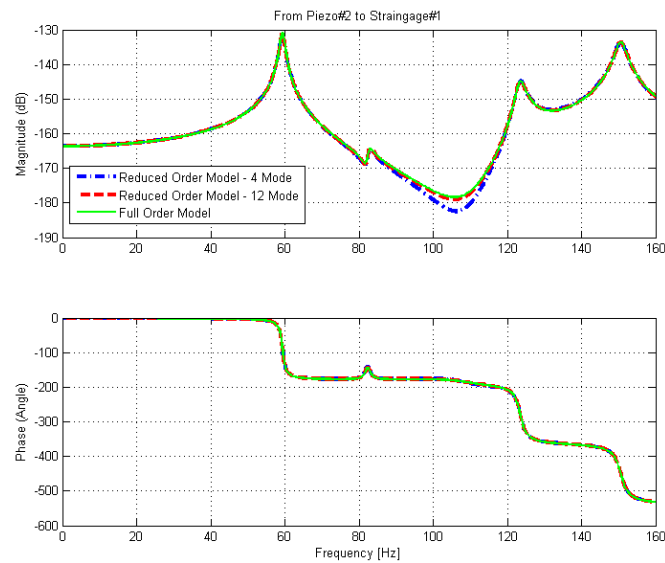


Figure 4-15 Frequency response of reduced and full order $G_{12}(s)$

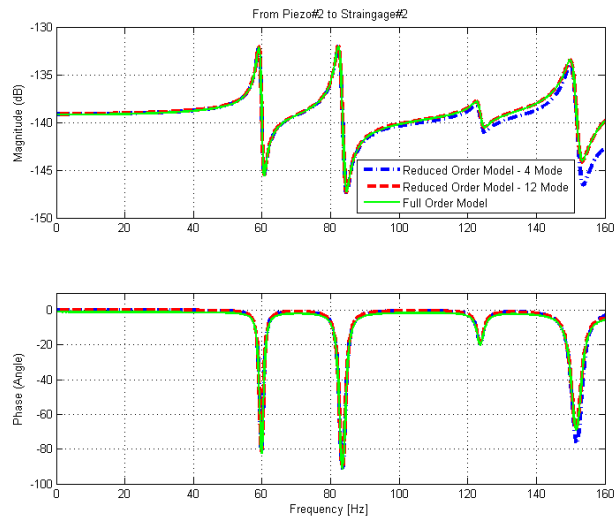


Figure 4-16 Frequency response of reduced and full order $G_{22}(s)$

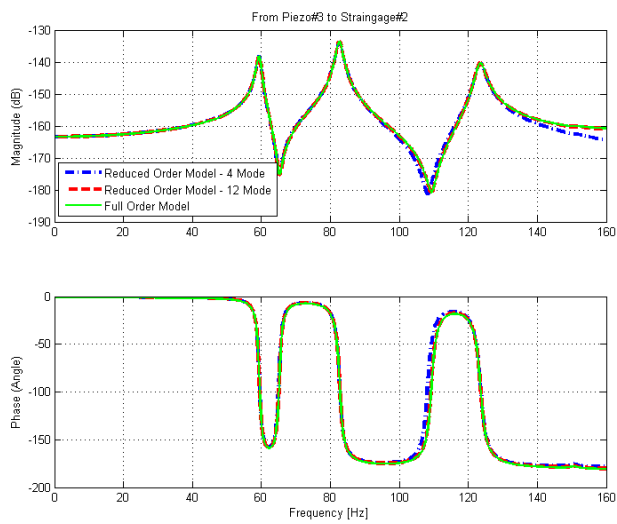


Figure 4-17 Frequency response of reduced and full order $G_{23}(s)$

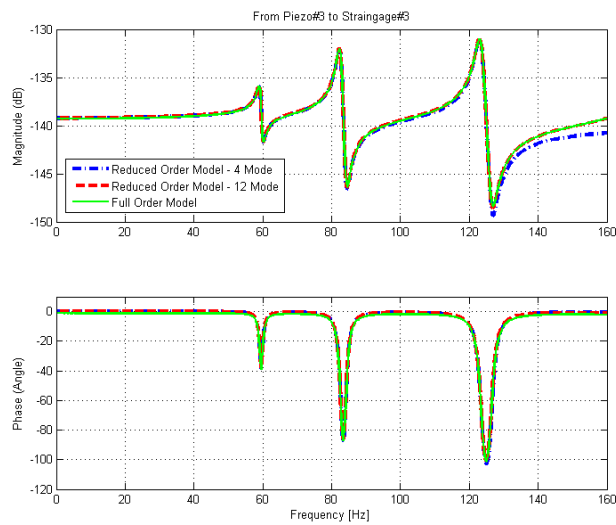


Figure 4-18 Frequency response of reduced and full order $G_{33}(s)$

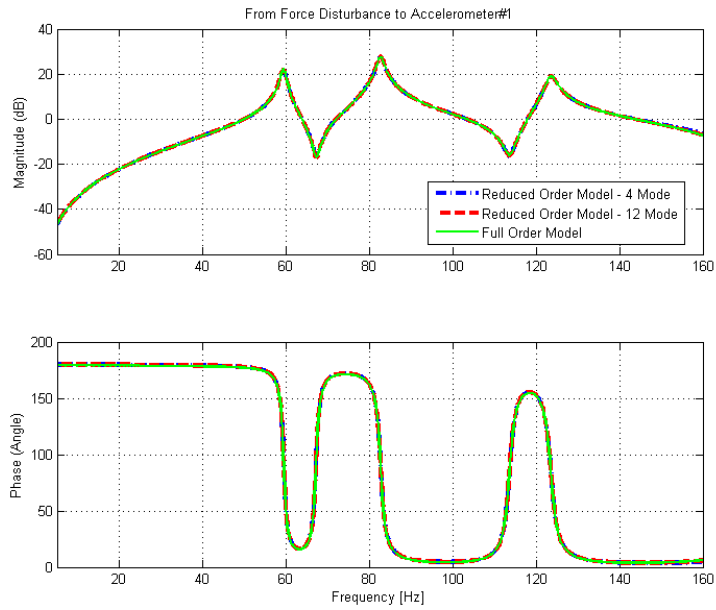


Figure 4-19 Frequency response of reduced and full order $G_{44}(s)$

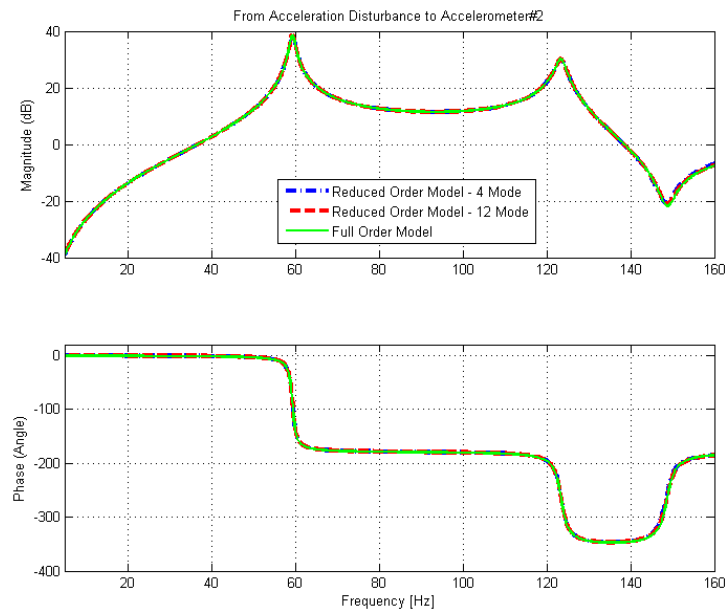


Figure 4-20 Frequency response of reduced and full order $G_{55}(s)$

4.6 Controller Design

In this section, it is aimed to synthesize a controller based on the suggested Positive Position Feedback with Feed-through (PPFFT) method. As previously mentioned, first three structural modes are aimed to be suppressed. For this purpose, three piezoelectric patches are used. That is to say, control system is comprised of three piezoelectric voltage inputs and three axial strain outputs, except disturbance generators and acceleration observers. Block diagram representation of the control scheme is presented in Figure 4-21.

As it can be seen from the proposed control scheme, each collocated transfer function is treated separately. Hence it is required to design three single-input single-output (SISO) controllers which are

responsible to augment the damping of the controllable modes. Studies on these controllers showed that use of filters with high damping ratios minimize the disruptive effects of each controller on the other ones.

As discussed previously, a feed-through term addition to a collocated transfer function results in a zero (anti-resonance) placement in a specific frequency. If the zero is placed before the first natural frequency, it counteracts the actuator saturating effect of Positive Position Feedback (PPF) filters. After several trials, it has been decided to place a zero at 50 Hz of the collocated transfer functions. Changes in the anti-resonance frequencies of the collocated transfer functions are presented in Figure 4-22 to Figure 4-24.

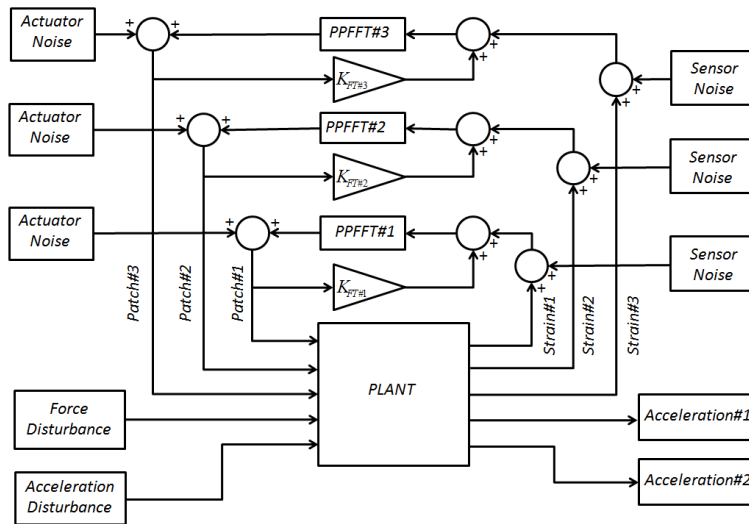


Figure 4-21 PFFFT Control Scheme with three actuators

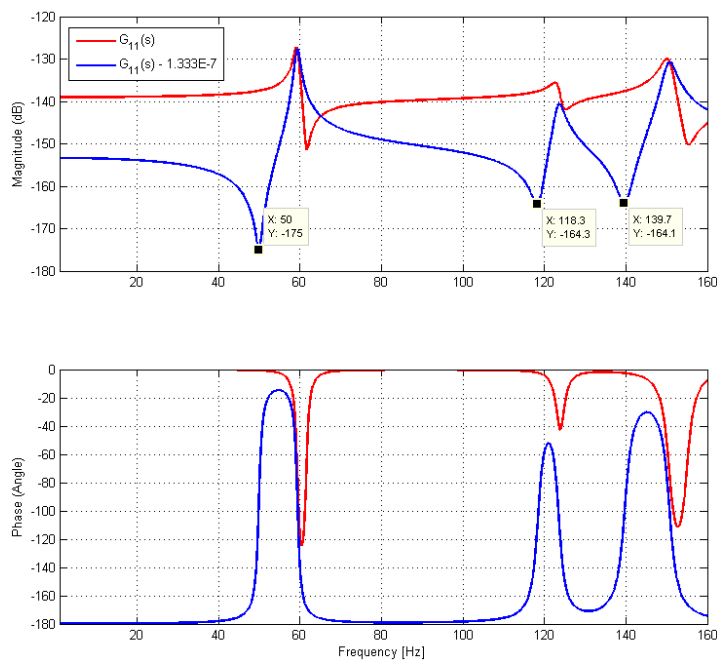


Figure 4-22 Effect of feed-through on collocated frequency response $G_{11}(s)$

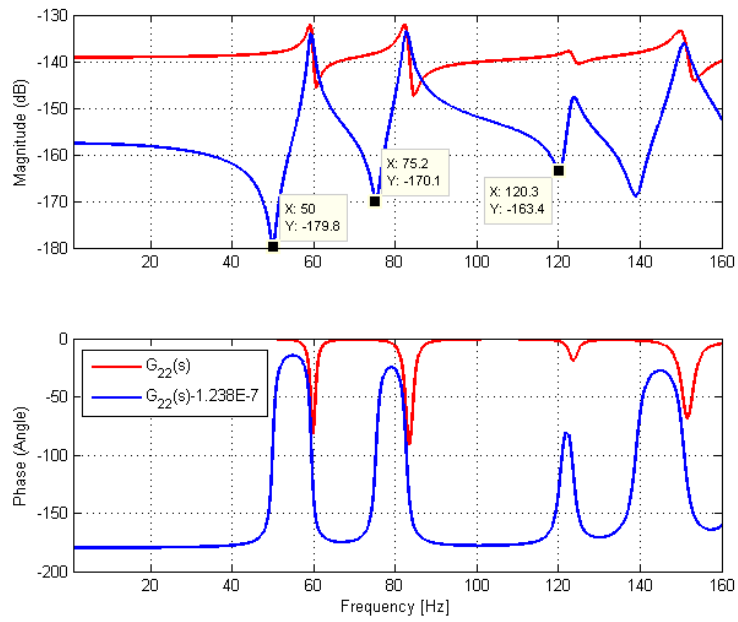


Figure 4-23 Effect of feed-through on collocated frequency response $G_{22}(s)$

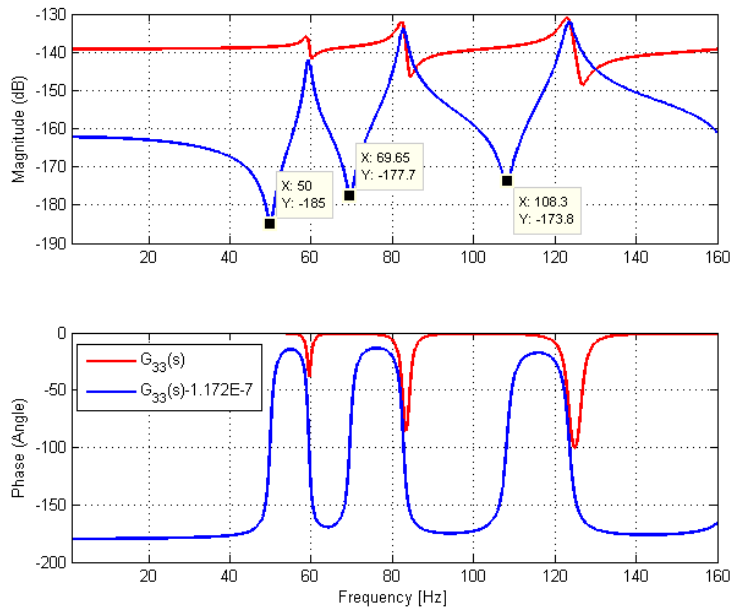


Figure 4-24 Effect of feed-through on collocated frequency response $G_{33}(s)$

Both second and third piezoelectric patches have controllability over not well-spaced three modes. Therefore, only one PPF filter has been used in controllers PPF#2 and PPF#3, in order to prevent control spillover. However, since first piezoelectric patch cannot excite the second mode, two PPF filters have utilized in PPF#3 in order to control first and third modes which are sufficiently spaced. Chosen PPF parameters are given in Table 4-8 to Table 4-10. Resulting root-locus diagrams showing the relocated poles and zeros are given in Figure 4-25 to Figure 4-27.

Table 4-8 Two mode PPFFT#1 controller parameters

| PPF#1 | | | PPF#2 | | | Feed-through |
|----------------|--------|---------------|----------------|---------|---------------|--------------|
| Frequency [Hz] | Gain | Damping Ratio | Frequency [Hz] | Gain | Damping Ratio | |
| 35 | 8.5E10 | 0.60 | 110 | 1.15E11 | 0.20 | -1.333E-7 |

Table 4-9 One mode PPFFT#2 controller parameters

| PPF | | | Feed-through |
|----------------|---------|---------------|--------------|
| Frequency [Hz] | Gain | Damping Ratio | |
| 60 | 1.45E11 | 0.55 | -1.238E-7 |

Table 4-10 One mode PPFFT#3 controller parameters

| PPF | | | Feed-through |
|----------------|---------|---------------|--------------|
| Frequency [Hz] | Gain | Damping Ratio | |
| 100 | 3.75E11 | 0.60 | -1.172E-7 |

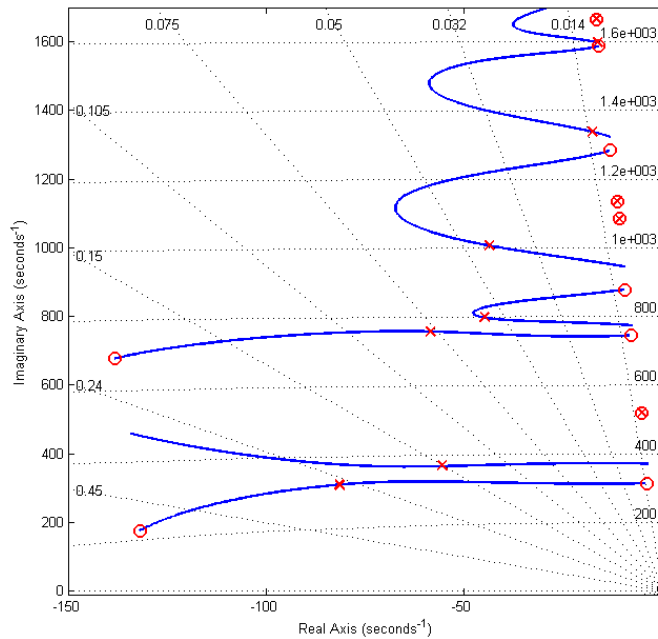


Figure 4-25 Root-locus and pole-zero map of PPFFT#1 controlled $G_{11}(s)$

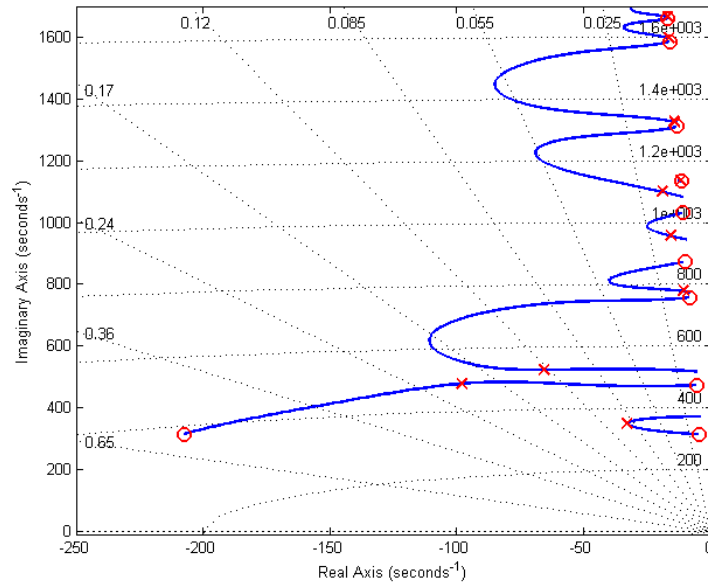


Figure 4-26 Root-locus and pole-zero map of PPF#2 controlled $G_{22}(s)$

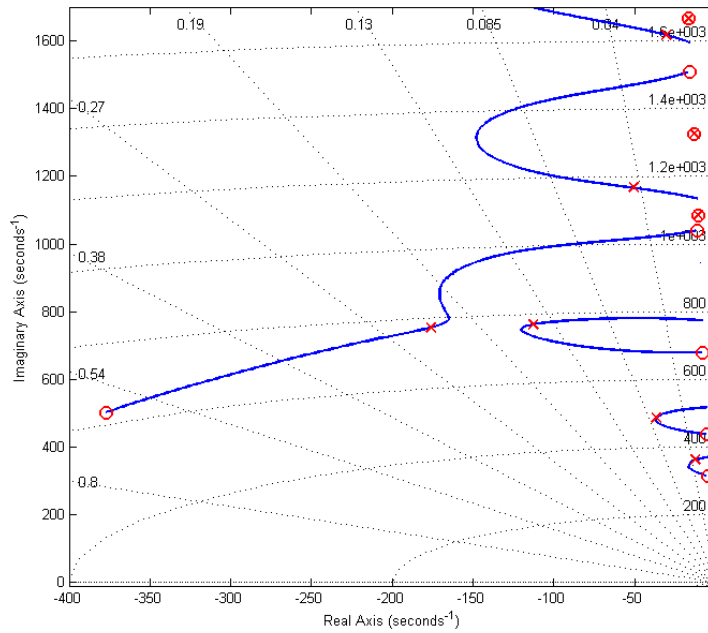


Figure 4-27 Root-locus and pole-zero map of PPF#3 controlled $G_{33}(s)$

Individual and cumulative disturbance rejection performances of three PPF controllers are presented in Figure 4-28 to Figure 4-31. It can be seen from these frequency responses, each PPF controller complements the other ones. As a result, approximately 24, 23 and 18 dB response attenuations in first three modes are achieved. However, quasi-static response of the structure is augmented by a degree of 5 dB. This is an inevitable consequence of positive feedback controllers. In design phase of PPF, it is aimed to achieve maximum modal damping while minimizing the amplification in quasi-static region.

Designed continuous-time controllers should be checked by discrete-time simulations under the influence of time delay, noise and actuator saturations. For these simulations, continuous-time system model and PPF controllers are discretized by using Tustin (bilinear) transformation for 10kHz

sampling rate. Noises of piezoelectric amplifier and strain gage are modeled as white noise with -40 and -150 dB power, respectively (see Section 3.4.1). Operating voltage range of the piezoelectric patches (PI DuraAct P-876.A12) is considered to be -50/+350V.

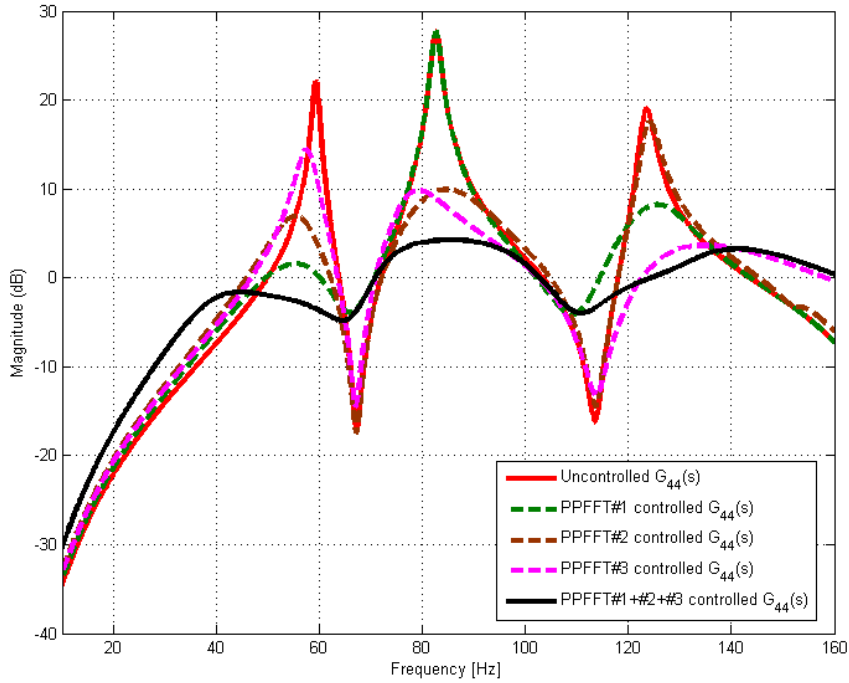


Figure 4-28 Effect of PPFFT controller on $G_{44}(s)$

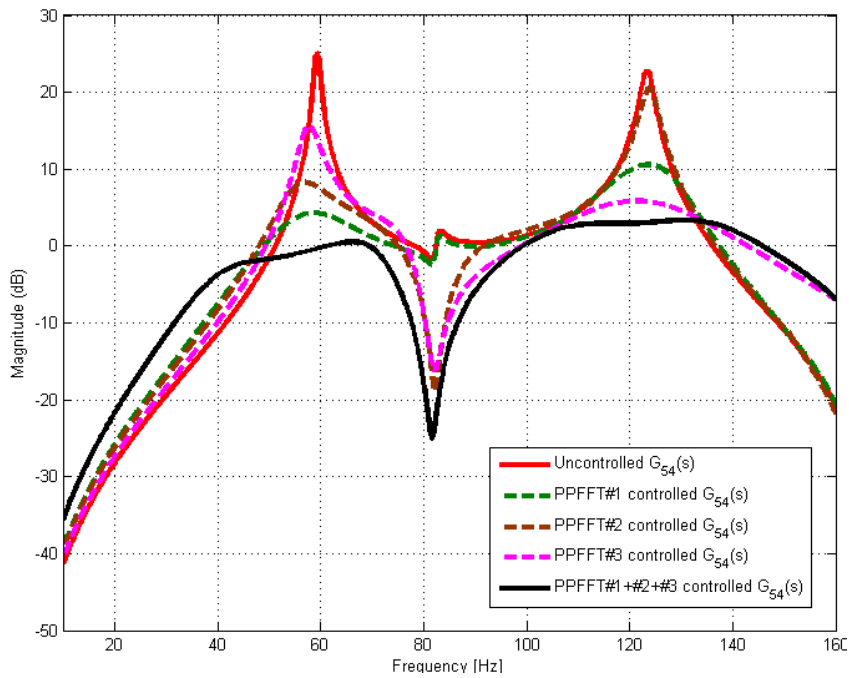


Figure 4-29 Effect of PPFFT controller on $G_{54}(s)$

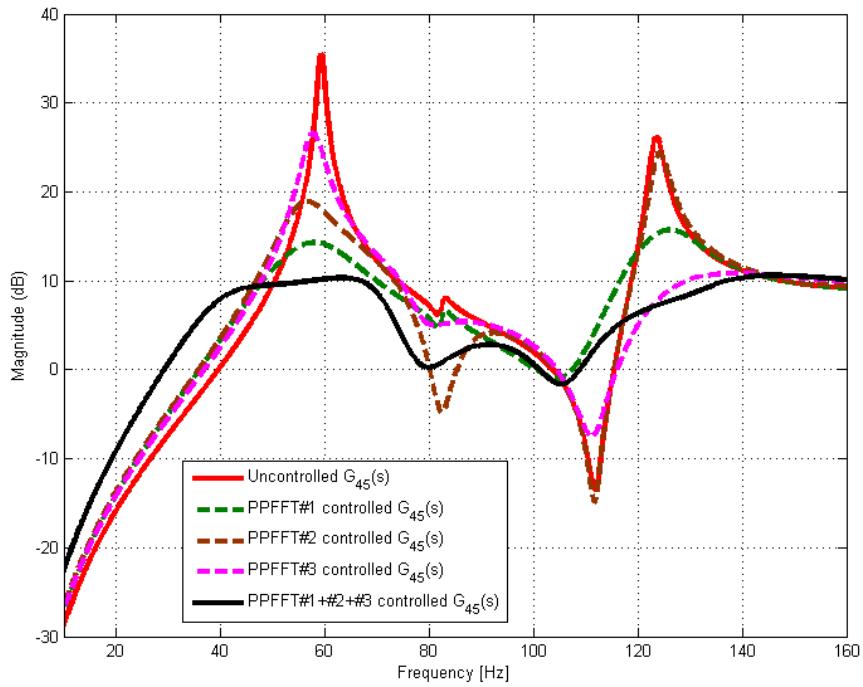


Figure 4-30 Effect of PPFFT controller on $G_{45}(s)$

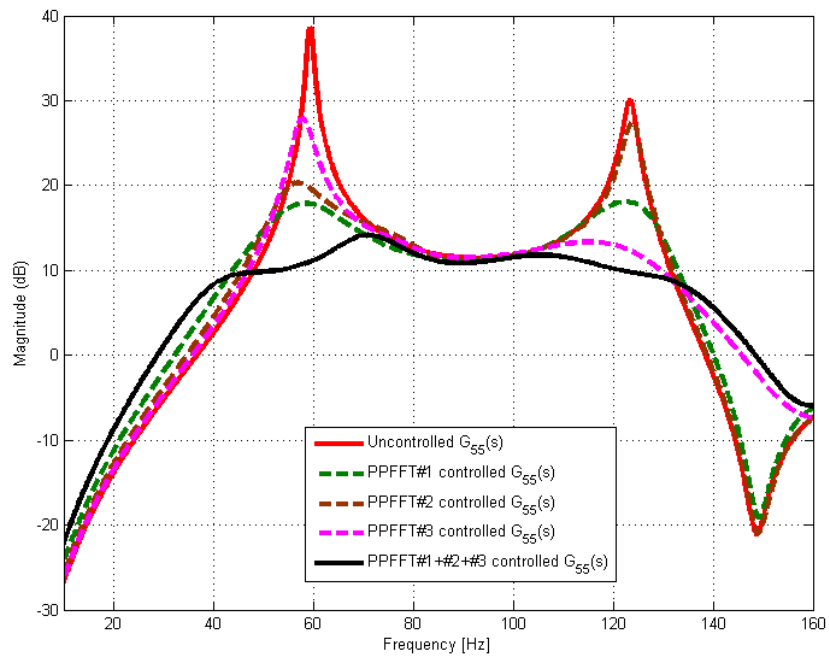


Figure 4-31 Effect of PPFFT controller on $G_{55}(s)$

MATLAB/Simulink R2010b is used in discrete-time control simulations. Fixed-step size of the solver is 0.0001 seconds. View of the Simulink model is given in Figure 4-32.

Random acceleration excitation is selected as the disturbance for the system. A constant acceleration power spectral density (PSD) of $10^{-4} g^2/\text{Hz}$ is selected by considering the in-flight vibration data

acquired from the aircraft NASA F-15B [82]. Control voltages on piezoelectric patches for duration of 120 seconds are given in Figure 4-33 to Figure 4-35.

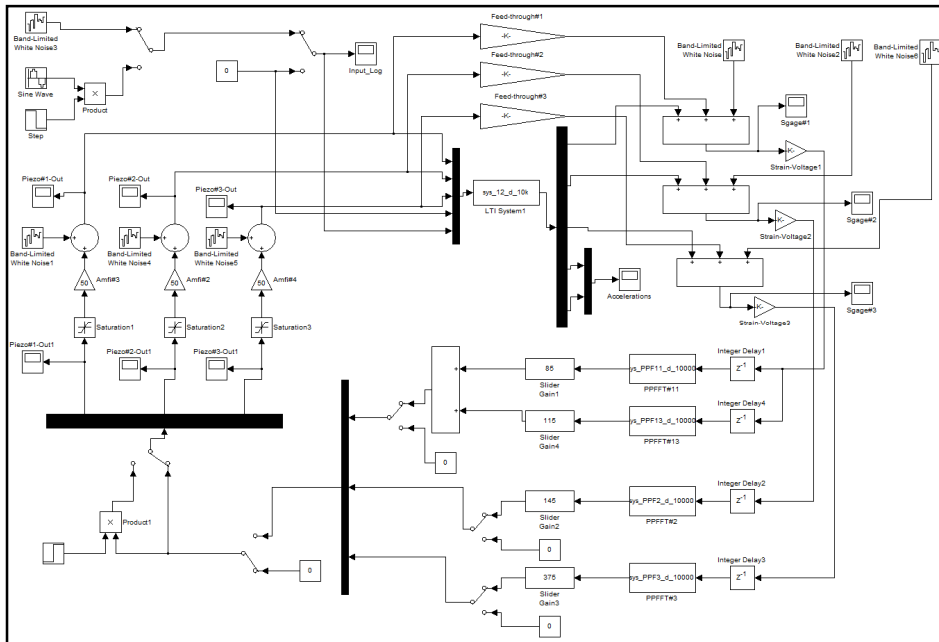


Figure 4-32 View of the Simulink model

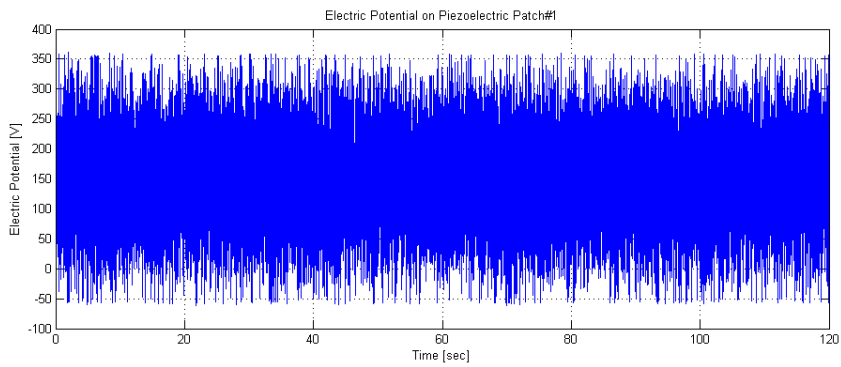


Figure 4-33 Control voltage of piezoelectric patch#1

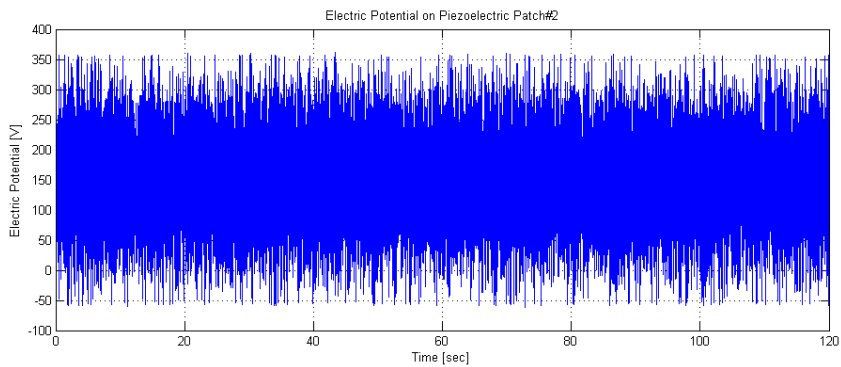


Figure 4-34 Control voltage of piezoelectric patch#2

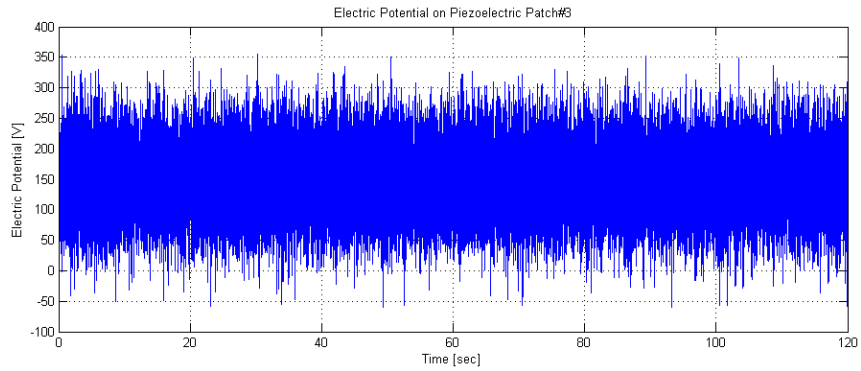


Figure 4-35 Control voltage of piezoelectric patch#3

When control voltages are examined, it can be stated that actuators do not saturate, except spikes, under the defined random acceleration disturbance. However, electric potentials of the first two actuators are close to the limits. Hence, for an excitation profile which will cause higher response amplitudes, actuator numbers and/or capabilities may require to be augmented.

PSD responses of the structure at accelerometer locations are presented in Figure 4-36 and Figure 4-37. It can be said that, obtained results are in good agreement with continuous-time responses. Previously given modal vibration suppression performances are also validated via discrete-time simulations. Another point that should be emphasized is nearly undisturbed higher frequency modes. This situation is a result of low-pass nature of PPF filters.

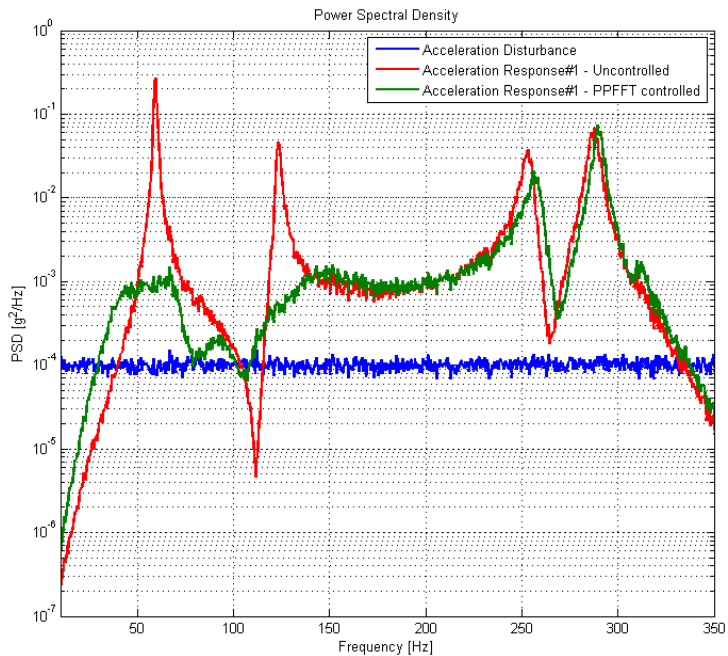


Figure 4-36 Effect of PPFFT controller on acceleration response#1

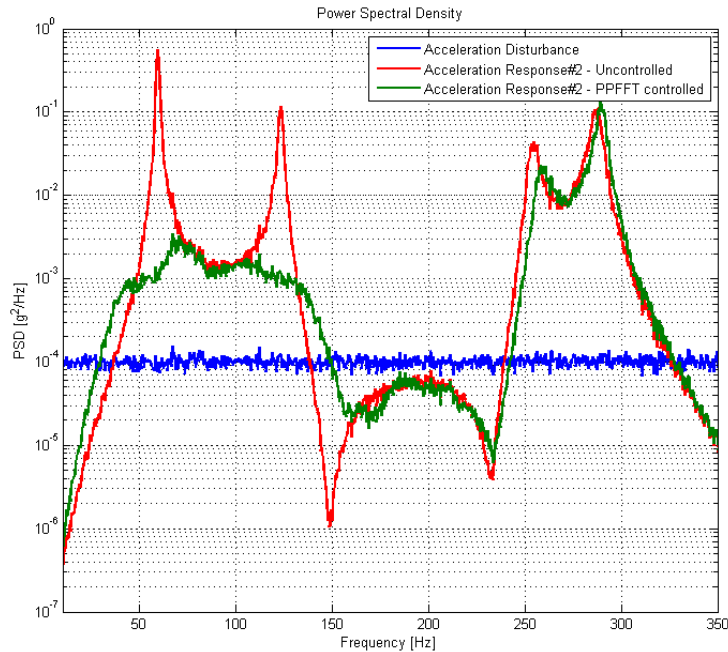


Figure 4-37 Effect of PPFFT controller on acceleration response#2

4.7 Conclusions

Studies on collocated modal control of a rectangular plate with four clamped edges are presented in this chapter. When the results are studied, the following conclusions can be drawn:

- It has been shown that, placing piezoelectric patches to high modal strain energy regions results in substantial modal controllability. Controller performance results demonstrate the validity of this statement.
- Number of modes to be used in order reduction phase should be carefully selected to capture the dynamics accurately, especially in anti-resonance regions. It has been seen that frequency range of the reduced order model should be much wider than the interested frequency range. For the defined inputs and outputs of the plant, contributions of the first 12 modes (without residual vectors) have been used to acquire the dynamics in the first 4 modes.
- Utilization of PPFFT controllers provides opportunity to control a multi-input multi-output system by controlling multiple single-input single-output collocated systems. PPF filters with high damping ratios minimize the disruptive effects of each controller on the other ones. It has been also shown that, PPFFT method works also in the case where the modes to be controlled are not well-separated.
- Proposed controller results in 24, 23 and 18 dB response reductions in the first three modes, respectively. This forced response performance is verified by discrete-time simulations in the presence of time delay, sensor/actuator noise and actuator saturation with a random acceleration disturbance considered to represent the in-flight vibration exposure.
- Performance of the controller gives promising results for a possible conformal airborne antenna application. However, it is necessary to remark that number and blocking force capability of piezoelectric patches are highly dependent on the amplitude and spectral content of the random vibration exposure. For this reason, before the design phase of such a system, platform vibration characteristics should be defined precisely.

CHAPTER 5

SUMMARY AND CONCLUSIONS

In the first part of this work, firstly conceptual information on the subjects of piezoelectric phenomenon and its modeling in ANSYS is presented. Then, theoretical backgrounds of the collocated control and three modal control methods (PPF, RC and IRC) are given. Afterwards, a modification on one of these control methods, PPF (positive position feedback), is proposed which is named as positive position feedback with feed-through (PPFFT). Also, simple design rules are suggested for these four methods with an illustrative single mode control problem. Then, a detailed literature survey on the optimality problem for piezoelectric actuator/sensor placement is presented. Finally, it is demonstrated that most of the studies point out high modal strain energy locations for optimal piezoelectric actuator placement. Hence, it is concluded to use modal strain energy method to determine best piezoelectric actuator location alternatives on the structure.

In the second part of the study, it is desired to control the first three bending modes of a cantilever beam. In order to obtain a plant model describing the dynamic characteristics of the structure, a finite element model is created in ANSYS. Since this finite element model has many DOFs, it cannot be used in control design and simulations. For this reason, the order of this model is reduced with a specialized command of ANSYS. It is demonstrated that reduced order model is in good agreement with full order model when frequency and transient response characteristics are considered.

After the reduced order model is acquired, four different collocated modal controllers (PPF, RC, IRC and PPFFT) are designed in order to maximize damping in the first three bending modes. Afterwards, open-loop transfer functions of the structure are obtained experimentally. Then, designed controllers are adapted to the experimental model which is generated using system identification techniques. Finally, real-time control experiments are performed with these controllers. When the results of these experiments are examined, it is observed that model obtained after system identification reflects the dynamics of the real structure quite successfully. It is also shown that control performance estimations based on reduced order finite element model give satisfactory results when damping properties are defined realistically. Moreover, it is demonstrated that, proposed PPFFT controller presents superior performance in out-of-resonance frequencies compared to its predecessor, PPF controller, especially when quasi-static sensor response is considered. This prevents the saturation in relatively low control gains; hence, results in improvement of steady-state response performance. PPFFT controller also shows better performance in transient response compared to other three (PPF, RC and IRC) controllers.

In the third part of the study, it is aimed to suppress the first three modes of a rectangular plate with four clamped edges. In order to determine alternative locations for piezoelectric actuator patches, modal strain energy method is employed. Since axial strain sensors are used in this study, directivities of modal strains are also taken into account. Then, the best three location alternatives are selected based on a developed performance index. After final patch locations are specified a finite element model is prepared. Model order reduction studies showed that frequency range of the reduced model should be significantly wider than the frequency range of interest.

Based on the reduced order model, three PPFFT controllers are designed for each collocated transfer function. With this action multi-input multi-output control system is treated with three single-input single-output controllers. However, it is deduced that filters with high damping ratios minimize the disruptive spillover between controllers. High disturbance rejection performances demonstrate the validity of the proposed PPFFT controller for multi-input multi-output configuration.

Finally, discrete-time simulations of the designed controller are performed in the presence of time delay, noise and actuator saturations. In these simulations, disturbance is defined as a white noise. While determining the power of this disturbance, in-flight vibration data acquired from an aircraft are considered. Disturbance rejection performances obtained with discrete-time simulations are in good agreement with continuous-time estimations. Due to missing equipment, the designed controller could not be implemented experimentally and this study is planned as a future work.

Although the results of discrete-time simulations are encouraging for a future implementation of an active vibration control system to a conformal airborne antenna, further studies are required on the following subjects:

- A high frequency electromagnetic simulation environment should be created to assess the disruptive effects of vibration on antenna performance. Also, a test facility is required to validate simulations.
- Weights of the high voltage power amplifiers, which are used to energize the piezoelectric actuators, should be minimized for aerial platform integration.
- Uncertainties in structural parameters (modal damping ratios, resonance and anti-resonance frequencies) should be determined considering several effects such as temperature change, structural degradation etc [13]. If these uncertainties are high, adaptivity should be added to modal controllers [48,49] or robust control methods can be adopted [25–31].

REFERENCES

- [1] L. Josefsson and P. Persson, *Conformal Array Antenna Theory and Design (IEEE Press Series on Electromagnetic Wave Theory)*. Wiley-IEEE Press, 2006, p. 496.
- [2] H. Schippers, R. J. C. Creemers, E. Bron, A. Hulzinga, D. J. Bekers, E. H. van der Houwen, and G. Gerini, "Integration of Antennas into Composite Load-Bearing Aircraft Structures," in *Multifunctional Structures / Integration of Sensors and Antennas (Meeting Proceedings RTO-MP-AVT-141)*, 2006, pp. 1–18.
- [3] P. J. Callus, "Conformal load-bearing antenna structure for Australian Defence Force aircraft," Australia, 2007.
- [4] P. Knott, C. Locker, and S. Algermissen, "Antenna element design for a conformal antenna array demonstrator," in *2011 Aerospace Conference*, 2011, pp. 1–5.
- [5] M. Urcia and D. Banks, "Structurally integrated phased arrays," in *2011 Aerospace Conference*, 2011, pp. 1–8.
- [6] D. Banks, M. Berden, B. Baron, and J. Tenbarge, "Structurally Integrated X-Band Array Development," in *Multifunctional Structures / Integration of Sensors and Antennas (Meeting Proceedings RTO-MP-AVT-141)*, 2006, pp. 1–12.
- [7] W. von S. R. Sekora, C. Brand, "Conformal Array Antenna for Data Link Applications," in *Multifunctional Structures / Integration of Sensors and Antennas (Meeting Proceedings RTO-MP-AVT-141)*, 2006, pp. 1–14.
- [8] T. D. Aarons, "Development and Implementation of a Flight Test Program for a Geometrically Scaled Joined Wing SensorCraft Remotely Piloted Vehicle," Virginia Polytechnic Institute and State University, Blacksburg, Virginia, 2011.
- [9] "NATO RTO TR-068 / Smart Antenna Structures (Structures d'antenne intelligentes)," in *NATO/RTO SET-012*, 2002, p. 108.
- [10] "RTO TECHNICAL REPORT TR-SET-087 / Vibrating Antennas and Compensation Techniques (Antennes vibrantes et compensations techniques)," in *NATO/RTO SET-087*, 2008.
- [11] D. Chaumette, "Technical Evaluation Report," in *Multifunctional Structures / Integration of Sensors and Antennas (Meeting Proceedings RTO-MP-AVT-141)*, 2006, p. 10.
- [12] P. Knott, C. Locker, S. Algermissen, and W. Gruner, "Research on vibration control and structure integration of antennas in NATO/RTO/SET-131," in *2010 IEEE Antennas and Propagation Society International Symposium*, 2010, pp. 1–4.
- [13] S. Algermissen, H. P. Monner, P. Knott, and R. Sekora, "Closed-loop subspace identification for vibration control of structure integrated antenna arrays," in *2011 Aerospace Conference*, 2011, pp. 1–12.
- [14] T. J. Seidel, W. S. T. Rowe, and K. Ghorbani, "Passive compensation of beam shift in an array on a bending surface."

- [15] H. Schippers, R. Cornelius, A. Hulzinga, and G. Vos, "Real-time adaptive beam-forming for vibrating airborne antenna arrays."
- [16] A. H. Daraji and J. M. Hale, "Active vibration reduction of a flexible structure bonded with optimised piezoelectric pairs using half and quarter chromosomes in genetic algorithms," *Journal of Physics: Conference Series*, vol. 382, no. 1, p. 012039, Aug. 2012.
- [17] F. Peng, "Actuator Placement Optimization and Adaptive Vibration Control of Plate Smart Structures," *Journal of Intelligent Material Systems and Structures*, vol. 16, no. 3, pp. 263–271, Mar. 2005.
- [18] Z. Xiaojin, Z. Miao, G. Zhiyuan, and C. Zhiyan, "Analysis of active vibration control for piezoelectric intelligent structures by ANSYS and MATLAB," in *2010 International Conference on Computer Application and System Modeling (ICCSM 2010)*, 2010, pp. V4–184–V4–188.
- [19] H. Karagülle, L. Malgaca, and H. F. Öktem, "Analysis of active vibration control in smart structures by ANSYS," *Smart Materials and Structures*, vol. 13, no. 4, pp. 661–667, Aug. 2004.
- [20] S. X. Xu and T. S. Koko, "Finite element analysis and design of actively controlled piezoelectric smart structures," *Finite Elements in Analysis and Design*, vol. 40, no. 3, pp. 241–262, Jan. 2004.
- [21] J. Zhang, L. He, E. Wang, and R. Gao, "A LQR Controller Design for Active Vibration Control of Flexible Structures," in *2008 IEEE Pacific-Asia Workshop on Computational Intelligence and Industrial Application*, 2008, pp. 127–132.
- [22] M. A. TRINDADE, A. BENJEDDOU, and R. OHAYON, "PIEZOELECTRIC ACTIVE VIBRATION CONTROL OF DAMPED SANDWICH BEAMS," *Journal of Sound and Vibration*, vol. 246, no. 4, pp. 653–677, Sep. 2001.
- [23] C. M. A. Vasques and J. Dias Rodrigues, "Active vibration control of smart piezoelectric beams: Comparison of classical and optimal feedback control strategies," *Computers & Structures*, vol. 84, no. 22–23, pp. 1402–1414, Sep. 2006.
- [24] V. Sethi, "Optimal Vibration Control of a Model Frame Structure Using Piezoceramic Sensors and Actuators," *Journal of Vibration and Control*, vol. 11, no. 5, pp. 671–684, May 2005.
- [25] J. Zhang, L. He, E. Wang, and R. Gao, "Active Vibration Control of Flexible Structures Using Piezoelectric Materials," in *2009 International Conference on Advanced Computer Control*, 2009, pp. 540–545.
- [26] L. Iorga, H. Baruh, and I. Ursu, "A Review of H_{∞} Robust Control of Piezoelectric Smart Structures," *Applied Mechanics Reviews*, vol. 61, no. 4, p. 040802, 2008.
- [27] W. Chang, S. V. Gopinathan, V. V. Varadan, and V. K. Varadan, "Design of Robust Vibration Controller for a Smart Panel Using Finite Element Model," *Journal of Vibration and Acoustics*, vol. 124, no. 2, p. 265, 2002.
- [28] S. Kouhi, J. Poshtan, and A. Montazeri, "Feedforward and feedback H_{∞} controllers for active vibration control of a PZT laminated thin plate," in *2007 International Conference on Intelligent and Advanced Systems*, 2007, pp. 1017–1022.
- [29] G. E. Stavroulakis, G. Foutsitzi, E. Hadjigeorgiou, D. Marinova, and C. C. Baniotopoulos, "Design and robust optimal control of smart beams with application on vibrations suppression," *Advances in Engineering Software*, vol. 36, no. 11–12, pp. 806–813, Nov. 2005.

- [30] W. Zhang, J. Qiu, and J. Tani, "Robust Vibration Control of a Plate Using Self-sensing Actuators of Piezoelectric Patches," *Journal of Intelligent Material Systems and Structures*, vol. 15, no. 12, pp. 923–931, Dec. 2004.
- [31] M. Sahin, F. M. Karadal, Y. Yaman, O. F. Kircali, V. Nalbantoglu, F. D. Ulker, and T. Caliskan, "Smart structures and their applications on active vibration control: Studies in the Department of Aerospace Engineering, METU," *Journal of Electroceramics*, vol. 20, no. 3–4, pp. 167–174, Apr. 2007.
- [32] K. Ma, "Adaptive non-linear control of a clamped rectangular plate with PZT patches," *Journal of Sound and Vibration*, vol. 264, no. 4, pp. 835–850, Jul. 2003.
- [33] N. Jalili, *Piezoelectric-Based Vibration Control: From Macro to Micro/Nano Scale Systems*. Springer, 2009.
- [34] H. S. TZOU, H.-J. LEE, and S. M. ARNOLD, "Smart Materials, Precision Sensors/Actuators, Smart Structures, and Structronic Systems," *Mechanics of Advanced Materials and Structures*, vol. 11, no. 4–5, pp. 367–393, Jul. 2004.
- [35] "Publication and Proposed Revision of ANSI/IEEE Standard 176-1987 'ANSI/IEEE Standard on Piezoelectricity'," *IEEE Transactions on Ultrasonics, Ferroelectrics and Frequency Control*, vol. 43, no. 5, p. 717, Sep. 1996.
- [36] ANSYS Inc., "ANSYS Mechanical APDL Coupled-Field Analysis Guide," Canonsburg, PA, 2010.
- [37] ANSYS Inc., "ANSYS Mechanical APDL Element Reference," Canonsburg, PA, 2010.
- [38] H. Allik and T. J. R. Hughes, "Finite element method for piezoelectric vibration," *International Journal for Numerical Methods in Engineering*, vol. 2, no. 2, pp. 151–157, Apr. 1970.
- [39] ANSYS Inc., "ANSYS Mechanical APDL and Mechanical Applications Theory Reference," Canonsburg, PA, 2010.
- [40] A. Preumont, *Vibration Control of Active Structures: An Introduction (Solid Mechanics and Its Applications)*. Springer, 2011, p. 452.
- [41] I. Petersen and A. Lanzon, "Feedback Control of Negative-Imaginary Systems," *IEEE Control Systems Magazine*, vol. 30, no. 5, pp. 54–72, Oct. 2010.
- [42] C. J. GOH and T. K. CAUGHEY, "On the stability problem caused by finite actuator dynamics in the collocated control of large space structures," *International Journal of Control*, vol. 41, no. 3, pp. 787–802, Mar. 1985.
- [43] S. Krenk and J. Hogsberg, "Equal modal damping design for a family of resonant vibration control formats," *Journal of Vibration and Control*, no. May, May 2012.
- [44] Z. Long and D. Guangren, "A robust vibration suppression controller design for space flexible structures," *2012 24th Chinese Control and Decision Conference (CCDC)*, pp. 4020–4024, May 2012.
- [45] R. R. Orszulik and J. Shan, "Active vibration control using genetic algorithm-based system identification and positive position feedback," *Smart Materials and Structures*, vol. 21, no. 5, p. 055002, May 2012.
- [46] J. Xiong, I. R. Petersen, and A. Lanzon, "On lossless negative imaginary systems," *Automatica*, vol. 48, no. 6, pp. 1213–1217, Jun. 2012.

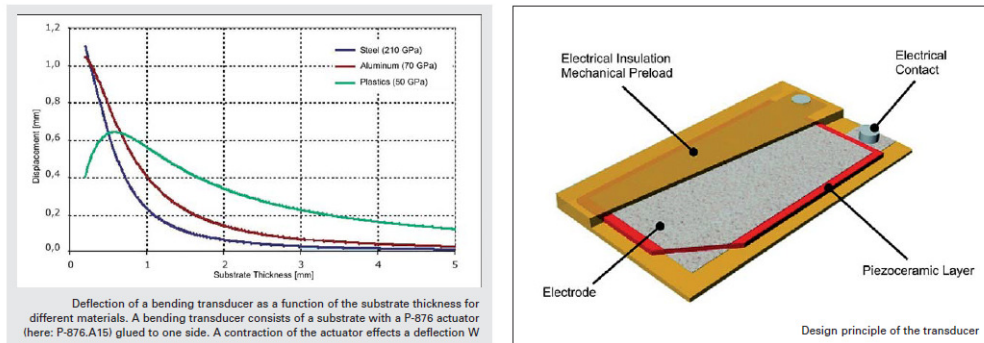
- [47] D. J. Inman, "Comparison of Control Laws for Vibration Suppression Based on Energy Consumption," *Journal of Intelligent Material Systems and Structures*, vol. 22, no. 8, pp. 795–809, Jun. 2011.
- [48] R. Orszulik and J. Shan, "Multi-mode adaptive positive position feedback: An experimental study," *American Control Conference (ACC), 2011*, pp. 3315–3319, 2011.
- [49] S. Nima Mahmoodi, M. Ahmadian, and D. J. Inman, "Adaptive Modified Positive Position Feedback for Active Vibration Control of Structures," *Journal of Intelligent Material Systems and Structures*, vol. 21, no. 6, pp. 571–580, Feb. 2010.
- [50] J. L. FANSON and T. K. CAUGHEY, "Positive position feedback control for large space structures," *AIAA Journal*, vol. 28, no. 4, pp. 717–724, Apr. 1990.
- [51] S. Pietrzko and M. J. Brennan, "Active Vibration Isolation Using an Electrical Damper or an Electrical Dynamic Absorber," *IEEE Transactions on Control Systems Technology*, vol. 16, no. 2, pp. 245–254, Mar. 2008.
- [52] S.-M. Kim, S. Wang, and M. J. Brennan, "Comparison of negative and positive position feedback control of a flexible structure," *Smart Materials and Structures*, vol. 20, no. 1, p. 015011, Jan. 2011.
- [53] D. Halim and S. O. R. Moheimani, "Spatial resonant control of flexible structures-application to a piezoelectric laminate beam," *IEEE Transactions on Control Systems Technology*, vol. 9, no. 1, pp. 37–53, 2001.
- [54] H. R. Pota, S. O. R. Moheimani, and M. Smith, "Resonant controllers for smart structures," *Smart Materials and Structures*, vol. 11, no. 1, pp. 1–8, Feb. 2002.
- [55] S. S. Aphale, A. J. Fleming, and S. O. R. Moheimani, "Integral resonant control of collocated smart structures," *Smart Materials and Structures*, vol. 16, no. 2, pp. 439–446, Apr. 2007.
- [56] B. Bhikkaji, S. O. R. Moheimani, and I. R. Petersen, "Multivariable integral control of resonant structures," *2008 47th IEEE Conference on Decision and Control*, pp. 3743–3748, 2008.
- [57] H. S. Tzou and H. Q. Fu, "A Study of Segmentation of Distributed Piezoelectric Sensors and Actuators, Part I: Theoretical Analysis," *Journal of Sound and Vibration*, vol. 172, no. 2, pp. 247–259, Apr. 1994.
- [58] V. Gupta, M. Sharma, and N. Thakur, "Optimization Criteria for Optimal Placement of Piezoelectric Sensors and Actuators on a Smart Structure: A Technical Review," *Journal of Intelligent Material Systems and Structures*, vol. 21, no. 12, pp. 1227–1243, Sep. 2010.
- [59] Y. C. Liu and S. M. Yang, "Three Simple and Efficient Methods for Vibration Control of Slewing Flexible Structures," in *American Control Conference, 1992*, 1992, pp. 1670–1674.
- [60] I. Bruant, L. Gallimard, and S. Nikoukar, "Optimal piezoelectric actuator and sensor location for active vibration control, using genetic algorithm," *Journal of Sound and Vibration*, vol. 329, no. 10, pp. 1615–1635, May 2010.
- [61] A. K. Jha and D. J. Inman, "Optimal Sizes and Placements of Piezoelectric Actuators and Sensors for an Inflated Torus," *Journal of Intelligent Materials Systems and Structures*, vol. 14, no. 9, pp. 563–576, Sep. 2003.
- [62] A. M. Sadri, J. R. Wright, and R. J. Wynne, "Modelling and optimal placement of piezoelectric actuators in isotropic plates using genetic algorithms," *Smart Materials and Structures*, vol. 8, no. 4, pp. 490–498, Aug. 1999.

- [63] K. Ramesh Kumar and S. Narayanan, "Active vibration control of beams with optimal placement of piezoelectric sensor/actuator pairs," *Smart Materials and Structures*, vol. 17, no. 5, p. 055008, Oct. 2008.
- [64] Y. Yang, Z. Jin, and C. Kiong Soh, "Integrated optimal design of vibration control system for smart beams using genetic algorithms," *Journal of Sound and Vibration*, vol. 282, no. 3–5, pp. 1293–1307, Apr. 2005.
- [65] S. T. QUEK, S. Y. WANG, and K. K. ANG, "Vibration Control of Composite Plates via Optimal Placement of Piezoelectric Patches," *Journal of Intelligent Materials Systems and Structures*, vol. 14, no. 4, pp. 229–245, Apr. 2003.
- [66] D. E. Heverly, "OPTIMAL ACTUATOR PLACEMENT AND ACTIVE STRUCTURE DESIGN FOR CONTROL OF HELICOPTER AIRFRAME VIBRATIONS," The Pennsylvania State University, 2002.
- [67] L. BIN, L. YUGANG, Y. XUEGANG, and H. SHANGLIAN, "Maximal Modal Force Rule for Optimal Placement of Point Piezoelectric Actuators for Plates*," *Journal of Intelligent Material Systems and Structures*, vol. 11, no. 7, pp. 512–515, Jul. 2000.
- [68] K.-H. Ip and P.-C. Tse, "Optimal configuration of a piezoelectric patch for vibration control of isotropic rectangular plates," *Smart Materials and Structures*, vol. 10, no. 2, pp. 395–403, Apr. 2001.
- [69] R. Barboni, A. Mannini, E. Fantini, and P. Gaudenzi, "Optimal placement of PZT actuators for the control of beam dynamics," *Smart Materials and Structures*, vol. 9, no. 1, pp. 110–120, Feb. 2000.
- [70] Y. Yang and L. Zhang, "Optimal excitation of a rectangular plate resting on an elastic foundation by a piezoelectric actuator," *Smart Materials and Structures*, vol. 15, no. 4, pp. 1063–1078, Aug. 2006.
- [71] K. Ramesh Kumar and S. Narayanan, "The optimal location of piezoelectric actuators and sensors for vibration control of plates," *Smart Materials and Structures*, vol. 16, no. 6, pp. 2680–2691, Dec. 2007.
- [72] K. Ogata, *Modern Control Engineering (5th Edition)*. Prentice Hall, 2009, p. 912.
- [73] A. Hać and L. Liu, "Sensor And Actuator Location In Motion Control Of Flexible Structures," *Journal of Sound and Vibration*, vol. 167, no. 2, pp. 239–261, Oct. 1993.
- [74] I. Bruant and L. Proslier, "Optimal Location of Actuators and Sensors in Active Vibration Control," *Journal of Intelligent Material Systems and Structures*, vol. 16, no. 3, pp. 197–206, Mar. 2005.
- [75] Q. WANG and C. M. WANG, "A CONTROLLABILITY INDEX FOR OPTIMAL DESIGN OF PIEZOELECTRIC ACTUATORS IN VIBRATION CONTROL OF BEAM STRUCTURES," *Journal of Sound and Vibration*, vol. 242, no. 3, pp. 507–518, May 2001.
- [76] S. O. R. Moheimani and T. Ryall, "Considerations on placement of piezoceramic actuators that are used in structural vibration control," in *Proceedings of the 38th IEEE Conference on Decision and Control (Cat. No.99CH36304)*, vol. 2, pp. 1118–1123.
- [77] J. L. JUNKINS and Y. KIM, "Measure of controllability for actuator placement," *Journal of Guidance, Control, and Dynamics*, vol. 14, no. 5, pp. 895–902, Sep. 1991.
- [78] D. Halim and S. O. Reza Moheimani, "An optimization approach to optimal placement of collocated piezoelectric actuators and sensors on a thin plate," *Mechatronics*, vol. 13, no. 1, pp. 27–47, Feb. 2003.

- [79] Z. Qiu, X. Zhang, H. Wu, and H. Zhang, "Optimal placement and active vibration control for piezoelectric smart flexible cantilever plate," *Journal of Sound and Vibration*, vol. 301, no. 3–5, pp. 521–543, Apr. 2007.
- [80] T.-W. Kim and J.-H. Kim, "Optimal distribution of an active layer for transient vibration control of a flexible plate," *Smart Materials and Structures*, vol. 14, no. 5, pp. 904–916, Oct. 2005.
- [81] M. Géradin and D. Rixen, *Mechanical Vibrations: Theory and Application to Structural Dynamics*, 2E. John Wiley & Sons, 1997, p. 444.
- [82] S. Corda, R. J. Franz, J. N. Blanton, M. J. Vachon, and J. B. Deboer, "In-Flight Vibration Environment of the NASA F-15B Flight Test Fixture," California, 2002.

APPENDIX A

PROPERTIES OF PI DURA ACT P-876.A12



| Technical Data | P-876.A11 | P-876.A12 | P-876.A15 | Tolerances |
|--------------------------------|---|---|--|--------------|
| Operating voltage | -50 to +200 V | -100 to +400 V | -250 to +1000 V | |
| Motion and positioning | | | | |
| Lateral contraction, open-loop | 400 $\mu\text{m/m}$ 1.6 $\mu\text{m}/(\text{H/m/V})$ | 650 $\mu\text{m/m}$ 1.3 $\mu\text{m}/(\text{H/m/V})$ | 800 $\mu\text{m/m}$ 0.64 $\mu\text{m}/(\text{H/m/V})$ | min. |
| Mechanical properties | | | | |
| Holding force | 90 N | 265 N | 775 N | |
| Length | 61 mm | 61 mm | 61 mm | ± 0.5 mm |
| Width | 35 mm | 35 mm | 35 mm | ± 0.5 mm |
| Thickness | 0.4 mm | 0.5 mm | 0.8 mm | ± 0.5 mm |
| Bending radius | 12 mm | 20 mm | 70 mm | max. |
| Drive properties | | | | |
| Piezo ceramic type | PIC 252 Layer thickness: 100 μm | PIC 255 Layer thickness: 200 μm | PIC 255 Layer thickness: 500 μm | |
| Electrical capacitance | 150 nF | 90 nF | 45 nF | $\pm 20\%$ |
| Miscellaneous | | | | |
| Operating temperature range | -20 to +150 (180) $^{\circ}\text{C}$ | -20 to +150 (180) $^{\circ}\text{C}$ | -20 to +150 (180) $^{\circ}\text{C}$ | |
| Mass | 2.1 g | 3.5 g | 7.2 g | $\pm 5\%$ |
| Voltage connection | Solder pads | Solder pads | Solder pads | |
| Recommended controller/driver | E-413.D2 | E-413.D2 | E-508 | |

Figure A-1 Properties of PI DuraAct P-876.A12

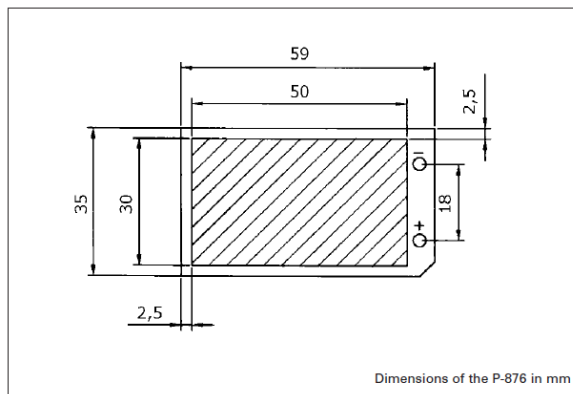


Figure A-2 Dimensions of PI DuraAct P-876.A12

APPENDIX B

Z-POLARIZED MATERIAL PROPERTIES OF PIC255



| Material coefficients PIC255 | | | | | |
|------------------------------|-------------------|------------|-------------|------------------|-----------|
| Coefficient | Unit | Value | Coefficient | Unit | Value |
| Density | kg/m ³ | 7,80E+03 | N1 | Hzm | 1420 |
| Qm | | 80 | N3 | Hzm | 1710 |
| | | | N5 | Hzm | 1125 |
| ε 11Tr | | 1649 | Np | Hzm | 2000 |
| ε 33Tr | | 1750 | Nt | Hzm | 2000 |
| ε 11Sr | | 930 | | | |
| ε 33Sr | | 857 | d31 | m/V | -1,74E-10 |
| | | | d33 | m/V | 3,94E-10 |
| β 11T | Vm/As | 6,85E+07 | d15 | m/V | 5,35E-10 |
| β 33T | Vm/As | 6,45E+07 | | | |
| β 11S | Vm/As | 1,21E+08 | g31 | Vm/N | -1,13E-02 |
| β 33S | Vm/As | 1,32E+08 | g33 | Vm/N | 2,54E-02 |
| | | | g15 | Vm/N | 3,66E-02 |
| tan δ | | 20,0E-3 | | | |
| | | | e31 | N/Vm | -7,15 |
| k31 | | 0,351 | e33 | N/Vm | 13,70 |
| k33 | | 0,691 | e15 | N/Vm | 11,90 |
| k15 | | 0,661 | | | |
| kp | | 0,620 | h31 | N/As | -9,49E+08 |
| kt | | 0,471 | h33 | N/As | 1,81E+09 |
| | | | h15 | N/As | 1,45E+09 |
| Poisson (σ) | | 0,36 | | | |
| | | | | | |
| s11E | m ² /N | 1,590E-11 | c11E | N/m ² | 1,230E+11 |
| s33E | m ² /N | 2,097E-11 | c33E | N/m ² | 9,711E+10 |
| s55E | m ² /N | 4,492E-11 | c55E | N/m ² | 2,226E+10 |
| s12E | m ² /N | -5,699E-12 | c12E | N/m ² | 7,670E+10 |
| s13E | m ² /N | -7,376E-12 | c13E | N/m ² | 7,025E+10 |
| s44E | m ² /N | 4,492E-11 | c44E | N/m ² | 2,226E+10 |
| s66E | m ² /N | 4,319E-11 | c66E | N/m ² | 2,315E+10 |
| | | | | | |
| s11D | m ² /N | 1,393E-11 | c11D | N/m ² | 1,298E+11 |
| s33D | m ² /N | 1,096E-11 | c33D | N/m ² | 1,220E+11 |
| s55D | m ² /N | 2,532E-11 | c55D | N/m ² | 3,949E+10 |
| s12D | m ² /N | -7,660E-12 | c12D | N/m ² | 8,345E+10 |
| s13D | m ² /N | -2,945E-12 | c13D | N/m ² | 5,729E+10 |
| s44D | m ² /N | 2,532E-11 | c44D | N/m ² | 3,949E+10 |
| s66D | m ² /N | 4,319E-11 | c66D | N/m ² | 2,315E+10 |

Values are only for information - no specification!

Simulation purpose

The data in the table was determined using testbodies with geometries and dimensions in accordance with European Standard EN 50324 2, and are typical values.

Singular parameters can deviate from catalogue values, because they were measured at samples which were taken from one block of ceramics according to the sequence of IEC483 to get maximum consistency.

Catalogue values reflect the statistical distribution of each individual specification in production and therefore also take into account spreading from material batch to material batch.

Figure B-1 Piezoelectric material properties of PIC255

Command snippet to define Z-polarized PIC255 material properties

```
mpde,all,matid  
tbde,all,matid
```

```
et,matid,5,3 ! SOLID5 element type
```

```
TB,ANEL,matid,1,0 ! Elastic stiffness matrix  
TBDATA,1,1.23E+11,7.67E+10,7.03E+10  
TBDATA,7,1.23E+11,7.03E+10  
TBDATA,12,9.71E+10  
TBDATA,16,2.32E+10  
TBDATA,19,2.23E+10  
TBDATA,21,2.23E+10
```

```
TB,PIEZ,matid ! Piezoelectric stress matrix  
TBDATA,3,-7.15  
TBDATA,6,-7.15  
TBDATA,9,13.7  
TBDATA,14,11.9  
TBDATA,16,11.9
```

```
EMUNIT,EPZRO,8.85E-12 ! Permittivity  
MP,PERX,matid,930  
MP,PERY,matid,930  
MP,PERZ,matid,857
```

```
MP,DENS,matid,7800*1.496
```

APPENDIX C

COMMAND SNIPPETS FOR ORDER REDUCTION

Command Snippet Added to the Model Branch

```
/solu
antype,2
modopt,lanb,4
mxpand,4
resvec,on
modcont,on
alphad,1.131702
betad,0.0000432845

cmsel,s,Piezo1_Top
cp,1,volt,all
*get,n1top,node,,num,min
d,n1top,volt,1
nset,all
cmsel,all
!*

cmsel,s,Piezo1_Bot
cp,2,volt,all
*get,n1bot,node,,num,min
d,n1bot,volt,0
nset,all
cmsel,all
!*

cmsel,s,Piezo2_Top
cp,3,volt,all
*get,n2top,node,,num,min
d,n2top,volt,0
nset,all
cmsel,all
!*

cmsel,s,Piezo2_Bot
cp,4,volt,all
*get,n2bot,node,,num,min
d,n2bot,volt,0
nset,all
cmsel,all
!*

cmsel,s,Beam_root
cp,5,ux,all
cp,6,uy,all
cp,7,uz,all
*get,nroot,node,,num,min
d,nroot,ux,0
d,nroot,uy,0
```

```
d,nroot,uz,0
nset,all
cmsgel,all
!*
solve
```

```
ddele,all
fdele,all
```

```
d,n1top,volt,0
d,n1bot,volt,0
d,n2top,volt,1
d,n2bot,volt,0
d,nroot,ux,0
d,nroot,uy,0
d,nroot,uz,0
!*
```

```
solve
fini
```

Command Snippet Added to the Solution Branch

```
/post1
```

```
cmsgel,,Beam_tip,node
*GET,beamtíp,NODE,0,NUM,MAX, ,
cmsgel,,Far,node
*GET,far,NODE,0,NUM,MAX, ,
cmsgel,,Near,node
*GET,near,NODE,0,NUM,MAX, ,
nset,all
cmsgel,all
```

```
*dim,output,,3,2
output(1,1)= near
output(1,2)= 1
output(2,1)= far
output(2,2)= 1
output(3,1)= beamtip
output(3,2)= 3
```

```
*dim,outputLab,CHAR,3
outputLab(1)='NEAR_X'
outputLab(2)='FAR_X'
outputLab(3)='BEAM_TIP_Z'
```

```
*dim,inputLab,CHAR,2
inputLab(1)='PIEZO_1'
inputLab(2)='PIEZO_2'
```

```
SPMWRITE,modal,,,inputLab,output,outputLab,,,0
```


APPENDIX E

MATLAB SCRIPT PARSING THE GENERATED SPM FILE

```
Edge_length=0.01; % Length of the strain gage

fid = fopen('4_mode.spm','r'); % Select the .spm file to be read

while(~feof(fid))
    line=fgetl(fid);
    name=sscanf(line,['%s' 'MATRIX']);

    if name=='A'; % System Matrix
        line=fgetl(fid);
        size_A=sscanf(line,'%f');
        for i=1:size_A(1);
            line=fgetl(fid);
            A(i,:)=sscanf(line,'%f');
        end
    end

    if name=='B'; % Input Matrix
        line=fgetl(fid);
        size_B=sscanf(line,'%f');
        for j=1:size_B(1);
            line=fgetl(fid);
            B(j,:)=sscanf(line,'%f');
        end
    end

    if name=='C'; % Output Matrix
        line=fgetl(fid);
        size_C=sscanf(line,'%f');
        for k=1:size_C(1);
            line=fgetl(fid);
            CCC(k,:)=sscanf(line,'%f');
        end
    end
end

fclose(fid);

C(1,:)=(CCC(2,:)-CCC(1,:))./Edge_length; % Acquiring axial strain from directional displacements
C(2,:)=CCC(3,:)*1000; % Unit conversion for displacement output

D=zeros(2,2); % Direct feed-through matrix

sys_4=ss(A,B,C,D); % System in state-space
```